1971

Microwave absorption in terbium, erbium and MnAu2 at selected frequencies from 20 - 120 GHz

Lynn Winterton Hart
Iowa State University

Microwave absorption in terbium, erbium and $MnAu_2$ at selected frequencies from 20 - 120 GHz

by

Lynn Winterton Hart

A Dissertation Submitted to the
Graduate Faculty in Partial Fulfillment of
The Requirements for the Degree of
DOCTOR OF PHILOSOPHY

Major Subject: Solid State Physics

Approved:

Signature was redacted for privacy.

In Charge of Major Work

Signature was redacted for privacy.

For the Major Department

Signature was redacted for privacy.

For the Graduate College

Iowa State University
Ames, Iowa

1971

TABLE OF CONTENTS

I. INTRODUCTION

This thesis is divided into three major sections, each section corresponding to a microwave absorption study of a different material.

The terbium section contains a description of the 24 GHz microwave gear used in these experiments, and gives a theoretical and experimental description of ferromagnetic resonance in terbium. Our experimental results provide evidence that magnetoelastic strain in terbium is free to follow the motion of the localized spin on a given terbium ion.

The $MnAu_2$ section contains a description of the 100 GHz microwave gear used in these experiments, and gives a theoretical description of spiral phase antiferromagnetic resonance predicted for $MnAu_2$. A theoretical and experimental description of field-induced fan and ferromagnetic resonance absorptions in $MnAu_2$ is also given, as well as an experimental description of some very unusual resonances in the antiferromagnetic spiral phase of $MnAu_2$ that are not theoretically predicted.

The erbium section gives a theoretical description of resonance absorption expected for the many unusual magnetic phases of erbium. We observe no microwave resonance absorption at our experimental frequencies, in agreement with theory. We do observe many field induced magnetic transitions which can be used to derive theoretical parameters describing the static magnetic configurations of erbium.

II. TERBIUM

A. Introduction

Terbium crystallizes in a hexagonal close-packed structure and is a silvery gray heavy rare-earth metal that is soft enough to be cut with a knife. Terbium oxidizes slowly in air (the oxide is a chocolate or dark maroon color (1)). In its metallic state (below 1356°C) terbium is a trivalent ion immersed in a sea of conduction electrons. The electronic configuration for the Tb ion is $4f^8 5s^2 5p^6$ with a ground state spectroscopic designation $^7F_6$ and a Landé factor g=3/2. The maximum theoretical magnetic moment on one Tb ion at low temperatures is therefore $9\mu_B$, where μ_B is the Bohr magneton. This magnetic moment is entirely due to the unfilled 4f electronic shell inside the 5s and 5p shells, and is therefore very localized on the Tb ion. Tb metal can be thought of as a lattice of atomic magnets interacting with each other via a sea of conduction electrons. The magnetic interaction between Tb ions is long range and gives rise to periodic ordering of the spins as is also the case in the other heavy rare-earth elements (2). The differing magnetic moments on the various heavy rare-earth ions interacting with conduction electrons having a certain Fermi-surface geometry gives rise to the helical ordering of the spins (3) observed by neutron diffraction (4). Effects associated with the crystal structure such as the crystal field effect and the magnetoelastic effect often significantly affect the spin ordering and the occurrence of magnetic transitions (3). In particular, Tb is paramagnetic above 229 K, and ferromagnetic below 222 K (5). From 222 - 229 K, Tb has

a planar spiral spin configuration (4). The plane of the spiral is perpendicular to the c-axis (⟨0001⟩ direction) due to a very large uniaxial anisotropy field (6). This planar spiral collapses to a ferromagnet with application of a magnetic field of less than 1 kOe in the plane of the spiral (5). In the ferromagnetic region the spins align along a b-axis (⟨$10\bar{1}0$⟩ direction) due predominantly to magnetoelastic effects (7). The driving force in the spiral-to-ferromagnetic transition in Tb is the negative magnetoelastic energy associated with the ferromagnetic state (there is no magnetoelastic energy associated with the spiral state at equilibrium) (3).

Our experiment deals with the excited states (spin waves or "magnons") of the ferromagnetically aligned spin system in Tb. These states are excited by an experiment in which an external magnetic field is applied perpendicular to the c-axis of the sample while photons of a certain polarization and frequency (24 GHz) strike the sample surface. When the photons are absorbed by the Tb spin system at a given temperature, microwave polarization, and magnetic field we have the condition known as ferromagnetic resonance. In the following section the theory of ferromagnetic resonance in Tb will be discussed, and it will be shown that much useful information can be obtained by studying the dynamic behavior of the spin system.

B. Theory

Apparent contradictions between the high and low frequency ferromagnetic resonance results in Tb and Dy have prompted much theoretical

speculation (8). Earlier calculations of ferromagnetic resonance energy gaps did not include the magnetoelastic energy (9), and the result came to be known as the "free lattice model" because it was identical to the later result obtained by considering the crystal strains to be locally coupled to the ionic spins at zero wavenumber (q=0) (10). In this local coupling theory the first order magnetoelastic energy is invariant under rotation of the magnetization in the hexagonal plane for q=0, so it has no effect on the spin-wave spectrum at q=0 (8, 10). In the free lattice model the second-order magnetoelastic energy simply provides the hexagonal anisotropy in the basal plane of Tb (the hexagonal anisotropy due to the crystal field is negligible) (7, 8). If an external magnetic field (H_{dc}) is applied along a hard $\langle 11\bar{2}0 \rangle$ direction in the basal plane, the ferromagnetic resonance (q=0) energy gap can be reduced to zero in Tb at the spin-flip field (when the spins align along H_{dc}) in the free lattice model (8). Ferromagnetic resonance experiments at about 38 GHz in Dy single crystals seem to confirm the applicability to Dy of the free lattice model just discussed (11, 12).

Another model of the magnetoelastic strains was proposed by Turov and Shavrov (13). They suggested that the uniform (q=0) mode should be found by considering the strain as frozen at its equilibrium position. If the strain is not free to follow the instantaneous motion of the excited spins, an external magnetic field is unable to lower the q=0 energy gap appreciably, making observation of this mode difficult except at very high frequencies or high temperatures (the energy gap decreases with increasing temperature) (8, 10). Inelastic neutron scattering

experiments (7) and high frequency (100 GHz) microwave experiments (14) in Tb seem to be explained by the frozen lattice model. In fact, 100 GHz microwave experiments in Dy might also be explained by the frozen lattice model (15) in contrast to the 38 GHz experiments previously mentioned.

Vigren and Liu (10) recently proposed a theory explaining these apparent contradictions by predicting free lattice model behavior in Tb and Dy at low microwave frequencies and frozen lattice model behavior at high microwave frequencies and in neutron diffraction experiments. As stated, free lattice model behavior was predicted for Tb at low microwave frequencies, but a difference between the results expected from the free lattice and frozen lattice models does not occur until temperatures below 140 K are investigated. All low frequency ferromagnetic resonance experiments in Tb prior to the work reported in this thesis were for temperatures above 140 K, and so were subject to differing interpretations (16, 17). The experimental data in this thesis for Tb at low frequencies and temperatures below 140 K provide strong evidence in support of the theory of Vigren and Liu, supplying a satisfying resolution to the apparent contradictions which have existed for some time in the literature.

The theory of Vigren and Liu (10) assumes the crystal strains to be locally coupled to the ionic spins as in the free lattice model. For zero wavenumber (q=0) spin waves, all spins oscillate in phase and the magnetoelastic contribution to the Hamiltonian is that due to a single spin multiplied by the number of spins. This energy is invariant under rotation of the magnetization in the hexagonal plane to first order, so

the free lattice model holds, which means that except for the hexagonal anisotropy due to second order magnetoelastic effects (which allow the external field in the $\langle 11\bar{2}0 \rangle$ direction to lower the energy gap to zero at the spin-flip field), there is essentially no magnetoelastic contribution to the spin wave spectrum at $q=0$. This first order magnetoelastic energy is quite large as determined from magnetostriction measurements (18) using the theory of Callen and Callen (19).

For $q \neq 0$ spin waves, however, the spins are not in phase, and this phase difference causes a cancellation of all but the equilibrium magnetoelastic energy, resulting in the frozen lattice model and a large magnetoelastic contribution to the spin wave spectrum which can not be overcome by application of an external magnetic field. Note that by making the free lattice model assumption of local coupling of the ionic spins, Vigren and Liu arrived at the same result for $q \neq 0$ as the ad hoc frozen lattice model proposed by Turov and Shavrov. The major contribution of the theory of Vigren and Liu was to correctly minimize the locally coupled magnetoelastic energy with respect to the instantaneous strains (caused by motion of the ionic spins) for $q \neq 0$ spin waves. This simple theory correctly accounts for the major experimental results involving excited spin wave states in Tb and Dy with the inclusion of the experimental results on Tb reported in this thesis.

In a ferromagnetic resonance experiment the largest value of q excited is $q \tilde{=} 1/\delta$, where δ is the classical microwave skin depth inversely proportional to the square root of the microwave frequency. In such an experiment, Vigren and Liu show that in the approximation of an infinite

crystal the transition rate to a state of q less than $1/\delta$ is proportional to a constant (20) (assuming the spin wave energy is approximately the same as the microwave energy, a condition called on-resonance absorption). Since there are perhaps 10^3 allowed values of q between 0 and $1/\delta$, each having approximately the same energy, we can talk about a $q=0^+$ mode excited with an intensity 10^3 greater than the q=0 mode at the same energy ($10^3=L/\delta$ using periodic boundary conditions where L is the sample thickness). The specification in the preceding sentence "at the same energy" is important because as we have previously discussed, q=0 corresponds to the "free lattice model", while $q=0^+$ corresponds to the "frozen lattice model" in the theory of Vigren and Liu. These two models generally predict resonance at different frequency values because only the q=0 "free lattice model" energy gap can be made zero by application of an external magnetic field. In our experiment, the applied field in a hard $\langle 11\bar{2}0\rangle$ direction lowers the energy of the q=0 free lattice mode to that of our microwave energy, while the $q=0^+$ frozen lattice mode remains well above our experimental frequency. This experiment is therefore only capable of exciting the q=0 mode in on-resonance absorption. It should be stressed that the discontinuity in the spin wave spectrum between q=0 and $q=0^+$ is artificial and results from the assumption of an infinite sample using periodic boundary conditions. If more realistic boundary conditions are considered, a smooth transition from q=0 to $q=0^+$ should take place over a range of q determined by the inverse of the thickness of the specimen (21). An even more realistic model effectively increases the number of free lattice states as compared with frozen lattice states so

that $0 \leq q \lesssim 1/\delta$ are essentially free lattice states and $1/\delta \lesssim q \leq \frac{2\pi}{c}$ are frozen lattice states, making observation of the free lattice states with microwaves more probable (20). In any case, the q=0 mode should be visible if the microwave frequency is low enough, because then the $q=0^+$ mode energy is much higher than the microwave frequency (making on-resonance absorption impossible and off-resonance absorption improbable for the $q=0^+$ mode), while the q=0 mode is excited in on-resonance absorption. We had an indication that our frequency of 24 GHz was low enough to see the q=0 mode from the numerical estimates of Intensity made by Vigren and Liu (20), and from the fact that Rossol and Jones (11) saw the q=0 mode in Dy at 38 GHz. Similar behavior is expected in both Tb and Dy as far as intensity is concerned.

In more detail, the theory of Vigren and Liu starts out with a Hamiltonian consisting of exchange, uniaxial anisotropy, hexagonal anisotropy, a Zeeman term, and first-order magnetoelastic terms corresponding to the theory of Callen and Callen (19). Demagnetizing effects due to sample dimensions are considered phenomenologically at the end of the calculation by following Kittel (22). Second order magnetoelastic effects are not considered, but recent work reported in Reference (7) considers these effects both theoretically and experimentally using neutron diffraction for the $q=0^+$ frozen lattice mode. The neutron diffraction results showed that the hexagonal anisotropy of Tb was entirely due to second order magnetoelastic effects within experimental error. Of interest to us are the effects of the second order magnetoelastic energy on the q=0 free lattice mode. Cooper (8) has calculated this effect, and as in the frozen

lattice case, the only effect is to add to the hexagonal anisotropy due to the crystal field a hexagonal anisotropy due to second-order magnetoelastic energy. Since the hexagonal anisotropy due to crystal field has no wavenumber dependence, we may take it as zero in the q=0 case since it is essentially zero in the $q=0^+$ case. This introduces a slight change in the temperature dependence of the predicted q=0 mode for Tb because the temperature dependences of the crystal field and the second-order magnetoelastic energy are different (19), but the difference is so slight as to be negligible within data scatter in our experiments (8). Even the equation known as the transcendental equation derived from the original Hamiltonian at equilibrium to determine the orientation of the spins with respect to an external applied magnetic field is unchanged by the inclusion of the second-order magnetoelastic energy because the second-order magnetoelastic energy has the same angular dependence in the hexagonal plane as the crystal field hexagonal anisotropy energy (7, 8).

After the first-order magnetoelastic energy is minimized with respect to the instantaneous strains, the diagonalization of the spin Hamiltonian to obtain the spin wave energies proceeds as outlined in Reference (9). The Holstein-Primakoff (23) approximation is applied, which is good for large spin values. Tb has a spin value of 6 on each ion, which is certainly large. Only terms to second-order in the Holstein-Primakoff operators are retained in the spirit of the harmonic oscillator approximation of small spin deviations from equilibrium. A Bogoluibov transformation to true spin wave operators of the system is then effected by considering the true operators to be a certain linear combination of the

Holstein-Primakoff operators and going through steps leading to a secular determinant for obtaining the spin wave energies.

The Tb spin wave energy for the q=0 uniform mode excited in our experiment can be written (8, 9, 10)

$$\hbar\omega = \{[-2P_2S I_{5/2}\sigma^{-1} + 3c^{\gamma}A(0)C(0)\cos 6\theta I_{9/2} I_{5/2} g\mu_B M^{-1}$$

$$+ g\mu_B H_{dc}\cos(\beta-\theta) + g\mu_B M(N_x-N_z) + \Delta_+ I^2_{5/2}\sigma^{-1}]$$

$$\times [18c^{\gamma}A(0)C(0)\cos 6\theta I_{9/2} I_{5/2} g\mu_B M^{-1} + g\mu_B H_{dc}\cos(\beta-\theta)$$

$$+ g\mu_B M(N_y-N_z)]\}^{\frac{1}{2}} \quad . \qquad (1)$$

Here $I_{(\ell+\frac{1}{2})/2}$ is the ratio of the hyperbolic Bessel function of order $\frac{1}{2}(2\ell+1)$ to that of order $\frac{1}{2}$ where the argument of the Bessel functions is Z, where $L(Z)=\sigma$, L is the Langevin function, and σ is the ratio of the magnetization M at temperature T to that at T=0. P_2S is the two-fold crystal field anisotropy constant, c^{γ} is an elastic stiffness constant in the notation of Callen and Callen (19), C(0) and A(0) are the first and second-order magnetostriction coefficients in the notation of Rhyne and Legvold (18), g is the Landé factor, μ_B is the Bohr magneton, Δ_+ is a magnetoelastic term in the notation of Vigren and Liu (10), N_x, N_y and N_z are the demagnetizing factors for a thin disk sample with the c-axis normal and $\vec{H}_{dc}$ (the external magnetic field) in the plane of the disk ($z\|\vec{M}$ and $y\perp\vec{M}$ in the plane of the disk, and $x\|$c-axis), and β and θ are

angles measured from the nearest b-axis (easy axis) to $\vec{H}_{dc}$ and $\vec{M}$, respectively (β and θ have values between 0^o and 30^o).

For a given value of β, the angle θ is given implicitly as a function of H_{dc} by a transcendental equation obtained by minimizing the equilibrium energy of the spin wave Hamiltonian in the molecular field approximation with respect to θ (8, 9, 10):

$$18c^{\gamma}A(0)C(0)I_{9/2}I_{5/2}g\mu_B M^{-1}\sin 6\theta = 6g\mu_B H_{dc}\sin(\beta-\theta) \quad . \qquad (2)$$

Note that Equation 2 is solved for any value of H_{dc} when $\beta=\theta=0$ (magnetic field along an easy $\langle 10\bar{1}0\rangle$ direction or b-axis), and for $H_{dc} = 18c^{\gamma}A(0)C(0)I_{9/2}I_{5/2}M^{-1}$, sometimes referred to as the spin-flip field, when $\beta=\theta=30^o$ (magnetic field along a hard $\langle 11\bar{2}0\rangle$ direction or a-axis). Observe that when H_{dc} along a $\langle 11\bar{2}0\rangle$ direction reaches the spin-flip field, $\hbar\omega=0$ from Equation 1 assuming $N_y=N_z$. For H_{dc} in the hexagonal plane of the sample the demagnetizing field is always parallel to the equilibrium direction of $\vec{M}$, and so does not enter in Equation 2. If the uniform mode extends throughout the sample, then $N_y=N_z$, $N_x=4\pi-2N_z$, and N_z can be obtained from tables (24). If the uniform mode is randomized after a certain coherence depth into the sample in the c-direction due to interactions with phonons or other reasons, then $N_y<N_z$ where N_z still has the same value from the tables as in the previous case where the uniform mode extended throughout the volume of the sample. N_y decreases in value because the randomization process decreases the effective thickness of the sample in which transverse components of the magnetization (M_x and

M_y) act coherently. N_y could be determined from the tables (24), but for a smaller effective sample thickness. Let $N_y=N'$ for this case; then the other transverse demagnetizing factor has the value $N_x=4\pi-2N'$ because $N_x+N_y+N_z=4\pi$ and $N_y=N_z=N'$ in the effective thickness of the sample. In Equation 1 the demagnetizing factors become $N_x-N_z=4\pi-2N'-N_z$ and $N_y-N_z=N'-N_z$. If the coherence depth is small, then $N'\cong 0$ and we have a potentially noticeable but small effect in our experiment because in the second factor of Equation 1 the demagnetizing effects are no longer zero. By making the samples thin, however, all demagnetizing effects are negligible experimentally. In the above reasoning, the condition $N_x+N_y+N_z=4\pi$ is not satisfied for the sample as a whole when a coherence depth is considered. This is because in the classical equations of motion formalism used to obtain the demagnetizing effects on Equation 1, the magnetization is treated as a microscopic quantity which oscillates like a single spin (22), whereas demagnetizing factors affect only the macroscopic magnetization. Rather than change the formalism we simply compensate for the coherence depth by adjusting the values of the demagnetizing factors when in fact it is the macroscopic magnetization that is changing.

Actual numbers for the quantities in Equation 1 are given in References (8) and (10). In both these references the value for $18c^{\gamma}A(0)C(0)g\mu_B M_o^{-1}$ where $M_o=M(T=0)$ is the same as the value given for $-36P_6^6S^5$. $P_6^6S^5$ is strictly speaking the six-fold crystal field anisotropy constant which was found to be zero in Tb (7). However, the experimentally determined hexagonal anisotropy determined by Rhyne and Clark (6) (which

includes six-fold anisotropy due to crystal field and second-order magnetostriction) was all lumped numerically into the factor $-36P_6^6S^5$. Both References (8) and (10) use the total experimental hexagonal anisotropy given by Reference (6) in their numerical results rather than evaluating $18c^{\gamma}A(0)C(0)g\mu_B M_o^{-1}$ term by term. Cooper (8), however, does make a crude estimate of c^{γ} giving him a value for $18c^{\gamma}A(0)C(0)g\mu_B M_o^{-1}$ about 70% larger than the experimental value of Rhyne and Clark (6). The value of Rhyne and Clark explains our experimental results very well, so it is undoubtedly the correct value to use in Tb calculations. The magnetization data of Hegland et al. (5) is used to determine M and σ as a function of temperature. In Equation 1, using the values of Vigren and Liu (10), $-2P_2S = 63.6$ K, so if we define H_A by $g\mu_B H_A = -2P_2S$, we have H_A=632 kOe in an effective field formulation. Similarly, $18c^{\gamma}A(0)C(0)g\mu_B M_o^{-1} = 3.4$ K, so if we define H_h by $g\mu_B H_h = 18c^{\gamma}A(0)C(0)g\mu_B M_o^{-1}$, we get H_h=34 kOe. The value for Δ_+ is $\Delta_+ = -8.0$ K, which makes a contribution to the first factor in Equation 1 and corresponds to an effective field of -80 kOe.

C. Sample Preparation

Two disk-shaped samples with the c-axis normal were used in this experiment. One of them was the same as the thinner crystal reported in previous work (17), except that its dimensions were changed to 5.9 mm diam and 0.3 mm thickness. This sample was used only for the data taken at T=143 K and 161 K because it was the thinner of the two samples made and so was least subject to demagnetizing effects affecting domain alignment.

(The resonance field depends on the domain alignment field at T=143 K and 161 K.) Data at all other temperatures were taken on a sample having 9 mm diam and 1.2 mm thickness cut from the same large crystal as the first sample. From Bozorth (24), the demagnetizing factors are N_z= 0.628 for the thinner sample and N_z=1.13 for the thicker sample. The dimensions of the samples were measured directly with a micrometer after all data were taken.

The large crystal from which our Tb samples were prepared was grown by W. J. Nellis according to a method developed by Nigh (25). A button about 3 cm diam and 1 cm thick of pure Tb metal was prepared at the Ames Laboratory, Iowa State University, using ion-exchange separation (26). Table 1 gives an impurity analysis of this metal. The button was annealed

Table 1. Tb sample impurities in ppm by weight

Al 30	Er -	Mn -
Ca 60	Fe <50	Mo -
Co -	Gd <200	N 3
Cr 300	H 5	Ni <20
Cu 100	Ho -	O 160
Dy <100	Mg <10	Sc -
Si <20	Ta <200	W 500
Sm T	Tm -	Yb FT

Symbols: T = trace, FT = faint trace. A blank space means the element was not investigated.

Tb sample resistance ratio: 54.5

at 1250°C for 12 hours, producing several large single crystals in the button. The crystals were then X-rayed using the Laue technique to locate the crystal symmetry axes. The crystals are glued to a goniometer using a conducting glue made of a mixture of Duco cement and graphite. Once a desired crystal direction is determined the goniometer can be transferred to a spark cutting machine where, by using a moving wire cutter for the flat cuts and a cylindrical cutting tool for the circular cut, a thin disk sample can be produced with the desired orientation. The glue needs to be conducting so the sample will be electrically grounded to the case of the spark cutting machine.

In order to get effective coupling between the microwaves and the sample spin system it is necessary that the sample have a microscopically smooth surface. We achieved an acceptable surface by first using 600 grit sandpaper to reduce the surface crystal damage due to spark cutting. The lapping tool was developed by J. R. Cleveland (27) and consists of a plunger slip-fitted into a thick walled circular cylinder. A flat sample surface is glued to the plunger using beeswax for an adhesive (the wax melts at 100°C). The weight of the plunger holds the sample with uniform weight against the sandpaper, and the cylinder keeps the sample orientation constant with respect to the sandpaper. A figure eight motion is the lapping technique used. The sample is removed from the plunger simply by melting the beeswax.

The sample is next electropolished (28) to remove the surface damage due to the 600 grit sandpaper and produce a microscopically smooth surface. The solution used is 6% perchloric acid by volume into 94%

methanol after the methanol has been cooled to -70°C by an acetone-dry ice bath. A current of about 0.2 amps per square centimeter is passed through the sample in the perchloric solution using a 50 volt power source while the solution is stirred by a magnetic stirrer (the sample is the positive electrode and the metal beaker or a metal post is the negative electrode). A polishing time of one or two minutes is usually sufficient to prepare the surface for mounting in the microwave cavity. This mounting is accomplished as rapidly as possible so that oxidation in the air is kept to a minimum. Whenever possible the polished sample is maintained in a vacuum. A small scratch is made on the back of the sample corresponding to one of the crystallographic directions to aid in orienting the sample with respect to the cavity.

D. Apparatus

1. Description

Figure 1 gives a block diagram of the apparatus used. The system is a conventional reflection spectrometer employing a magic tee (Microwave Associates Model 884) and a crystal detector (1N26 crystal in an Aircom Model 156K holder). The klystron (OKI Model 24V10A) was locked onto the cavity frequency by means of a phase-sensitive automatic frequency control (AFC) which modulates the output frequency of the klystron at 70 KHz (Teltronics Model KSLP). The crystal converts the power reflected from the cavity into a dc voltage with a 70 KHz ac component superimposed because the crystal will respond to 70 KHz. The 70 KHz signal amplitude is proportional to the magnitude of the derivative

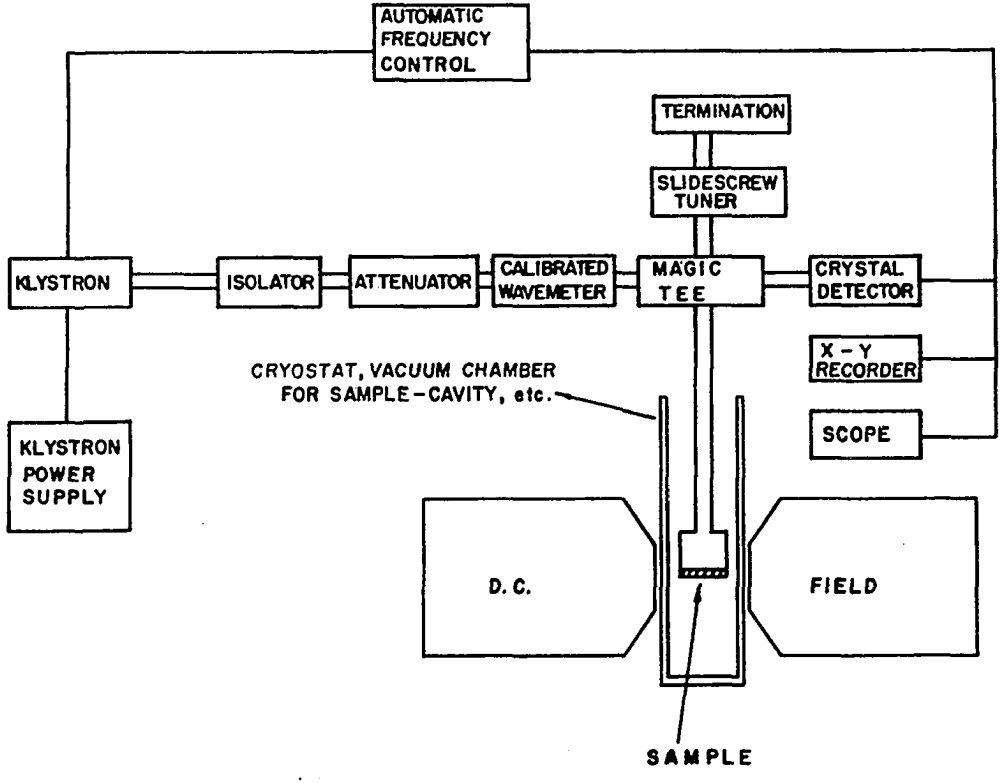

Figure 1. Block diagram of 24 GHz spectrometer system.

of the power reflected vs microwave frequency characteristics of the cavity, and at resonance this derivative is zero. The derivative increases rapidly in magnitude away from resonance because of the large cavity Q. Because the derivative changes sign when the klystron frequency goes from slightly above to slightly below the cavity resonance frequency, the phase of the 70 KHz output signal also changes sign when the klystron frequency goes from slightly above to slightly below the cavity resonance frequency. The amplitude of the 70 KHz signal is therefore proportional to the change in frequency necessary to make the klystron frequency coincide with the resonant frequency of the cavity, and the phase of the signal tells the AFC whether the klystron frequency should be increased or decreased.

The isolator (Microwave Associates Model 161) gives the klystron about 20 db of isolation from the reflected microwave power for increased klystron stability. The klystron (powered by a Polytechnic Model 812 power supply) was air cooled and was stable enough for our experiments after it was warmed up for a period of $\frac{1}{2}$ hour. The frequency meter was a calibrated high-Q cavity resonator that gives frequency to about 2% accuracy (Microwave Associates Model 588). The attenuator was calibrated and gave about 20 db maximum attenuation (Microwave Associates Model 587). A good crystal (one with low noise) was found by trial and error. When maximum sensitivity was desired, the klystron was operated at a full power of about 0.15 - 0.20 watts (see next section for theory of sensitivity), and the slide screw tuner (Waveline Model 883) and magic tee arrangement were used to buck down the

microwave power incident on the crystal. The bucking provided by the slide screw tuner and magic tee also partially cancelled out klystron noise (29). The optimum crystal current for low noise was found to be about 40 μa using our AFC which has 1000 ohms input impedance. At 40 μa the crystal is probably operating in the linear region (29), which means that the rectified output current is proportional to the square root of the incident power. In some cases (particularly in some experiments with erbium metal) when lower crystal current was used, the crystal was probably operating in the square law region (29), which means that the output current is directly proportional to the incident power. Since the characteristics of crystals are not constant from one crystal to the next, we do not know the exact characteristics of the crystals used in our experiment. It should be noted, however, that the exact characteristics of the crystal used are not very important because we experimentally observe only the small change in power absorbed by the sample due to magnetic losses (spin wave resonance) when the external applied field is at a certain value. Because this change in power absorption is small, the change in crystal voltage (or current) accompanying the change in power absorption varies essentially linearly with the change in power absorption no matter what the crystal characteristics are. We estimate roughly that spin wave resonance in Tb at 24 GHz causes about a 10% increase in power absorption in our microwave cavity. This corresponds to a change in absorption of almost 1 part in 10^5 for simple reflection of microwaves from the sample with no cavity.

There were no problems due to saturation of the spins in the samples

studied in this experiment (saturation meaning that application of microwave power above a certain level is ineffective in further exciting the spin system because all the spins in the skin depth of the sample are already excited), so high microwave powers were possible. The large magnetic field linewidths in the power absorbed vs magnetic field plots associated with spin wave resonance in Tb and Dy can be related to a phenomenological relaxation time for the decay of an excited spin state of about 10^{-12} seconds for Dy (12) and a similarly short relaxation time for Tb. This implies extremely heavy damping of the magnetic system. Because the spins relax so rapidly to their equilibrium positions after being excited, there are always enough spins in an unexcited state so that saturation is not observed, even at relatively high microwave power.

In order to observe the cavity mode on the oscilloscope, the frequency of the klystron was modulated at 60 Hz. (The 60 Hz modulation was removed before the AFC was locked to the cavity frequency.) The correct bucking up or down of microwave power incident on the crystal was obtained by first introducing the probe of the slide screw tuner into the waveguide until the effect on the cavity coupling was just visible. The phase of the probe was then adjusted so that the cavity was effectively coupled either a maximum or a minimum amount. The probe was then introduced further into the waveguide until the desired crystal current was obtained. In this manner the cavity could be effectively undercoupled or overcoupled. (At times coupling in one direction or the other seemed to decrease noise.) The dc output signal is inverted when the effective cavity coupling goes from overcoupled to undercoupled or vice versa, so

care must be taken that the crystal current does not go to zero while a run is being made. (The crystal current goes through zero when the cavity changes its coupling.) We measured direct absorption as a function of applied field because our noise was low enough that we did not need to modulate the dc magnetic field.

The magic tee is constructed by connecting waveguides in shunt and series with a collinear guide at the same point (30). The series connection is also called an E-plane junction, and the incident microwave power is fed into the series connection. If the two arms of the collinear guide are terminated in matched loads (i.e., the slide screw tuner is used to critically couple the cavity in our experiment), the power will divide equally between the two arms and there will be no coupling between the series and shunt arms because no electric vector is developed across the entrance to the shunt arm. (When the power divides equally between the two arms of the collinear guide, the electric vectors are 180° out of phase at equal and opposite distances from the junction, and the electric vectors reflected from the two matched loads cancel when they meet at the junction.) Note that klystron noise is also cancelled at the junction when the loads are matched. When the two loads on the collinear guide are no longer matched (i.e., the cavity is overcoupled or undercoupled), the electric vectors at the entrance to the shunt arm will no longer completely cancel, and there will be energy transfer to the shunt arm. The crystal is attached to the shunt arm (also called the H-plane arm), so our experiment measures the difference between the power absorbed in the cavity and the constant power absorbed

by the slide screw tuner arm of the magic tee. It is evident that the magic tee has many of the qualities of a bridge circuit. A further refinement is the introduction of matching structures near the magic tee junction so that the wave impedance of the series and shunt connections is the same as the wave impedance of the collinear guide for maximum power transfer at the junction (30).

The x-y recorder (Moseley Model 7000A) is preceded by a low pass filter and a dc amplifier (built by John Hartman) with a zero-suppress (built by Dave Newquist), and is used to record changes in the dc component of the crystal output. The magnetic field is swept slowly enough that the artificial hysteresis due to the time constant of the low pass filter does not affect the field positions of the absorption peaks going up and down in magnetic field. The field sweep (built by Kerry Nelson) is controlled by an electric motor, and the magnetic field is measured by a Rawson rotating coil gaussmeter placed between the poles of the magnet along with the dewar-cavity system.

Figure 2 gives a diagram of the 24 GHz cavity and associated components. The circular cavity was designed to operate in the TE_{111} mode. The approximate formulas used to determine cavity dimensions are given by Harrington (31) and will be discussed in the next section. The TE_{111} mode is degenerate with respect to rotation of the microwave fields about the cavity axis. In order to lift this degeneracy, a small dent inward was made in the wall of the cavity about half way between the top and bottom. This dent produces two orthogonal TE_{111} modes separated slightly in frequency (31) because the dent makes the cavity

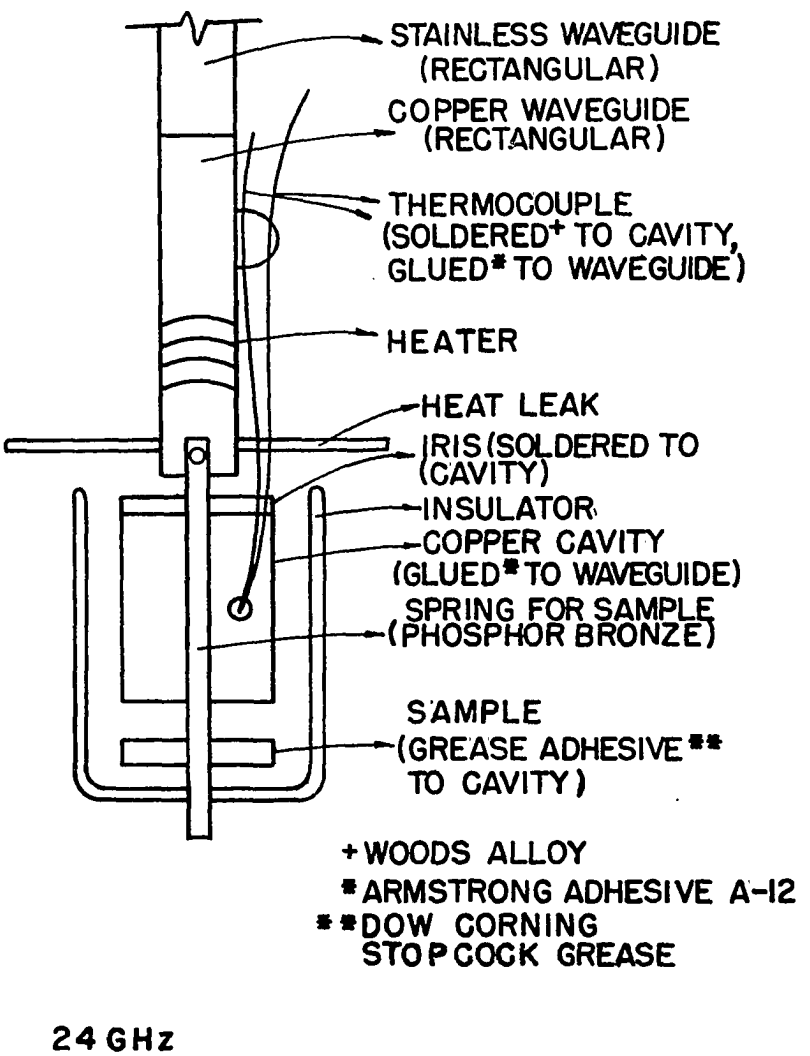

Figure 2. Diagram of 24 GHz microwave cavity.

somewhat "elliptical," and a true elliptical cavity has this property (30). At the bottom and top of the cavity, the rf magnetic field (H_{rf}) of either one or these two modes is almost linear and perpendicular to the axis of the cavity. Our cavity had an i.d. of 0.323 in. and a length of 0.539 in. and was soldered to a coupling iris about 0.010 in. thick with a centered coupling hole of 0.128 in. diam. The cavity was positioned on the waveguide so that both orthogonal modes were equally coupled and almost critically coupled. The lower frequency mode was used throughout the course of the experiment, but both modes gave equivalent results.

The sample formed the base of the cavity for the data using the thicker sample as shown in Figure 2. The sample was made thick enough that strain due to spring loading could be avoided. The b-axis of the sample was aligned approximately parallel to H_{rf} of the lower frequency of the two orthogonal TE_{111} modes. This means that an a-axis was parallel to a diameter of the cavity drawn with one end intersecting the dent. At low temperatures Dow Corning stopcock grease made a good adhesive because it adheres to the sample and cavity well enough to prevent slipping, but does not solidify to the extent that small expansions or contractions strain the sample. This is important in Tb at low temperatures because the magnetic ordering in the basal plane exerts a torque on the sample. The external magnetic field could be aligned in any direction in the plane of the sample, so that all angles between H_{rf} and H_{dc} could be realized in this plane.

The thinner sample was glued with GE 7031 varnish to a circular

copper plate about 0.020 in. thick and surrounded by a copper washer described below, and this assembly was then spring loaded to the cavity much like the thicker sample. Instead of grease, however, masking tape placed on the back of the plate and attached to the cavity was used to prevent slipping of the plate and washer assembly. The copper washer had an o.d. the same as the copper plate, an i.d. slightly larger than the sample diameter, and thickness about the same as the sample thickness, and was mounted along with the sample so that the sample perturbed the symmetry of the cavity as little as possible. The washer was held in place by friction due to the spring loading.

In Figure 2, the insulator (masking tape) was used to maintain electrical isolation of the cavity so the copper-constantan thermocouple could be soldered directly to it, thereby giving a good thermal connection between the sample and thermocouple. The thermocouple was glued to the waveguide to provide a sink for heat coming down the wires from the top of the dewar. A second thermocouple was placed under the heater wires to control the heater current and maintain the copper waveguide at a desired temperature. The output from this thermocouple was balanced against the emf corresponding to the desired temperature using a potentiometer, and the difference emf was amplified (using a dc amplifier built by Dr. T. K. Wagner) and used to supply the heater current. (The heater was made of manganin wire with 30 ohms resistance.) In this manner the temperature could be made stable over long periods of time.

The heat leak (see Figure 2) drained the heat conducted down the stainless steel waveguide and the wires into the liquid nitrogen bath by

making good contact with the walls of the stainless steel vacuum jacket in which the apparatus shown in Figure 2 was placed. The liquid nitrogen (or liquid helium) was maintained by a conventional stainless steel dewar designed by J. R. Cleveland consisting of two vacuum spaces isolating two chambers where refrigerants could be introduced. The stainless steel vacuum jacket containing the apparatus was immersed in liquid nitrogen in the innermost of these two chambers. (Helium transfer gas at a pressure of 100 μ or so in the vacuum jacket maintained the sample at the bath temperature if desired.) Mylar plastic transmits microwaves, and was therefore used to seal the waveguide entering the vacuum jacket. Armstrong adhesive A-12 was used to seal the wires entering the jacket. The top of the jacket itself was sealed with an O-ring. The "tail" of the dewar containing the cavity was just large enough to fit between the poles of the magnet. The pole spacing of the Magnion magnet used is $1\frac{3}{8}$ in.

2. Electromagnetic calculations

The approximation used in most waveguide and cavity calculations is that the metal walls are infinitely good conductors. A good estimate of the power loss in the conductor walls can be obtained to a first approximation by considering that the fields calculated for the infinitely good conductor case generate the eddy currents in the real metal walls which dissipate the power. The rectangular waveguide used in this experiment has inside dimentions 0.170 in. X 0.420 in. The cutoff frequencies for the various modes are given by (31)

$$f_{mn} = c/2(m^2/a^2 + n^2/b^2)^{\frac{1}{2}} \tag{3}$$

where c is the speed of light, and a is the long dimension and b is the short dimension of the cross section of the rectangular waveguide. The two lowest cutoff frequencies are f_{10}=14.1 GHz and f_{20}=30 GHz and correspond to transverse electric (TE) waveguide modes. For the waveguide to operate exclusively in the TE_{10} mode (a desirable condition for exciting a consistent mode in the cavity), the klystron frequency must be between 14.1 - 30 GHz. The recommended operating range of this waveguide in the TE_{10} mode is 18 - 26.5 GHz, somewhat less than the theoretical limits and including our experimental frequency of 24 GHz.

If the length of a circular microwave cavity is greater than its diameter, the lowest frequency mode excited is the TE_{111} mode with a frequency given by (31)

$$f_{111} = c/2\pi a(3.39 + \pi^2 a^2/d^2)^{\frac{1}{2}} \tag{4}$$

where c is the speed of light, d is the cavity length, and a is the inside radius of the circular cavity. The dimensions of our cavity given in the previous section correspond to f_{111}=24 GHz. The fields in the TE_{111} mode at the end of the cavity where the sample is located are given by

$$H_\rho = H_o J_1'(1.841\rho/a)\sin\phi$$

$$H_\phi = H_o[a/(1.841\rho)]J_1(1.841\rho/a)\cos\phi \quad . \tag{5}$$

Here H_o is a constant with units of magnetic field, and ρ and ϕ are polar coordinates on the surface of the sample where $\rho=0$ is the cavity axis and ϕ is the polar angle measured from any arbitrary cavity diameter. (Note the degeneracy of field direction mentioned in the previous section.) The function J_1 is the Bessel function of the first kind of order 1, and $J_1'(x)$ is the derivative of $J_1(x)$ with respect to x (when $\rho=a$, $J_1'=0$ in Equation 5). Note that there are no electric fields acting on the sample. In order to uniquely determine the $\phi=0$ axis, a small inward dent was made in the side of the cavity as described in the previous section. If the $\phi=0$ axis is taken as the projection on the sample surface of a cavity diameter that intersects the dent, then Equation 5 describes the lower frequency of the two orthogonal modes excited by the dent (the higher frequency mode is given by interchanging $\sin\phi$ and $\cos\phi$). An outward dent instead of an inward dent would cause Equation 5 to represent the higher frequency of the two orthogonal modes excited if the $\phi=0$ axis remained the same. For an inward dent the higher frequency mode is shifted upward in frequency from the original unperturbed frequency by an amount (31)

$$\Delta\omega = \frac{2.86\omega_o}{1+2.92a^2/d^2} \left| \frac{\Delta\tau}{\tau} \right| \tag{6}$$

and the lower frequency mode is shifted downward in frequency from the original unperturbed frequency by an amount (31)

$$\Delta\omega = 0.843\omega_o \left| \frac{\Delta\tau}{\tau} \right| \tag{7}$$

where ω_o is the unperturbed frequency, a is the cavity radius and d is the cavity length (d>2a). τ is the unperturbed cavity volume and $\Delta\tau$ is the small change in cavity volume due to the dent. For an outward dent Equations 6 and 7 would change to a downward and an upward shift in frequency, respectively, from the unperturbed frequency. Equations 6 and 7 were obtained by doing a perturbation calculation on the cavity frequency which assumes Equation 5 is unchanged by the presence of the dent. The complete configuration of fields acting on the sample can therefore be determined by knowing the orientation of a sample crystallographic axis with respect to the cavity dent. It should be noted that for both orthogonal cavity modes to be equally coupled to the incoming microwave energy (as was the case in our experiment), the cavity diameter passing through the dent should make an angle of about 45^o with the direction of the electric field in the TE_{10} mode of the connecting waveguide. (The electric field of the TE_{10} mode is parallel to the short dimension of the rectangular cross section of the waveguide.) The size of the coupling

hole in the iris given in the previous section was determined experimentally by enlarging the hole until the cavity modes were almost critically coupled without using the slide screw tuner.

A cavity was used in these experiments because the power absorbed per unit volume due to magnetic losses in a sample is given by (29)

$$P = \frac{1}{2}\omega H_1^2 \chi'' \tag{8}$$

where H_1 is some sort of average rf magnetic field in the skin depth of the metallic sample, $\omega=2\pi f$ where f is the frequency, and χ'' is the imaginary part of the rf susceptibility. Since χ'' is not a function of H_1 for the microwave power used in this experiment (saturation effects are not observed as discussed in the previous section), the larger the value of H_1 the greater the power absorbed and the greater the sensitivity of the spectrometer. A cavity effectively increases the value of H_1 by storing microwave energy in the cavity volume. A more detailed analysis using an equivalent circuit representation for the reflection spectrometer (29) shows that the change in power absorbed by the cavity due to magnetic losses in the sample is proportional to $\chi'' P_o Q_o$ where P_o is the microwave power available to the cavity from the klystron and Q_o is the unloaded Q of the cavity. It is interesting to note that the term $\chi'' P_o Q_o$ contains the large theoretically determined unloaded Q of the cavity (by definition due to losses in only the sample and cavity) rather than the smaller experimentally observable loaded Q of the cavity (by definition including losses from power leaking out of the cavity

through the iris in addition to the losses considered in determining Q_o).

Q_o is determined theoretically be dividing the energy stored in the cavity by the average energy dissipated per cycle in both the sample and the rest of the cavity where the coupling iris is mathematically replaced by a copper plate. Of course χ'' becomes non-zero in Tb principally when spin-wave resonance occurs, so the power absorbed by the cavity due to spin-wave resonance is multiplied by the factor Q_o when a cavity is used. In order to get an idea of the magnitude of Q_o, we use the expression on page 257 of Harrington (31) to obtain $Q_o \cong 7000$ for a circular cavity made of copper operating in the TE_{111} mode at room temperature with our cavity dimensions as given in the previous section. (We neglected the large resistivity of the Tb sample in this calculation by mathematically replacing it with copper when calculating Q_o.) If we include the Tb sample in the calculation at T=300 K by using the resistivity data for Tb of Colvin et al. (32), we obtain $Q_o = 5150$. At lower temperatures, of course, the resistivity of Tb decreases, so $Q_o = 5150$ can be taken as a lower limit on the value of Q_o in our experiments.

E. Experimental Results

The data were taken by measuring direct microwave absorption as a function of temperature, microwave polarization, magnetic field, and crystallographic orientation of the sample. The figures which follow generally present schematically the experimental configuration corresponding to the data shown. Figure 3 gives examples of some of the data. Comparisons of relative signal amplitude are valid between curves

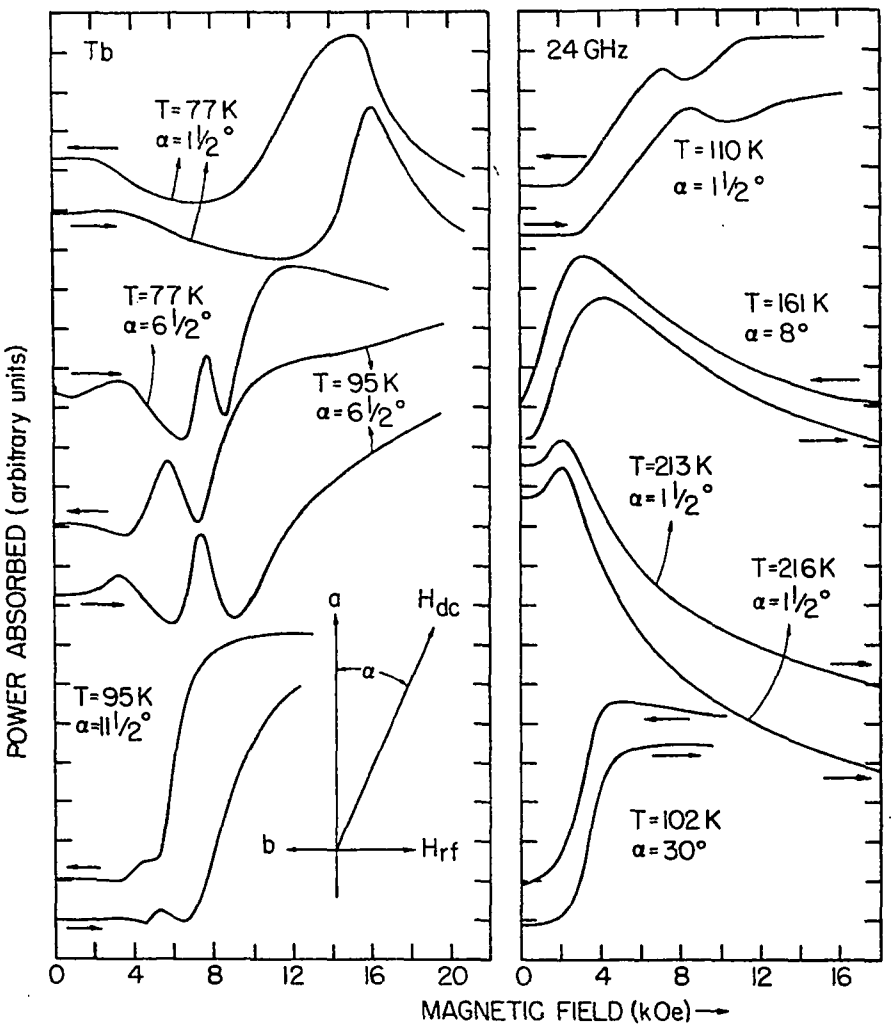

Figure 3. Tracings of typical power absorption vs applied magnetic field data for Tb.

at the same temperature. At T=77 K, $\alpha=1\frac{1}{2}^{o}$ there are large microwave absorptions in Figure 3. We attribute peaks aligned within two degrees of the a-axis to be due to resonance absorption in Cooper's (8) free lattice model for the following reasons (some of which will be discussed in more detail later): 1. The amplitudes are large, and the linewidths are narrow compared to absorption observed in Tb at 100 GHz by Wagner and Stanford (14), indicating on-resonance absorption. 2. The temperature dependence of the peak is close to the free lattice model (see Figure 4), which departs significantly from that of the frozen lattice model data of Wagner and Stanford (14) at 100 GHz for $T<140$ K. The peaks remain sharply defined (similar in line shape to the T=77 K, $\alpha=1\frac{1}{2}^{o}$ peaks in Figure 3) for $T<110$ K. For $110\text{ K}<T<140$ K the peaks become much broader (see the T=110 K, $\alpha=1\frac{1}{2}^{o}$ peaks in Figure 3), and a second absorption begins to appear at higher fields. At even higher temperatures (see T=161 K, 213 K, and 218 K data in Figure 3) the absorption appears to be along the domain alignment field as determined by magnetization measurements (5), in agreement with Cooper's (8) free lattice model calculated by Vigren and Liu (10). 3. Anomalies in the magnetoresistance and magnetostriction (18) of the heavy rare earth metals (i.e., Tb, Dy, Ho, etc.) are associated with domain alignment and magnetic phase transitions. Since our peaks in power absorption for $T<140$ K occur exclusively in the ferromagnetic phase of Tb above the domain alignment field, they should not be due to changes in background conductivity or magnetostriction. 4. The peak at T=86 K (see Figure 7) has a $\sin^2\phi$ amplitude dependence (where ϕ is the angle between H_{rf} and H_{dc}) as expected for a spin-wave

resonance.

In the preceding discussion the peaks observed were for H_{dc} aligned within a few degrees of the a-axis. When the field is aligned exactly along the a-axis no absorption is observed, contrary to the prediction of Cooper's free lattice model. Our experimental results reveal that peaks with the temperature dependence predicted by Cooper for the free lattice model actually occur for H_{dc} from 1^{o}-2^{o} off the a-axis (see Figure 4).

When H_{dc} is aligned from 3^{o}-10^{o} from the a-axis in the basal plane, two absorptions were observed for all temperatures below T=140 K (see T=77 K, $\alpha=6\frac{1}{2}^{o}$; T=95 K, $\alpha=6\frac{1}{2}^{o}$ and T=95 K, $\alpha=11\frac{1}{2}^{o}$ data in Figure 3). These absorptions are very unusual because Cooper's free lattice model predicts no resonance absorption for H_{dc} aligned from 3^{o}-10^{o} away from the a-axis. The initial peak (at lower field) has a narrow linewidth and is well resolved from the second peak (at higher field) which is a very broad absorption. We assume that both of these peaks might be due to spin wave resonance for many of the same reasons as those listed above for the peaks obtained with H_{dc} aligned within 2^{o} of the a-axis. We will refer to these reasons (listed above) by number. Reason 1. applies to the initial peak because it has large amplitude and narrow linewidth, indicating on-resonance absorption. The second peak has large amplitude but very broad linewidth. We will discuss a possible interpretation of the narrow linewidth of the first peak later, but we do not understand the large width of the second peak. Reason 2. does not apply to the two peaks we are discussing because as previously stated, Cooper's theory

predicts no resonance for H_{dc} aligned from 3^{o}-10^{o} away from the a-axis. We note, however, that the first peak always has a narrow linewidth and the second peak is always very broad for H_{dc} aligned from 3^{o}-10^{o} away from the a-axis. For H_{dc} aligned more than 10^{o} from the a-axis, the resonance field of the first peak begins to disappear below the domain alignment field (see T=95 K, $\alpha=11\frac{1}{2}^{o}$ data in Figure 3). The field dependence of the first peak vs rotation angle of H_{dc} in the basal plane is shown in Figure 8, and will be discussed in more detail later. The field dependence of the second peak is difficult to determine at most temperatures because the width precludes accurate determination of an absorption maximum. The field dependence vs temperature of this peak can be inferred from several examples of the second peak plotted in Figure 3 at T=95 K. Note that the onset of absorption associated with the second peak approaches the domain alignment field as H_{dc} is rotated farther from the a-axis. This general trend for field vs temperature dependence of the second peak was observable for rotation studies at all temperatures below T=140 K. Reason 3. above mentions that anomalies in magnetostriction and magnetoresistance should not be the explanation of the two peaks we are discussing, and applies to the second peak as well as the first peak. Reason 4. does not apply to the second peak because of difficulty in determining its amplitude. We therefore do not know the rotation dependence of the second peak.

Figure 3 shows an onset of power absorption at the domain alignment field with H_{dc} aligned along an easy axis (T=102 K, $\alpha=30^{o}$ data). The open triangles in Figure 4 are a plot of the "knee" of this absorption, which

we interpret as being at least partially due to off-resonance absorption predicted by Cooper (8) at the domain alignment field for $\alpha=30^{o}$. This absorption is predicted and observed at all temperatures covered in this experiment at $\alpha=30^{o}$, and the absorption always appears to occur at the domain alignment field. The absorption is very broad as expected.

Figure 4 gives experimental resonance field values vs temperature at 24 GHz. Triangles with the vertex pointing up or down represent data taken while increasing or decreasing H_{dc} with time, respectively. The letters are as follows: A, calculation by Vigren and Liu of Cooper's free lattice model absorption maxima at 24 GHz for $H_{dc}\|$a-axis. B, prediction by Vigren and Liu of off-resonance absorption maxima at the domain alignment field in Cooper's free lattice model for $H_{dc}\|$a-axis. Off-resonance in this case means the actual resonance conditions are satisfied for a value of H_{dc} below the domain alignment field. Because of the large linewidth of the resonance, its trailing edge is observed for H_{dc} greater than the domain alignment field. The open triangles are the domain alignment field determined by the knee of off-resonance absorption when $H_{dc}\|$b-axis (see $\alpha=30^{o}$ data in Figure 3). $\alpha=30^{o}$ is the case for $H_{dc}\|$b-axis, corresponding to setting $\beta=\theta=0$ in Equation 1 and causing $\hbar\omega$ to become a monotonically increasing function of H_{dc} with an energy too high for on-resonance absorption at 24 GHz at the domain alignment field. C, paramagnetic resonance. The amplitude of these resonances decreases rapidly with increasing temperature. D, region of non-resonance absorption maxima (not plotted) due to domain alignment when using the thicker sample with H_{dc} oriented 1^{o} from the a-axis. The temperature

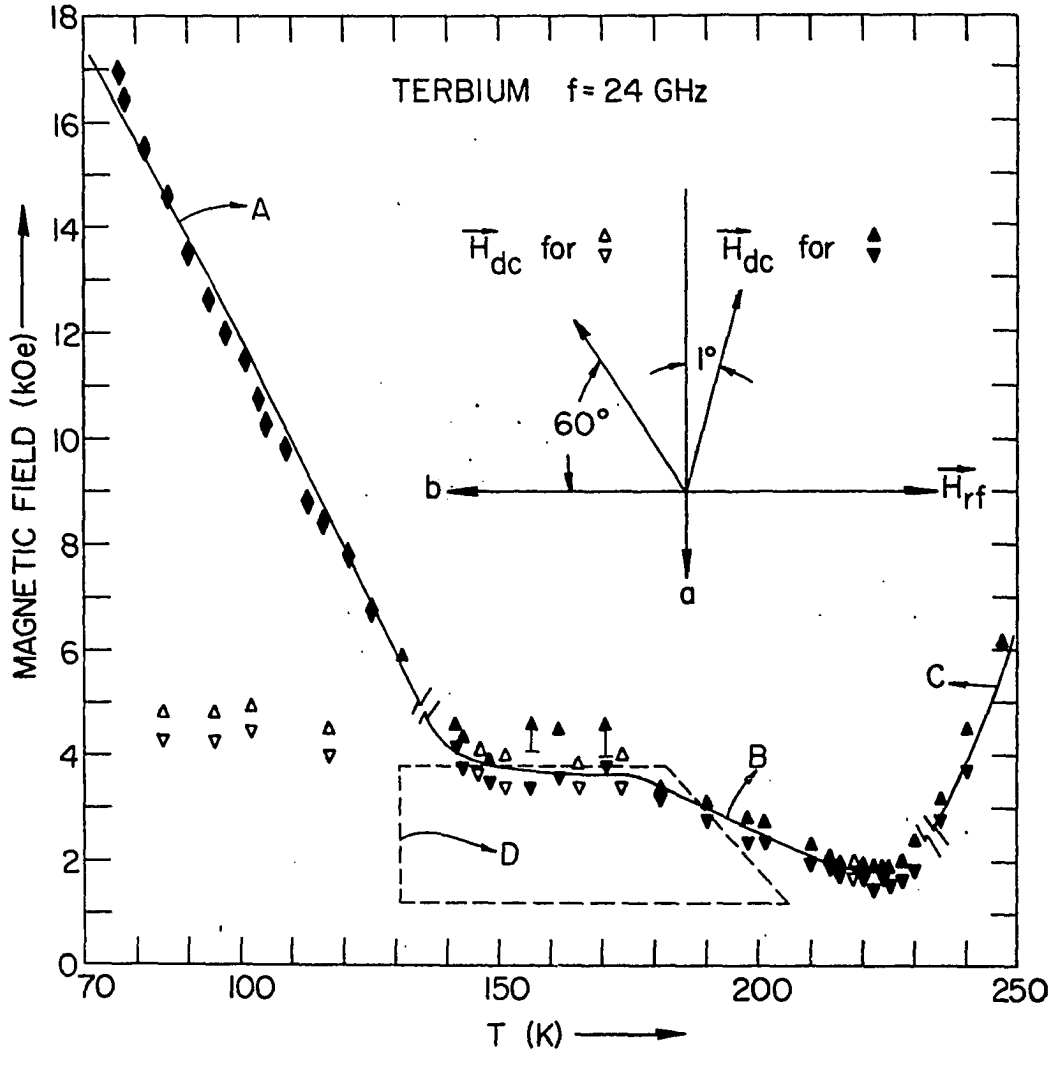

Figure 4. Plot of the field values of power absorption maxima as a function of temperature for Tb.

dependence of the data is in good agreement with the free lattice model calculated by Vigren and Liu. On the basis of these data, we believe the rise in resonance field with decreasing temperature observed by Bagguley and Liesegang (16) in Tb at 10 GHz for temperatures above 140 K was due to a combination of off-resonance absorption and domain alignment effects, and was not an indication of free lattice model behavior. The frozen lattice model interpretation of the data of Wagner and Stanford (17) at 10 GHz for temperatures above 175 K does not contradict the free lattice model interpretation of Vigren and Liu since the two models give similar predictions for T>140 K. The contrast between the 100 GHz Tb data of Wagner and Stanford (14) and our 24 GHz data in Figure 4 is especially evident at T=100 K where for similar experimental configurations (given in Figure 4 for the closed triangles) Wagner and Stanford observed a resonance at 6 kOe (close to the domain alignment field), while Figure 4 shows a strong resonance at almost 12 kOe. These field differences for different microwave frequencies are adequately accounted for by assuming the frozen lattice model applies at 100 GHz and the free lattice model at 24 GHz as predicted by Vigren and Liu. If the frozen lattice model is applied at 24 GHz, all the closed triangles for T<140 K in Figure 4 would be due to off-resonance absorption, and the 100 GHz Tb data for T<140 K would be expected to have almost the same field dependence as the closed triangles in Figure 4, but with even greater intensity (8, 10), which is obviously not the case. The spin wave energy for the $q=0^{+}$ frozen lattice mode is similar to Equation 1, except that a magnetoelastic term $\Delta_{-}I^{2}_{5/2}\sigma^{-1}$ is added to the second factor (15) so that when Equation 1 is

combined with Equation 2, $\hbar\omega$ is always non-zero. Figure 5 is a plot of the q=0 and $q=0^+$ energy gaps versus magnetic field as calculated by Vigren and Liu. All of the 100 GHz data of Wagner and Stanford (14) below T=180 K are explained as off-resonance absorption at the domain alignment field due to the $q=0^+$ frozen lattice mode, and the higher temperature data as on-resonance absorption due to the same mode (10). Recall that the open triangles in Figure 4 give the domain alignment field for comparison with the data of Wagner and Stanford (14) below T=180 K.

Figure 6 gives theoretical power absorption vs magnetic field plots calculated by Vigren and Liu for the uniform q=0 mode. They consider ferromagnetic resonance absorption as an optical pumping experiment by using the "golden rule" to calculate the rate of absorption of quantum $\hbar\omega$ by the spin system in the metal. The experimental q=0 broadening of the spin wave spectrum determined by neutron diffraction (33, 34) was used for the magnon broadening parameter in the result to determine the plots in Figure 6. Comparison between Figures 3 and 6 shows reasonably good agreement between experiment and theory at some temperatures. The low temperature linewidths will be discussed in more detail hereafter. As the temperature increases, so does the broadening of the spin wave spectrum. This causes the decrease in absorption measured between the domain alignment field and H_{dc}=18 kOe to become more pronounced with increasing temperature. In Figure 6, Vigren and Liu predict the decrease in absorption, measured between the domain alignment field and H_{dc}=18 kOe, to be 100% greater at 220 K than it is at 210 K. In this same field interval, we find the decrease in absorption to be 23% greater at 216 K than it is

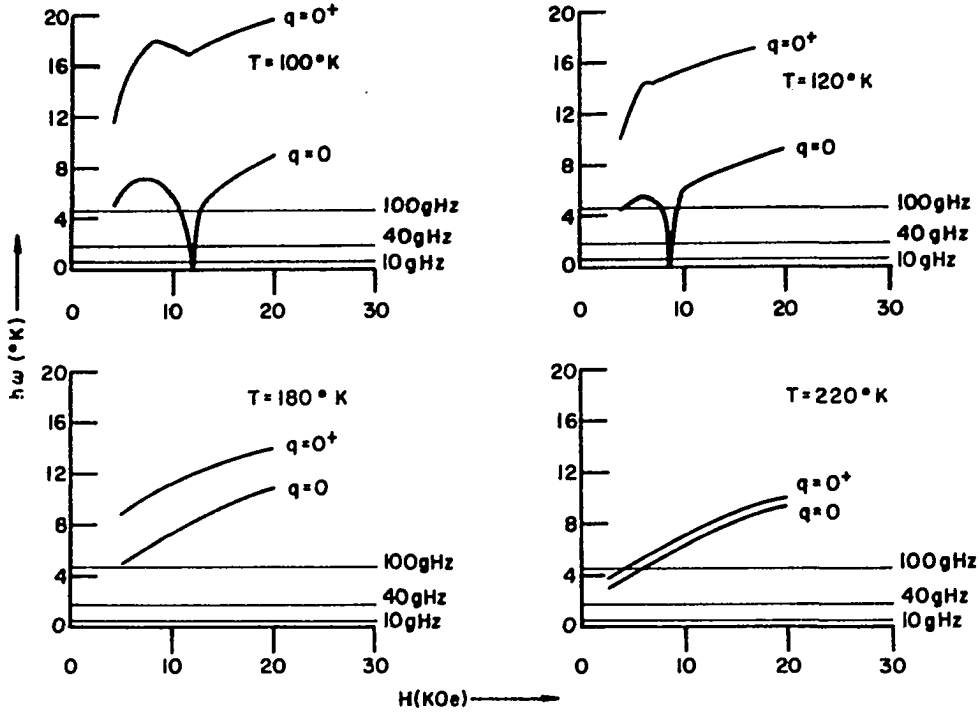

Figure 5. Magnon energy predicted by Vigren and Liu as a function of applied magnetic field in the $\langle 11\bar{2}0 \rangle$ direction of Tb.

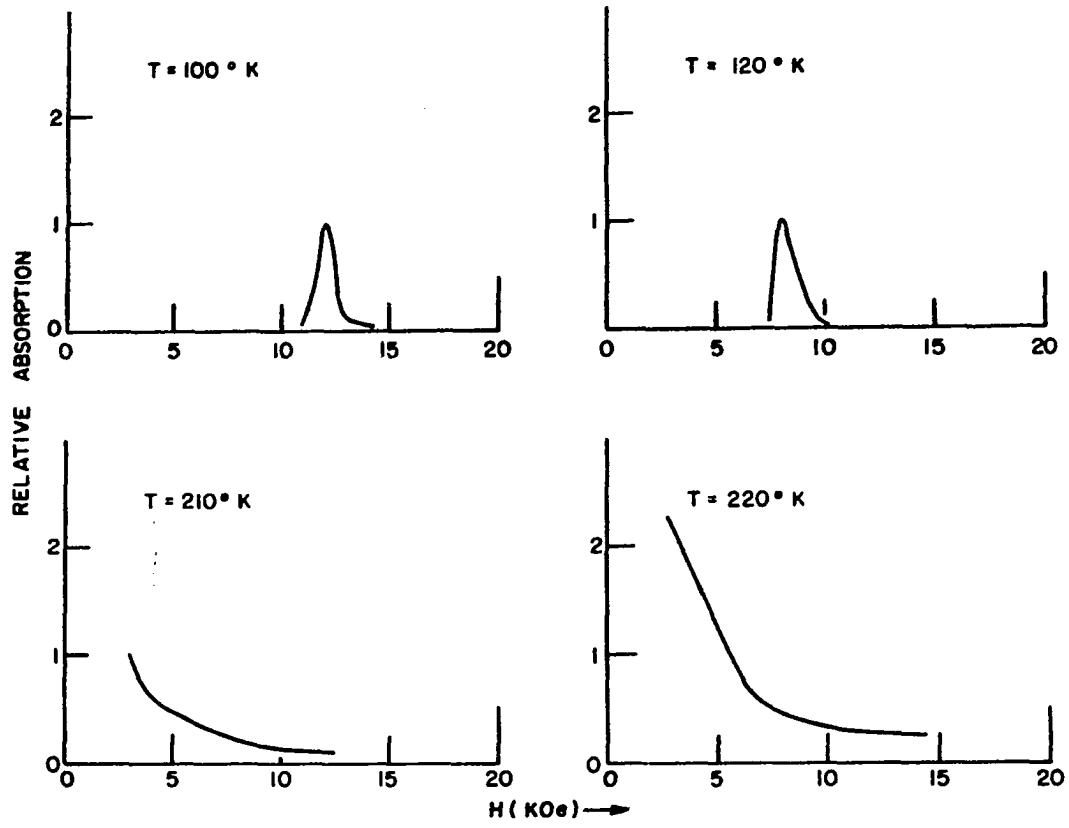

Figure 6. Microwave absorption predicted by Vigren and Liu at 10 GHz for applied magnetic field in the $\langle 11\bar{2}0 \rangle$ direction of Tb.

at 213 K (see Figure 3), in agreement with Vigren and Liu if the difference in temperature interval is taken into account.

Figure 7 shows rotation studies where the signal amplitude is plotted as a function of the angle between H_{rf} and H_{dc}. The zero of amplitude was taken to be that at $H_{dc}=0$, except at T=77 K where the local minimum of power absorption just prior to the onset of resonance was used as the zero of amplitude due to a "background" decrease in power absorption with increasing H_{dc} (see Figure 3). This "background" was not the same in all our experiments for similar experimental configurations. (At times the "background" was an increase in power absorption with increasing H_{dc}.) We do not have a good explanation for this "background" absorption. All data plotted were taken while increasing H_{dc} with time. Comparisons of relative signal amplitude are not valid between data at different temperatures. We note from Figure 7 that the amplitude of the resonance at T=77 K falls off rapidly as $\vec{H}_{dc}$ moves away from the a-axis, but if $\vec{H}_{dc}$ is kept at a constant relation to the a-axis, the amplitude has the $\sin^2\phi$ dependence of a true resonance absorption as shown by the T=86 K data. (The T=86 K data are equivalent to rotating H_{rf} in the diagram by 60° intervals while holding H_{dc} constant.) The higher temperature data will be discussed in more detail later. The absorption amplitude at T=77 K with H_{dc} along a hard $\langle 11\bar{2}0\rangle$ axis ($\phi=90^\circ$) is zero, which explains why the data in Figure 4 were taken 1° away from the a-axis. At all temperatures below 140 K the resonance amplitudes as a function of ϕ were qualitatively similar. Figure 3 shows that for some values of α below T=140 K there are two absorption maxima at a given temperature. Figure 7

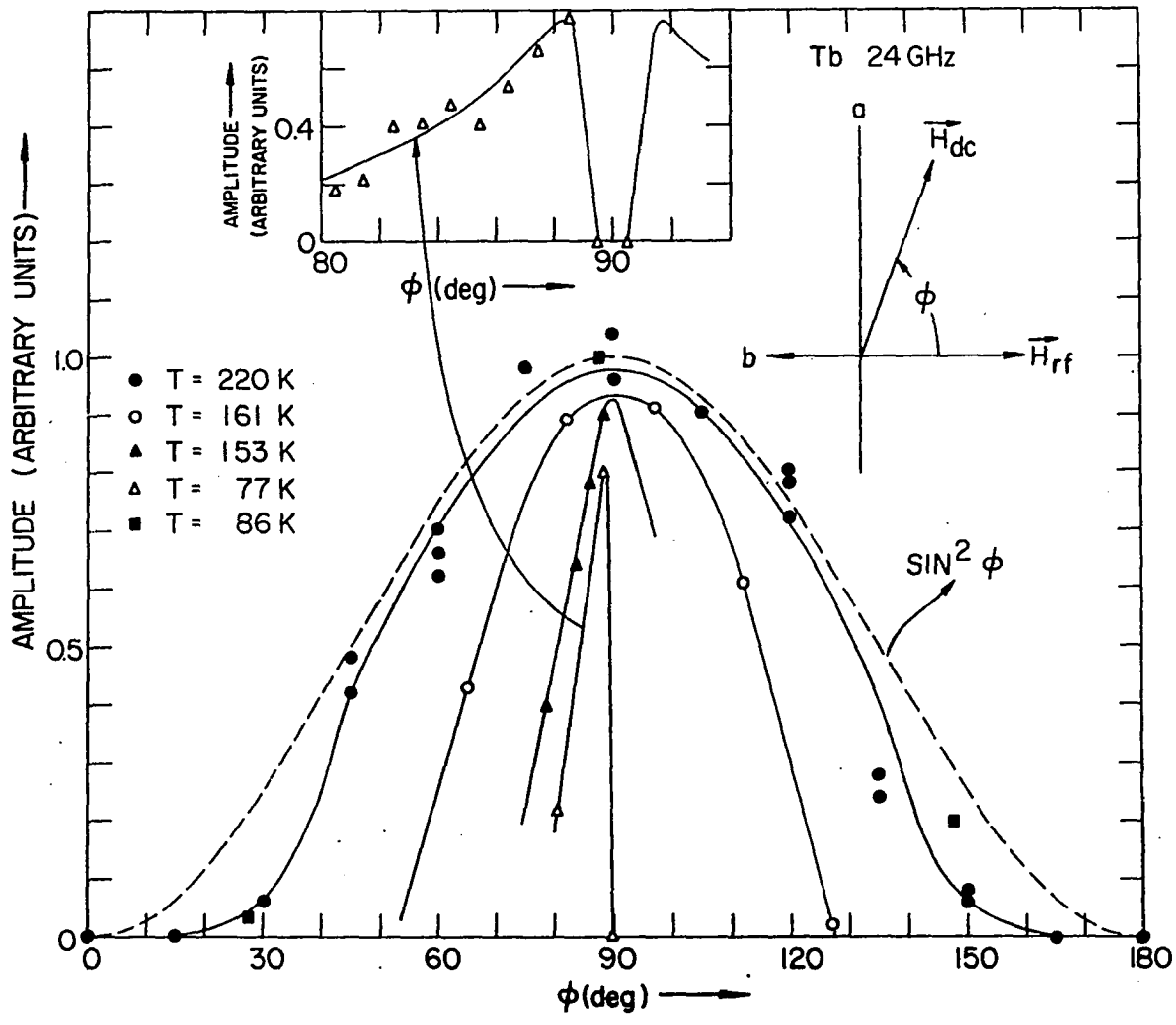

Figure 7. Plot of the amplitudes of power absorption maxima as a function of the angle between H_{rf} and H_{dc} for Tb.

refers only to the lower field maximum. The higher field maximum will be discussed later.

Figure 8 shows rotation studies where the field values of the absorption maxima are plotted as a function of the angle between H_{rf} and H_{dc}. For data taken at T=77 K, the filled triangles with the vertex pointing up or down represent data taken while increasing or decreasing H_{dc} with time, respectively. At all other temperatures the only data plotted were taken while increasing H_{dc} with time, but the hysteresis when decreasing H_{dc} with time was similar to that shown at T=77 K. Figure 3 shows that at some values of α below T=140 K there are two absorption maxima at a given temperature. Figure 8 refers only to the lower field maximum.

It is interesting to compare Figures 7 and 8 at temperatures such as 153 K and 77 K. The comparison at T=153 K gives strong indication of off-resonance absorption because the field values in Figure 8 do not change much with ϕ, while the amplitude in Figure 7 changes rapidly. The amplitude at T=77 K in Figure 7 tends to disappear when the field values in Figure 8 approach the domain alignment field indicated by the open triangles in Figure 4. In this experiment the a-axis was taken as the symmetry axis in Figure 8, and this symmetry axis was always within a few degrees of the a-axis direction determined by X-rays, which direction we preserved as well as possible on the spectrometer by careful mounting. Errors contributing to a slight misalignment of the sample were 1. difficulty in placing a scratch on the sample corresponding exactly to a crystallographic axis determined by Laue X-ray diffraction, and 2. the

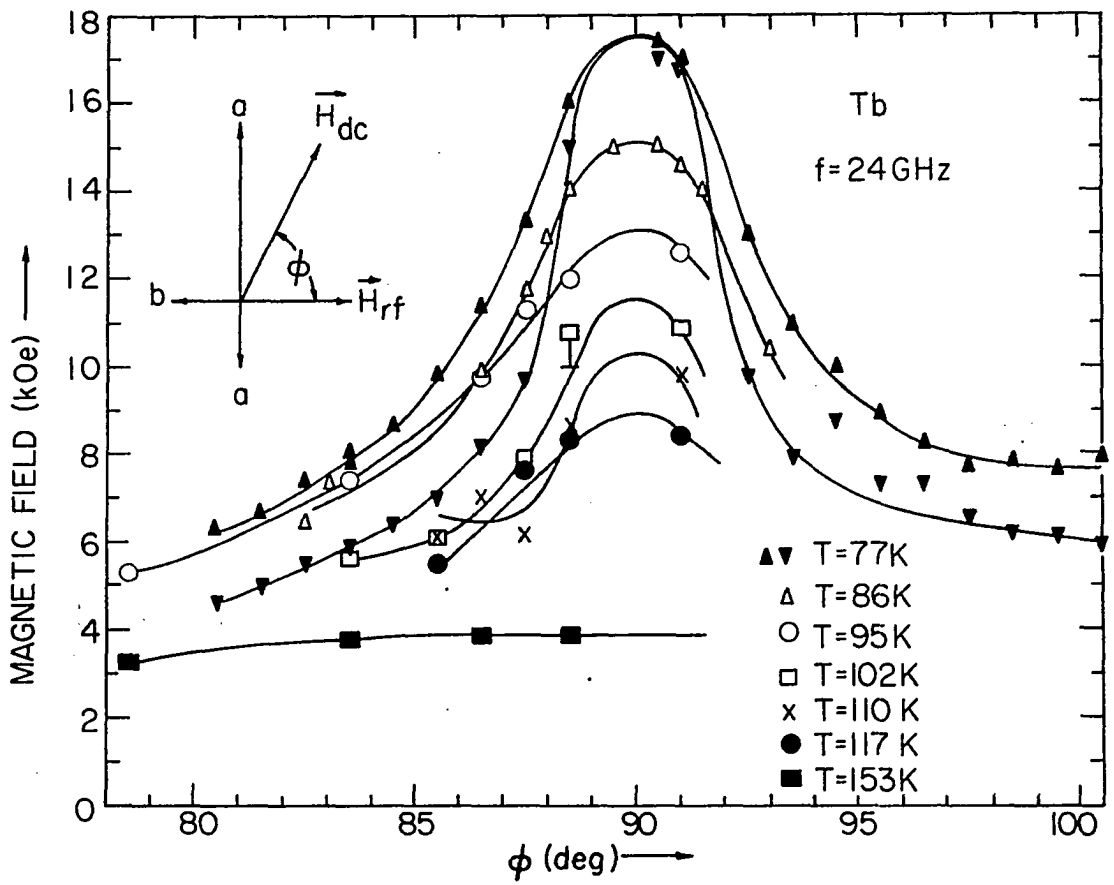

Figure 8. Plot of the field values of power absorption maxima as a function of the angle between H_{rf} and H_{dc} for Tb.

difficulty of aligning the scratch on the sample precisely with a known magnet angle marked on the cavity.

F. Discussion

If we now assume that the magnetic field necessary for on-resonance absorption in the q=0 mode at our low experimental frequency is approximately the same as the magnetic field necessary for $\hbar\omega=0$ in Equation 1, we obtain (assuming $N_y=N_z$),

$$H_{dc}\cos(\beta-\theta) = -18c^{\gamma}A(0)C(0)\cos 6\theta\, I_{9/2}I_{5/2}M^{-1} . \tag{9}$$

Unfortunately, however, the additional condition imposed by Equation 2 says that for $\hbar\omega=0$, $\beta=\theta=30^{\circ}$ is the only allowed value of β and θ, so that Equation 9 becomes

$$H_{dc} = 18c^{\gamma}A(0)C(0)I_{9/2}I_{5/2}M^{-1} \tag{10}$$

which is the spin-flip field. This means that $\hbar\omega=0$ (corresponding to on-resonance absorption) only when H_{dc} is at the spin-flip field along a hard $\langle 11\bar{2}0\rangle$ direction as shown in Figure 5. From Figure 7 we see that at $\phi=90^{\circ}$ (corresponding to $\beta=\theta=30^{\circ}$) there is no resonance at T=77 K at the spin-flip field as predicted. In fact, the magnetic field has to be aligned about 1° away from the a-axis before a resonance occurs essentially at the spin-flip field (see Figure 4). We have a case where the theory predicts a resonance where experimentally one is not found, and predicts no resonance where many are found. However, for small angular

deviations of $\vec{H}_{dc}$ from the a-axis, the experimental results are almost the same as those predicted for H_{dc} exactly along the a-axis. Perhaps one might suspect some error in the assumption that letting $\hbar\omega=0$ in Equation 1 to obtain Equation 9 gives us the equivalent of on-resonance absorption at our experimental frequency. Vigren and Liu [(20)], however, solved Equations 1 and 2 simultaneously by computer techniques for our experimental frequency (thus avoiding the $\hbar\omega=0$ approximation). They found that on-resonance absorption was possible for all practical purposes only at $\beta=30^{\circ}$. Even assuming off-resonance absorption to be possible for $\beta<30^{\circ}$, Vigren and Liu showed that the predictions of Equations 1 and 2 do not even qualitatively explain the data plotted in Figure 8. (The discrepancy between theory and experiment becomes more pronounced the farther the magnetic field is mis-aligned from the a-axis.) The exact solution of Equations 1 and 2 made by Vigren and Liu at 24 GHz essentially confirms our simple theoretical results obtained by assuming that the on-resonance absorption condition at 24 GHz is equivalent to setting $\hbar\omega=0$ in Equation 1.

One possible explanation of this discrepancy between theory and experiment in our rotation results is that Equation 2 is incorrect. Clearly either Equations 1 or 2 or both are incorrect, but Equation 1 does do a good job of explaining the data in Figure 4 where the line labeled A is essentially a plot of the spin-flip field given by Equation 10 as a function of temperature. For Equation 1 to be correct the original Hamiltonian has to be correct only up to terms of second order in the Holstein-Primakoff spin deviation operators, but Equation 2 might

conceivably depend significantly on terms which are not included in the original Hamiltonian. In any case it is possible to present a consistent interpretation of the data by graphically finding a transcendental equation to replace Equation 2 which when combined with Equation 1 will explain the experimental facts. Figure 9 is an attempt to do this. The assumption is made that our experimental results are due to on-resonance absorption because of their large amplitudes. Our experimental results therefore have essentially the field dependence given by Equation 9 where we make the approximation $\cos(\beta-\theta)=1$. We can make this approximation because $\theta \geq 15^{\circ}$ for $H_{dc} \geq 0$ in Equation 9, and $30^{\circ} \geq \beta \geq 0$ from physical and energy considerations, so combining these two results gives us $0 \leq \beta-\theta \leq 15^{\circ}$ or $0.97 \leq \cos(\beta-\theta) \leq 1$. We see that Equation 9 has essentially no β dependence. Equation 9 is plotted in Figure 9 as line C. The point A represents the spin-flip field given by Equation 10, and the line B is a plot of Equation 2 when $\beta=30^{\circ}$. For other values of β, Equation 2 no longer intersects line C in Figure 9, so on-resonance absorption is not possible as previously stated. The lines labeled D in Figure 9 are schematic transcendental equations replacing Equation 2 for different values of β, which intersect line B at the field values necessary to explain our data as on-resonance absorption at T=77 K. If Equation 1 is in fact correct, the lines labeled D are experimental determinations of the transcendental equation at the points where data is plotted. An independent experimental determination of the transcendental equation could be done in principle by elastic neutron scattering with an external field in different directions in the basal plane of the

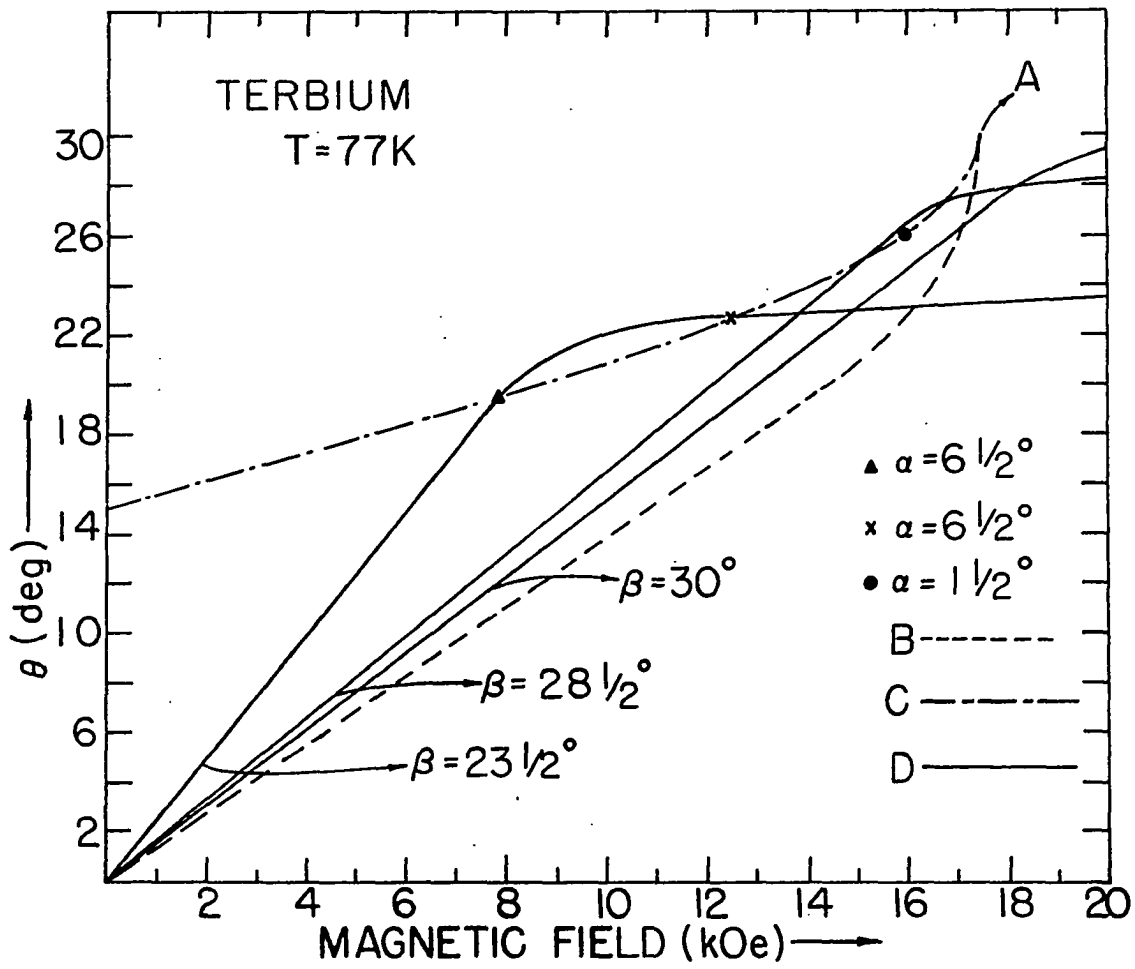

Figure 9. Plot of θ as defined in Equation 11 (the angle between $\vec{M}$ and the nearest b-axis) as a function of magnetic field in various mathematical expressions and schematic suggestions described in the text.

sample, or by a careful analysis of magnetization data obtained in a similar manner. An experimentally determined transcendental equation could be compared to the lines labeled D in Figure 9 to check our assumption that Equation 2 is incorrect.

The α values given for the plotted data in Figure 9 are to facilitate comparison with Figure 3 (only data for H_{dc} increasing with time are plotted). To avoid confusion, note that α, ϕ, and β each measure the angle between $\vec{H}_{dc}$ and a different reference axis. Both absorption maxima at T=77 K, $\alpha=6\frac{1}{2}^{o}$ in Figure 3 are explained by the $\beta=23\frac{1}{2}^{o}$ schematic transcendental equation in Figure 9. In fact, the assumption that Equation 9 (represented by line C) correctly explains our data <u>requires</u> a double resonance such as is possibly observed. This is strong additional evidence that Equation 1 is essentially correct as we initially assumed. The $\beta=28\frac{1}{2}^{o}$ curve in Figure 9 represents a possible explanation for the T=77 K, $\alpha=1\frac{1}{2}^{o}$ data in Figure 3 by assuming the peak to be the sum of two overlapping, unresolved peaks. Hence by comparison with the T=77 K, $\alpha=6\frac{1}{2}^{o}$ data, the $\alpha=1\frac{1}{2}^{o}$ data shows an increase in amplitude and a larger linewidth than the low field resonance at $\alpha=6\frac{1}{2}^{o}$. (The very large linewidth of the higher field resonance at $\alpha=6\frac{1}{2}^{o}$ is not understood, but the linewidth of the low field resonance corresponds almost exactly to detailed linewidth calculations by Vigren and Liu for T=100 K in Figure 6.) Since no resonance is observed at $\phi=90^{o}$, T=77 K in Figure 7, the $\beta=30^{o}$ curve in Figure 9 represents a possible explanation (the $\beta=30^{o}$ curve is a schematic replacement for curve B representing Equation 2).

Figure 9 can also be used to explain the data at temperatures other

than 77 K if the abscissa is scaled so that point A has its magnetic field coordinate given by Equation 10. At T=95 K and 110 K in Figure 3 we present more data showing the behavior of two absorption maxima very similar to the two maxima discussed in Figure 9 at T=77 K, $\alpha=6\frac{1}{2}^{o}$. Note that at T=110 K both maxima are resolved for a low α value ($\alpha=1\frac{1}{2}^{o}$), whereas they are not resolved at $\alpha=1\frac{1}{2}^{o}$ for lower temperatures.

For temperatures above 140 K, point A in Figure 9 falls below the domain alignment field, hence all absorption is off-resonance. The rotation amplitude results in Figure 7 for temperatures above 140 K can be qualitatively explained by noting that the farther the magnetic field gets aligned from the a-axis the farther off-resonance the absorption becomes, so the smaller the amplitude becomes. In the temperature region above 140 K the amplitude will be most affected by rotation of H_{dc} for temperatures slightly above 140 K because then point A in Figure 9 is just below the domain alignment field. The amplitude will be least affected by rotation of H_{dc} near the Néel temperature because then point A in Figure 9 is at $H_{dc}=0$ and there is no longer any hexagonal anisotropy. At T=220 K (near the Néel temperature) the off-resonance absorption has a nearly $\sin^2\phi$ dependence as expected (see Figure 7).

G. Conclusions

In conclusion, our results at 24 GHz experimentally confirm free lattice model behavior in Tb at low microwave frequencies where the q=0 state can be excited as predicted by Vigren and Liu (10) (see Figure 4), furnishing a satisfying resolution to the previously paradoxical ferromagnetic resonance data on Tb. Our explanation of the rotation studies

using Figure 9 assumed the experimental results were due to on-resonance absorption because of their large amplitude. The on-resonance absorption condition at our low experimental frequency (24 GHz) was assumed to be essentially the same as the condition $\hbar\omega=0$ in Equation 1 by analogy to the case where H_{dc} is in the hard $\langle 11\bar{2}0\rangle$ direction depicted in Figure 5. The foregoing assumptions meant that the transcendental Equation 2 had to be considered incorrect, so in Figure 9 we graphically constructed transcendental equations that were consistent with the experimental data and the assumption $\hbar\omega=0$ in Equation 1 for on-resonance absorption. (If both Equations 1 and 2 are considered correct the theory does not even qualitatively explain our experimental results.) As an unexpected bonus, our theoretical assumptions predicted that a double resonance should be present in our rotation studies, which was possibly observed. The linewidths and amplitudes of our experimental peaks were at least partially explained by comparing the linewidth calculations of Vigren and Liu to our resolved double peaks and by assuming that our single peaks were really two unresolved peaks. We thus have good internal consistency between our theoretical assumptions and our experimental results. In fact, all of our experimental results can be qualitatively explained by using the graphical transcendental equations in Figure 9. An independent check on the correctness of our graphical transcendental equations in Figure 9 and hence of all our theoretical assumptions could be made in principle by an elastic neutron scattering and/or a magnetization experiment where H_{dc} was rotated to various angles in the basal plane of the sample.

A further experimental argument in favor of the correctness of Equation 1 is that it correctly explains the field and temperature dependence of the resonance when H_{dc} is aligned within a few degrees of the a-axis (see Figure 4). From a theoretical point of view, spin wave theory employs the harmonic oscillator approximation, which means that the original Hamiltonian needs to be correct only to second order in the Holstein-Primakoff spin deviation operators for Equation 1 to be correct, whereas Equation 2 might well depend on terms which are not included in the present Hamiltonian.

III. $MnAu_2$

A. Introduction

$MnAu_2$ is an intermetallic compound with unusual magnetic properties. The ordered metallic phase $MnAu_2$ was detected by Raub et al. (35) below a temperature of 730°C. Above this temperature a eutectic is formed which melts at 1000°C. The ordered phase of $MnAu_2$ has a body centered tetragonal unit cell (36) with the Mn atoms providing the magnetic properties of the system (37). It is presumed that in the ordered state we have the Au^+ ion in the configuration $5d^{10}$ and spectroscopic designation $^1S_0$, and the Mn^{++} ion in the configuration $3d^5$ and spectroscopic designation $^6S_{5/2}$. The Landé factor for a free Mn^{++} ion is then g=2.

The magnetic properties of polycrystalline $MnAu_2$ were first investigated by Meyer and Taglang (38). They found that $MnAu_2$ was antiferromagnetic below 363 K and paramagnetic above 363 K in zero applied field. In the antiferromagnetic state, a field of about ~~10 k~~Oe caused a magnetic transition to a state with a ferromagnetic component. A saturation magnetic moment of 3.49 μ_B per atom of manganese was found at low temperatures, where μ_B is the Bohr magneton.

The nature of the antiferromagnetic state of $MnAu_2$ was determined by Herpin and Meriel (37) using neutron diffraction techniques. They discovered the antiferromagnetism was due to a spiral ordering of the spins in the plane perpendicular to the c-axis (⟨001⟩ direction) with a turn angle of 51° between successive layers (all the spins in a given layer perpendicular to the c-axis are ferromagnetically aligned). When

a field of about 10 kOe was applied perpendicular to the c-axis, a transition from the spiral structure to a fan structure predicted by Nagamiya et al. (39, 40) was observed. Pure ferromagnetic alignment occurred for applied fields less than 20 kOe.

The excited states of the spin system in $MnAu_2$ were investigated by Asch (41) at a frequency of 35.6 GHz. He observed apparent resonance absorption in the spiral phase of polycrystalline $MnAu_2$ at a temperature of 173 K. Since the theory of spin wave resonance in the magnetic spiral phase of a metal developed by Cooper et al. (9, 42) has difficulty explaining the resonance observed by Asch, we decided to perform experiments in the frequency range 20-26 GHz to obtain more data, hoping to clarify the situation.

B. Theory

Following the treatment found in Reference (9), the spin wave spectrum of a planar spiral spin system will be derived with no applied magnetic field. We start with the Hamiltonian

$$\mathcal{H} = -\sum_{i \neq j} J_{ij} \vec{S}_i \cdot \vec{S}_j - K_2 \sum_i S_{i\zeta}^2 \qquad (11)$$

where J_{ij} is the isotropic exchange coefficient and K_2 is the negative two-fold anisotropy constant. The sums are over all the spins in a crystal with periodic boundary conditions and $\hat{\zeta}$ is along the c-axis. We will take the Fourier transform of Equation 11, so we define

$$J(q) = \sum_j J_{ij} \cos \vec{q}\cdot(\vec{R}_i - \vec{R}_j) \quad . \tag{12}$$

Using Equation 11 in the molecular field approximation, the ground state of the spiral spin system is given by

$$E/N = -S^2 J(k_o) \quad . \tag{13}$$

Here $\vec{k}_o$ is directed along the c-axis and has a magnitude determined by $k_o c' = \theta$ where c' is the distance along the c-axis between adjacent atomic planes, and θ is the spin turn angle between adjacent planes. From the form of Equation 13 it is obvious that $J(k_o)$ must be a maximum for the spiral spin structure to be stable in the ground state.

We now transform to new coordinates such that the equilibrium direction of the spin at each site determines the z direction at that site.

$$S_{i\zeta} = -S_{ix}$$

$$S_{i\eta} = S_{iy} \cos \vec{k}_o\cdot\vec{R}_i + S_{iz} \sin \vec{k}_o\cdot\vec{R}_i \tag{14}$$

$$S_{i\xi} = -S_{iy} \sin \vec{k}_o\cdot\vec{R}_i + S_{iz} \cos \vec{k}_o\cdot\vec{R}_i \quad .$$

The directions $\hat{\eta}$ and $\hat{\xi}$ are fixed to the crystal and are mutually

perpendicular in the basal plane such that $(\hat{\xi},\hat{\eta},\hat{\zeta})$ form a right handed coordinate system. The $\hat{z}$ direction is always in the basal plane, and $\hat{y}$ is perpendicular to $\hat{z}$ in the basal plane such that $(\hat{x},\hat{y},\hat{z})$ forms a right handed coordinate system with $\hat{x}=-\hat{\zeta}$.

The Hamiltonian is further transformed by the substitution

$$S_{ix} = \frac{1}{2}\,(S_i^+ + S_i^-)$$

$$S_{iy} = \frac{1}{2i}\,(S_i^+ - S_i^-) \tag{15}$$

which allows us to make the Holstein-Primakoff (23) approximation

$$S_i^+ = (2S)^{\frac{1}{2}} a_i$$

$$S_i^- = (2S)^{\frac{1}{2}} a_i^\dagger \tag{16}$$

$$S_{iz} = S - a_i^\dagger a_i \quad .$$

The above approximation assumes that spin waves are small deviations from the equilibrium spin direction, which can be better realized the larger the value of S. The spin deviation operators are Fourier transformed as follows

$$a_i = N^{-\frac{1}{2}} \sum_q a_q\, e^{-i\vec{q}\cdot\vec{R}_i}$$

$$a_q = N^{-\frac{1}{2}} \sum_i a_i\, e^{i\vec{q}\cdot\vec{R}_i} \tag{17}$$

where q is summed over the first Brillouin zone in reciprocal space of the atomic lattice and the states in the first zone are counted using periodic boundary conditions, a convention used hereafter for sums on q. The Hamiltonian finally becomes

$$\mathcal{H} = E_o + \sum_q [2SA_q a_q^\dagger a_q + SB_q (a_q^\dagger a_{-q}^\dagger + a_q a_{-q})] \tag{18}$$

where

$$\begin{aligned} E_o &= -NS^2 J(k_o) - \tfrac{1}{2} NSK_2 \\ A_q &= -\tfrac{1}{4}[2J(q) - 4J(k_o) + 2K_2 + J(k_o+q) + J(k_o-q)] \\ B_q &= -\tfrac{1}{4}[2J(q) + 2K_2 - J(k_o+q) - J(K_o-q)] \end{aligned} \tag{19}$$

and for convenience the notation $J(k_o \pm q)$ which means $J(k_o \pm q) = J(\vec{k}_o \pm \vec{q})$ is used, a notation adopted hereafter. A Bogoluibov transformation is now performed in order to diagonalize Equation 18. Let

$$\alpha_q = w_q a_q + b_q a_{-q}^\dagger \, . \tag{20}$$

The relation

$$[\alpha_q, \mathcal{H}] = \hbar\omega(q)\alpha_q \tag{21}$$

must be satisfied where $\hbar\omega(q)$ is the desired spin wave energy. For linearly independent coefficients w_q and b_q, Equation 21 can only be satisfied for

$$\hbar\omega(q) = 2S[(A_q+B_q)(A_q-B_q)]^{\frac{1}{2}} \tag{22}$$

where A_q and B_q are defined in Equation 19.

Equation 18 can now be put in diagonal form. The parameters w_q and b_q can be solved in terms of A_q, B_q, and $\hbar\omega(q)$ using Equation 21 and the condition

$$w_q^2 - b_q^2 = 1 \ . \tag{23}$$

Equation 23 is imposed so that α_q will have the commutation relations of a true boson operator (spin waves are bosons). Using the Fourier transform Equation 12 and its inverse with the condition $J_{ii}=0$ we obtain

$$\sum_q J(q) = \sum_q J(k_o \pm q) = 0 \tag{24}$$

which further simplifies Equation 18 to the diagonal form

$$\mathcal{H} = -NJ(k_o)S(S+1) + \sum_q \hbar\omega(q)(\alpha_q^\dagger \alpha_q + \tfrac{1}{2}) \ . \tag{25}$$

The zero point energy of the system is

$$E/N = -S(S+1)J(k_o) + (2N)^{-1}\sum_q \hbar\omega(q) \ . \tag{26}$$

The second term in Equation 26 is due to zero point spin waves and is small compared to the first term. If Equation 13 and Equation 26 are

compared, it is seen that the molecular field approximation given by Equation 13 does not give the correct ground state energy of the system. In fact, the percent error in Equation 13 when compared with the first term in Equation 26 for $MnAu_2$ is given by

$$(S+1)^{-1}(100) \cong 30\% \ . \tag{27}$$

Equation 13 should be decreased in energy by about 40% in order to be correct for $MnAu_2$. This is a sizeable error and shows the dangers inherent in using the molecular field approximation. In fact, the Holstein-Primakoff harmonic oscillator approximation used in obtaining $\hbar\omega(q)$ (Equation 22) may not be valid for $MnAu_2$ because of its small spin. It is evident that the error is smaller the larger the value of spin, so the error is smaller for the heavy rare earths if the molecular field approximation for the ground state energy is used.

If a linearly polarized microwave-frequency magnetic field is now applied parallel to the surface of a sample at an angle ϕ to the c-axis ($\hat{\zeta}$ direction), the resulting Zeeman energy is considered a small perturbation on the spin system. The "golden rule" is used to calculate the transition rate to excited spin wave states, giving an idea of the intensity of signals expected in a spin wave resonance experiment where the frequency is swept. Without considering the effects of the metal skin depth specifically, it is found that the intensity of spin waves of wavenumber q is proportional to the square of the coefficients of the $\alpha_q^\dagger$ terms in the expression for the Zeeman energy. The intensity of spin

waves of wavenumbers excited by an rf magnetic field parallel to the sample surface at an angle ϕ to the c-axis is therefore

$$I(\pm k_o) \propto (w_{k_o} + b_{k_o})^2 \sin^2\phi$$
$$I(0) \propto (w_0 - b_0)^2 \cos^2\phi. \tag{28}$$

Equation 28 gives the square of the coefficients multiplied by $\alpha^\dagger_{k_o}$, $\alpha^\dagger_{-k_o}$, and $\alpha^\dagger_0$ in the expression for the Zeeman energy. In order to evaluate Equation 28 we use Equation 21 and Equation 23 to obtain

$$(w_q + b_q)^2 = \left[\frac{A_q + B_q}{A_q - B_q}\right]^{\frac{1}{2}} = \frac{-2K_2S + 2S[J(k_o) - J(q)]}{\hbar\omega(q)}$$
$$(w_q - b_q)^2 = \left[\frac{A_q - B_q}{A_q + B_q}\right]^{\frac{1}{2}} \tag{29}$$

From Equation 19 we note that $A_0 = B_0$, so $I(0)=0$ and $\hbar\omega(0)$ cannot be excited by microwaves. From Equation 22 we see that $\hbar\omega(0)=0$ and

$$\hbar\omega(\pm k_o) = [-2K_2(a_0 + a_2)]^{\frac{1}{2}} \tag{30}$$

where

$$a_0 = S^2[J(k_o) - J(0)]$$
$$a_2 = S^2[J(k_o) - J(2k_o)] \tag{31}$$

From Equation 28 we see that microwaves of energy given by Equation 30 polarized perpendicular to the c-axis are excited with an intensity proportional to the first expression in Equation 29 with $q=k_o$. This intensity is considered to be typical of ferromagnetic resonance because it is finite and ferromagnetic resonance (given by $k_o=0$) is just a special case.

As is seen later, Equation 30 corresponds to an energy generally above available microwave frequencies, so it will be interesting to see if an applied magnetic field can lower the energy gap of the spin wave of wavenumber k_o. The easiest mathematical configuration is to apply a magnetic field parallel to the c-axis ($\hat{\zeta}$ direction) of the crystal. The spiral configuration becomes a cone where the spin wave energies excited by an rf magnetic field perpendicular to the axis become (9, 42)

$$\hbar\omega(\pm k_o) = \pm \frac{(a_0-a_2)\cos\psi}{S} + \sin\psi[-2K_2(a_0+a_2)]^{\frac{1}{2}} \times \left[1 + \frac{(a_0+a_2)\cos^2\psi}{-2K_2S^2\sin^2\psi}\right]^{\frac{1}{2}} \tag{32}$$

where

$$\cos\psi = \frac{H}{H_o} \quad \text{and} \quad H_o = \frac{-2K_2S}{g\mu_B} + \frac{2a_0}{g\mu_B S} \quad . \tag{33}$$

ψ is the semi-vertical angle of the cone generated by the magnetic moments. When H=0 (no applied magnetic field), then Equation 32 reduces to Equation 30. When $H \geq H_o$, there is pure ferromagnetic alignment along $\hat{\zeta}$ and the resonance expression becomes (9)

$$\hbar\omega(k_o) = g\mu_B H + 2K_2S \quad . \tag{34}$$

An rf field parallel to the $\hat{\zeta}$ direction of the cone excites only $\hbar\omega(0)=0$ with zero intensity exactly as in the planar spiral case. For the spin wave energies given by Equations 32 and 34 excited by an rf field perpendicular to the c-axis, the intensity of excitation is typical of ferromagnetic resonance except for $\hbar\omega(-k_o)$, which has its intensity go to zero as H approaches H_o. When $H=H_o$, Equation 32 becomes

$$\hbar\omega(+k_o) = \frac{2a_0}{S}$$
$$\hbar\omega(-k_o) = \frac{2a_2}{S} \quad . \tag{35}$$

Since $a_0<a_2$ as we shall see later (42), the first expression in Equation 35 gives the smallest energy gap possible in an applied field for the cone configuration.

We now wish to apply a magnetic field perpendicular to the c-axis in the basal plane of the spiral and derive the consequences to the spin wave spectrum following Reference (42). First, a Zeeman term given by $-g\mu_B H\sum_i S_i$ is added to Equation 11 where $\vec{H}\|-\hat{\zeta}$ in the basal plane of the spiral. According to Nagamiya et al. (39, 40), if a magnetic field is applied in the basal plane of a spiral, the spin configuration remains a distorted spiral until a field

$$H_c = \frac{a_0}{g\mu_B S} \tag{36}$$

is reached where a first order transition to a "fan" structure occurs.

The fan has a strong ferromagnetic component and closes continuously to a pure ferromagnetic state at a field given approximately by

$$H_f = \frac{2a_0}{g\mu_B S} \quad . \tag{37}$$

Equation 36 allows us to make an estimate of the parameter a_0 because H_c can be measured by many methods.

For $H<H_c$, Equation 14 must be altered by replacing $\vec{k}_o \cdot \vec{R}_i$ by an arbitrary angle ϕ_i when a magnetic field is applied in the basal plane of the spiral. The angle ϕ_i is determined by solving the equation

$$\frac{\partial \mathcal{H}_o}{\partial \phi_i} = 0 = 2S\sum_j J_{ij}\sin(\phi_i - \phi_j) + g\mu_B H \sin\phi_i \quad . \tag{38}$$

$\mathcal{H}_o$ is the Hamiltonian in the molecular field approximation. Equation 38 is solved by iteration for small values of magnetic field by making an expansion in powers of the magnetic field

$$\phi_i = \vec{k}_o \cdot \vec{R}_i + \delta\phi_i^{(1)} + \delta\phi_i^{(2)} + \ldots \quad . \tag{39}$$

The superscript in the perturbational terms refers to the power of magnetic field retained in that term. Substituting $\phi_i = \vec{k}_o \cdot \vec{R}_i$ in the last term of Equation 38 (the perturbing term), and substituting $\phi_i = k_o \cdot R_i + \delta\phi_i^{(1)}$ into the first term, we can solve for $\delta\phi_i^{(1)}$ to first order in magnetic field by first expanding $\delta\phi_i^{(1)}$ in a Fourier series and then solving Equation 38 separately for each of the linearly independent coefficients. The expansion is

$$\delta\phi_i^{(1)} = \sum_n \delta\phi_n^{(1)} e^{-in\vec{k}_o\cdot\vec{R}_i} \quad , \quad n=0,\ 1,\ 2,\ \ldots \qquad (40)$$

After solving for $\delta\phi_i^{(1)}$, we continue the iteration by substituting $\phi_i = k_o\cdot R_i + \delta\phi_i^{(1)}$ into the last term of Equation 38, and substituting the terms shown explicitly in Equation 39 into the first term of Equation 38, and solving for $\delta\phi_1^{(2)}$ to second-order in magnetic field by expanding it as in Equation 40. The result after many iterations becomes (to sixth-order in magnetic field)

$$\begin{aligned}\phi_i = {} & \vec{k}_o\cdot\vec{R}_i + (A_1+C_1+E_1)\sin\vec{k}_o\cdot\vec{R}_i + (B_2+D_2+F_2)\sin 2\vec{k}_o\cdot\vec{R}_i \\ & + (C_3+E_3)\sin 3\vec{k}_o\cdot\vec{R}_i + (D_4+F_4)\sin 4\vec{k}_o\cdot\vec{R}_i \\ & + E_5\sin 5\vec{k}_o\cdot\vec{R}_i + F_6\sin 6\vec{k}_o\cdot\vec{R}_i\end{aligned} \qquad (41)$$

where $\mu=g\mu_B S$ and the coefficients determined by iteration are

$$\begin{aligned}A_1 &= \frac{-\mu H}{a_0+a_2} \\ B_2 &= \frac{-\mu H A_1}{2a_3} \\ C_1 &= \frac{\mu H}{a_0+a_2}\left(\frac{3A_1^2}{8} - \frac{B_2}{2}\right) \\ C_3 &= \frac{-\mu H}{a_2+a_4}\left(\frac{A_1^2}{8} + \frac{B_2}{2}\right)\end{aligned} \qquad (42)$$

$$D_2 = \frac{\mu H}{a_3}\left(\frac{A_1^2}{24} + \frac{A_1B_2}{2} - \frac{C_1}{2} - \frac{C_3}{2}\right)$$

$$D_4 = \frac{-\mu H}{a_3+a_5}\left(\frac{A_1^3}{48} + \frac{A_1B_2}{4} + \frac{C_3}{2}\right)$$

$$E_1 = \frac{\mu H}{a_o+a_2}\left(\frac{-5A_1^4}{192} + \frac{A_1^2B_2}{8} + \frac{B_2^2}{4} + \frac{3A_1C_1}{4} - \frac{A_1C_3}{4} - \frac{D_2}{2}\right)$$

$$E_3 = \frac{\mu H}{a_2+a_4}\left(\frac{5A_1^4}{384} + \frac{A_1^2B_2}{16} + \frac{B_2^2}{8} - \frac{A_1C_1}{4} + \frac{A_1C_3}{2} - \frac{D_2}{2} - \frac{D_4}{2}\right)$$

$$E_5 = \frac{-\mu H}{a_4+a_6}\left(\frac{A_1^4}{384} + \frac{A_1^2B_2}{16} + \frac{B_2^2}{8} + \frac{A_1C_3}{4} + \frac{D_4}{2}\right)$$

$$F_2 = \frac{\mu H}{a_3}\left(\frac{-5A_1^5}{3840} - \frac{5A_1^3B_2}{96} + \frac{3A_1B_2^2}{16} + \frac{A_1^2C_1}{8} + \frac{A_1^2C_3}{16} + \frac{B_2C_1}{2} + \frac{B_2C_3}{4} + \frac{A_1D_2}{2} - \frac{A_1D_4}{4} - \frac{E_1}{2} - \frac{E_3}{2}\right)$$

$$F_4 = \frac{\mu H}{a_3+a_5}\left(\frac{A_1^5}{960} + \frac{A_1^3B_2}{24} - \frac{A_1^2C_1}{16} + \frac{A_1^2C_3}{16} - \frac{B_2C_1}{4} + \frac{B_2C_3}{4} - \frac{A_1D_2}{4} + \frac{A_1D_4}{2} - \frac{E_3}{2} - \frac{E_5}{2}\right)$$

$$F_6 = \frac{-\mu H}{a_5+a_7}\left(\frac{A_1^5}{3840} + \frac{A_1^3B_2}{96} - \frac{A_1B_2^2}{16} - \frac{A_1^2C_3}{16} - \frac{B_2C_3}{4} - \frac{A_1D_4}{4} - \frac{E_5}{2}\right).$$

We define

$$a_n = S^2[J(k_o) - J(nk_o)], \quad n=0, 1, 2, \ldots \tag{43}$$

so that $a_1=0$, and a_0, a_2 are defined the same as in Equation 31. Methods of estimating the parameters in Equation 43 will be discussed later.

The Hamiltonian (including the Zeeman term) can now be written correct to the terms necessary in the harmonic oscillator approximation:

$$\mathcal{H} = -\sum_{i\neq j} J_{ij}\{(S_{iy}S_{jy}+S_{iz}S_{jz})\cos(\phi_i-\phi_j) + S_{ix}S_{jx}\}$$
$$-K_2\sum_i S_{ix}^2 - g\mu_B H\sum_i S_{iz}\cos\phi_i \qquad (44)$$

where ϕ_i is given by Equations 41 and 42 and the coordinate system is the same as that defined for Equation 14. The equations of motion method is used to find the energy of the spin wave states of the system

$$[S_x(\vec{q}),\mathcal{H}] = i\hbar\dot{S}_x(\vec{q}) = -\hbar\omega S_x(\vec{q}) \qquad (45)$$

where

$$S_x(\vec{q}) = N^{-\frac{1}{2}}\sum_i S_{ix}e^{i\vec{q}\cdot\vec{R}_i}$$
$$S_{ix} = N^{-\frac{1}{2}}\sum_q S_x(\vec{q})e^{-i\vec{q}\cdot\vec{R}_i} \qquad (46)$$

and a similar equation of motion for $S_y(\vec{q})$ is obtained by interchanging x and y in Equations 45 and 46. Terms only up to second order in magnetic field are kept in Equation 44 for simplicity, so using

the ordinary spin commutation relations for S_{ix} and S_{iy} in Equation 45 we obtain

$$\begin{aligned} -\hbar\omega(q)S_x(\vec{q}) &= \sum_{-2\le r\le 2} iD_r(q)S_y(\vec{q}+r\vec{k}_o) \\ -\hbar\omega(q)S_y(\vec{q}) &= \sum_{-2\le r\le 2} iG_r(q)S_x(\vec{q}+r\vec{k}_o) \end{aligned} \tag{47}$$

where to second-order in magnetic field

$$\begin{aligned} D_0(q) &= S[2J(k_o) - J(k_o+q) - J(k_o-q)] \\ &\quad + \frac{A_1^2 S}{8}[4J(0) - 8J(k_o) + 4J(2k_o) - 4J(q) + 4J(q+k_o) \\ &\quad + 4J(q-k_o) - 2J(q+2k_o) - 2J(q-2k_o)] - \frac{g\mu_B H A_1}{2} \end{aligned} \tag{48}$$

$$\begin{aligned} D_{-1}(q) &= \frac{-A_1 S}{2}[J(q+k_o) - J(q-k_o) + J(q-2k_o) - J(q) + J(0) \\ &\quad - J(2k_o)] + \frac{g\mu_B H}{2} \end{aligned}$$

$$D_1(q) = D_{-1}(-q)$$

$$D_{-2}(q) = \frac{B_2 S}{2}\left[2J(q-k_o) - J(q+k_o) - J(q-3k_o) + J(3k_o) - J(k_o)\right]$$
$$+ \frac{A_1^2 S}{8}\left[2J(q) + 2J(q-2k_o) - 2J(q-k_o) - J(q+k_o) - J(q-3k_o)\right.$$
$$\left. + 3J(k_o) + J(3k_o) - 2J(0) - 2J(2k_o)\right] + \frac{g\mu_B H A_1}{4}$$

$$D_2(q) = D_{-2}(-q)$$

$$G_o(q) = S[2K_2 - 2J(k_o) + 2J(q)]$$

$$G_{\pm 1}(q) = \frac{A_1 S}{2}[J(0) - J(2k_o)] - \frac{g\mu_B H}{2}$$

$$G_{\pm 2}(q) = \frac{B_2 S}{2}[J(k_o) - J(3k_o)] + \frac{A_1^2 S}{8}[2J(0) + 2J(2k_o)$$
$$- 3J(k_o) - J(3k_o)] - \frac{g\mu_B H A_1}{4} \quad .$$

Equation 47 can now be solved for $\hbar\omega(q)$ where $q=0$, k_o, $2k_o$, etc. by making some approximations. We note that if $q=0$ in Equation 47, there are terms such as $S_y(\pm k_o)$ and $S_y(\pm 2k_o)$ that are coupled to $S_x(0)$, and each of the terms $S_y(\pm k_o)$ and $S_y(\pm 2k_o)$ are coupled to terms of even higher multiples of k_o. We would like to keep as many terms as practicable, and it is possible to keep terms up to $S_x(\pm 3k_o)$ in solving for $\hbar\omega(0)$ and still have to solve only a 4X4 determinant for the normal

frequencies of the system of spins. The order of the determinant necessary to solve Equation 47 for q=0, $\pm k_o$, $\pm 2k_o$, $\pm 3k_o$ is reduced by a factor of two by combining the two equations in Equation 47 so that the y subscript is eliminated. The order of the determinant is reduced by another factor of two (making it 4X4) by noting that the operators can be combined into symmetric combinations such as $[S_x(k_o) + S_x(-k_o)]$, $[S_x(2k_o) + S_x(-2k_o)]$, etc. In order to solve the 4X4 determinant for $\hbar\omega(0)$ to first-order in H (which is the highest order we can solve for with the Hamiltonian to second-order in H), we expand $\omega(0)\equiv\omega$ as

$$\omega = \omega_o + \omega_1 H \tag{49}$$

where ω_o=0 for q=0. We retain only the lowest order terms in H (H^2) when expanding the determinant and obtain ω_1=0. This means that $\omega(0)$=0 to first order in H, at least to the approximation used in ignoring terms of $q=\pm 4k_o$ and higher. By analogy, however, it is easy to see from the form of the determinant that even if the determinant were of infinite order (by allowing coupling to all possible multiples of k_o) the result would still be the same to order H^1:

$$[\hbar\omega(0)]^2 = \frac{-\mu H}{S^2}(a_0 - K_2 S^2)[A_1 + \mu H/(a_0 + a_2)] = 0 \ . \tag{50}$$

See Equation 42 for the value of A_1 in Equation 50. By making the simplifying assumption that the K_2 term is much larger than the other terms (as it is in the heavy rare earths), Cooper and Elliott (42)

were able to solve for $\omega(0)$ to order H^2. They got a non-zero answer, but subsequently found that a mistake had been made and the answer was again zero (43). Later, reasons will be given for supposing that $\omega(0)$ is identically zero to all orders of magnetic field.

We can now determine how a magnetic field perpendicular to the c-direction changes the $\hbar\omega(\pm k_o)$ energy gap given by Equation 30. Instread of solving for the $q=\pm k_o$ energies in Equation 47 directly, as we did with $\omega(0)$, it is convenient to solve for two energies using a symmetric and antisymmetric combination of operators and allowing coupling only to the q=0 and $q\neq\pm 2k_o$ states for simplicity (this corresponds to second-order perturbation theory (9)). The symmetric combinations of operators $(S_x(k_o) + S_x(-k_o);\ S_x(2k_o) + S_x(-2k_o);\ S_x(0))$ yield a frequency $\hbar\omega(\cos k_o)$, and the antisymmetric combinations of operators $(S_x(k_o) - S_x(-k_o);\ S_x(2k_o) - S_x(-2k_o))$ yield a frequency labeled $\hbar\omega(\sin k_o)$ when the determinant made from Equation 47 is evaluated to lowest order in H using the expansion Equation 49 for $\omega=\omega(\cos k_o)$ and $\omega=\omega(\sin k_o)$, respectively, where ω_o is given by Equation 30. The procedure is exactly the same as for evaluating $\omega(0)$ and the results are

$$[\hbar\omega(\cos k_o)]^2 = -2K_2(a_0+a_2) - (g\mu_B H)^2\{\frac{K_2S^2-a_0-a_2}{a_0+a_2}$$

$$+\frac{-2K_2S^2(2a_0+2a_2-a_3)+a_2(3a_3-16a_2)+a_0(4a_0+4a_2-a_3)}{8(a_0+a_2)^2}$$

$$+\frac{2K_2S^2(2a_0+2a_2-a_3)+a_3(a_0+a_2)}{4a_3(a_0+a_2)} \qquad (51)$$

$$+\frac{[K_2S^2(a_0-3a_2+a_3)+a_2(4a_2-a_3)][K_2S^2(a_0-3a_2+a_3)+a_2a_3]}{2(a_0+a_2)^2[K_2S^2(a_0+a_2-a_3)+a_2a_3]}\}$$

and

$$[\hbar\omega(\sin k_o)]^2 = -2K_2(a_0+a_2)+(g\mu_B H)^2\{\frac{2K_2S^2(2a_0+2a_2-a_3)+a_3(a_0+a_2)}{4a_3(a_0+a_2)}$$

$$+\frac{6K_2S^2(2a_0+2a_2-a_3)+a_0(4a_0+a_3)+a_2(4a_0+16a_2-5a_3)}{8(a_0+a_2)^2} \qquad (52)$$

$$-\frac{[K_2S^2(a_0-3a_2+a_3)+a_2(4a_2-a_3)][K_2S^2(a_0-3a_2+a_3)+a_2a_3]}{2(a_0+a_2)^2[K_2S^2(a_0+a_2-a_3)+a_2a_3]}$$

Equations 51 and 52 were derived making no approximations for K_2 being larger than the other terms. For $MnAu_2$, in fact, K_2 is not larger than the other terms. By assuming K_2 larger than the other terms, Cooper and Elliott (42, 43) derive expressions analogous to Equations 51 and 52

which are considerably less complicated and should be valid for the heavy rare earths. Cooper and Elliott (42) also show that an rf magnetic field along $\hat{\eta}$ (perpendicular to the dc field in the plane of the spiral) excites $\omega(\cos k_o)$ with an intensity typical of ferromagnetic resonance. An rf field along $\hat{\xi}$ (parallel to the dc field in the plane of the spiral) excites $\omega(\sin k_o)$, again with an intensity typical of ferromagnetic resonance.

Besides the $\omega(\cos k_o)$ and $\omega(\sin k_o)$ resonances, Cooper et al. (9) show that resonances of wavenumber $q=nk_o$, $n=2, 3, \ldots$ can be excited by a small dc field in the plane of the spiral. The procedure for calculating the intensity of excitation of a given harmonic follows the method shown for deriving Equation 28. If the rf magnetic field is parallel to $\hat{\eta}$, the Zeeman energy associated with this rf field is proportional to a sum on some Holstein-Primakoff operators multiplied by $\cos \phi_i$. One can expand $\cos \phi_i$ as

$$\cos \phi_i = \frac{1}{2} t_0 + \sum_{n=1} t_n \cos(n\vec{k}_o \cdot \vec{R}_i) \tag{53}$$

where t_n is given by

$$t_n = \frac{1}{\pi} \int_0^{2\pi} \cos \phi_i \cos(n\vec{k}_o \cdot \vec{R}_i) d(\vec{k}_o \cdot \vec{R}_i). \tag{54}$$

After a Bogoluibov transformation similar to Equation 20 with $q=nk_o$, it follows that the resonance absorption intensities for the various harmonics will be proportional to (9)

$$I(nk_o) \propto t_n^2(w_{nk_o}+b_{nk_o})^2 \cong t_n^2\left[\frac{-2K_2S+2a_n/S}{\hbar\omega(nk_o)}\right] \quad (55)$$

where Equation 29 and the assumption of small applied field were used to write the last term in Equation 55. Using Equation 22, the frequencies corresponding to these harmonics at H=0 are

$$[\hbar\omega(nk_o)]^2 = (-2K_2+2a_n/S^2)(a_{n-1}+a_{n+1}),\ n=1,\ 2,\ \ldots \quad (56)$$

or

$$a_{n+1} = \frac{[\hbar\omega(nk_o)]^2}{-2K_2+2a_n/S^2} - a_{n-1}\ . \quad (57)$$

Let us now use the specific example of $MnAu_2$ to illustrate the use of Equations 54 to 57. In the absence of any experimental determination of the frequencies given by Equation 56, an estimate of a_0 can be made by Equation 36 using H_c=10.5 kOe at T=0 K from Meyer and Taglang (38), and $g\mu_B S$=3.6 μ_B at T=0 K from Herpin and Meriel (37). In order to estimate a_2, we use a model of the magnetic interactions in $MnAu_2$ developed by Villain (44) and write the Hamiltonian (Equation 11) at equilibrium in the molecular field approximation as

$$\mathcal{H}/N = -4J_0S^2 - 8J_1S^2\cos\theta - 2J_2S^2\cos2\theta\ . \quad (58)$$

J_0 is the (positive) ferromagnetic interaction between a given

magnetic moment and its four nearest neighbors in the same atomic plane perpendicular to the c-axis, J_1 is the (positive) ferromagnetic interaction between a given magnetic moment and its eight nearest neighbors in the two nearest atomic planes perpendicular to the c-axis, and J_2 is the (negative) antiferromagnetic interaction between a given magnetic moment and its two nearest neighbors in the two next nearest atomic planes perpendicular to the c-axis. The angle θ is the turn angle between spins in adjacent atomic planes perpendicular to the c-axis and is about $51^\circ \cong 2\pi/7$ radians for $MnAu_2$. Equation 58 is minimized by setting $\partial\mathcal{H}/\partial\theta=0$, which gives us

$$\cos\theta = -J_1/J_2 \ . \tag{59}$$

From Villain (44) we also find

$$J(k_o) = \frac{3k_B T_n}{2S(S+1)} \tag{60}$$

and from Equation 12 for $q=q\hat{\zeta}$ we have

$$J(q) = 4J_0 + 8J_1 \cos qc' + 2J_2 \cos 2qc' \tag{61}$$

where c' is the distance between adjacent atomic planes perpendicular to the c-axis. Recall that $k_o c'=\theta$, so that using the definition given by Equation 43 with Equation 61, the exchange constants J_0, J_1, and J_2 can be found by solving simultaneously Equations 36, 59 and 60. Then by

using Equation 43 with Equation 61 the parameters a_n can be determined for all values of n. Some of the values obtained assuming $\theta=2\pi/7$ radians and $S=5/2$ are

$$\begin{aligned} J_0 &= 1.30 \text{ meV} \\ J_1 &= 0.039 \text{ meV} \\ J_2 &= -0.065 \text{ meV} \\ a_7 &= a_0 = 0.22 \text{ meV} \\ a_6 &= a_1 = 0 \\ a_5 &= a_2 = 1.12 \text{ meV} \\ a_4 &= a_3 = 3.25 \text{ meV} . \end{aligned} \tag{62}$$

The values in Equation 62 are likely to have large errors bars of at least $\pm 50\%$ because of the uncertain nature of the molecular field approximation for a substance with small spin (see Equation 27), and because there is an inconsistency that is difficult to resolve in the values of g and S used. We use g=1.92 because this is the experimental value obtained when $MnAu_2$ is paramagnetic well above the Néel temperature using the expression

$$\hbar\omega = g\mu_B H . \tag{63}$$

This value for g is close to the theoretical value of g=2 expected in the paramagnetic state of the Mn^{++} ion. We take S=5/2 because of the

Mn^{++} free ion spectroscopic state $^6S_{5/2}$. When these values are combined at T=0 K, however, the predicted magnetic moment on a given Mn^{++} ion is $g\mu_B S=4.8\ \mu_B$, or more than 1 μ_B greater than the experimentally observed magnetic moment using neutron diffraction (37). We expect that part of this discrepancy is due to zero point motion of the spins having an energy given by the second term in Equation 26, but if the zero point motion accounts for the complete discrepancy, the magnetic moment of a given spin along its equilibrium direction at T=0 K is about 75% of the value it would have without zero point motion. This is a large effect to be ascribed to zero point motion. The other alternative is to alter the values of g and/or S at low temperatures. It is found, however, that if g is altered by very much at low temperatures, the theoretically determined solid line in Figure 12 (for ferromagnetic resonance experiments to be described later) no longer fits the data. If we keep g=1.92, then S=2 gives $g\mu_B S=3.84\ \mu_B$, which is not far from the experimentally observed 3.6 μ_B (37). The problem is that it is impossible to determine a configuration for the free Mn ion giving S=2 and $g\tilde{=}2$ if quenching of the orbital angular momentum is not considered. It is true that the Mn ion is not free at low temperatures, but neutron diffraction studies by Wayne and Smith (45) have shown that the magnetic moment has atomic character (it is localized on the ion), so by analogy to the heavy rare earth ions at low temperatures one might expect Mn^{++} to have the free ion values S=5/2 and $g\tilde{=}2$

at low temperatures also. In practice we have always used g=1.92 and S=5/2 except in the determination of a_0 using Equation 36 where the experimental (37) $g\mu_B S=3.6\ \mu_B$ was used.

Using Equation 56, Equation 62 and the value $-2K_2=0.20$ meV obtained from our ferromagnetic resonance experiments described later, we obtain for the frequencies of the harmonics at H=0:

$$\begin{aligned}
\nu(7k_o) &= \nu(0) = 0 \\
\nu(6k_o) &= \nu(\pm k_o) \cong 125\ \text{GHz} \\
\nu(5k_o) &= \nu(2k_o) \cong 326\ \text{GHz} \\
\nu(4k_o) &= \nu(3k_o) \cong 564\ \text{GHz} \quad .
\end{aligned} \tag{64}$$

Equation 55 can now be applied to obtain the intensity of excitation expected for the harmonics of frequency given by Equation 64 excited by an rf magnetic field polarized along $\hat{\eta}$ when a small dc magnetic field is applied along $\hat{\xi}$. (The frequency $\nu(\pm k_o)$, however, does not need a magnetic field in order to be excited.) The results are

$$\begin{aligned}
I(0) &\propto t_0^2(\infty) \\
I(\pm k_o) &\propto 0.97 \\
I(2k_o) &\propto t_2^2(1.04) \\
&\vdots \\
I(7k_o) &\propto t_7^2(\infty) \quad .
\end{aligned} \tag{65}$$

Now by using Equations 54 and 62

$$t_2^2 = \tfrac{1}{4}t_0^2 = \frac{(\mu H)^2}{4(a_0+a_2)^2} \cong 10^{-4}H^2 \qquad (66)$$

where H is in kOe in the last term in Equation 66. Since H<10 kOe, we know $t_2^2<10^{-2}$, so $\hbar\omega(2k_o)\cong 326$ GHz is excited with an intensity at least two orders of magnitude less than $\hbar\omega(\pm k_o)\cong 125$ GHz. $\hbar\omega(\pm k_o)$ is considered to be excited with an intensity typical of ferromagnetic resonance because $I(\pm k_o)$ in Equation 65 is independent of H, and as $k_o \to 0$, $I(\pm k_o)$ gives the ferromagnetic resonance intensity as a special case. We do not concern ourselves with $I(0)$ because $\hbar\omega(0)=0$ at least to first-order in H, making the intensity of excitation irrelevant. For the other harmonics in Equation 65 there is little error in writing

$$I(nk_o) \propto t_n^2 < (\mu H)^{2(n-1)}, \quad n=3, 4, 5, 6 \qquad (67)$$

where (μH) has units of meV. For H in units of kOe, Equation 67 becomes approximately $I(nk_o) \propto (10^{-2}H)^{2(n-1)}$, so $I(3k_o) \propto 10^{-4}$ at H=10 kOe which is probably not observable. The harmonics up to and including n=6 are excited with even less intensity. The seventh harmonic, however, is a special case for $MnAu_2$ because $7k_o$ is almost exactly equal to the distance between adjacent points in the reciprocal lattice in the $\hat{\zeta}$ direction. The value $\hbar\omega(7k_o)=0$ given in Equation 64 would become finite if the turn angle θ was slightly greater than or less

than $2\pi/7$ radians. In order to see if $\hbar\omega(7k_o)$ could be observed at our relatively low experimental frequency of 24 GHz (if it existed there), we solve for t_7 to lowest order in H using Equations 54 and 41:

$$t_7 = \frac{A_1^6}{46,080} + \frac{A_1^4 B_2}{768} + \frac{B_2^3}{48} + \frac{A_1 B_2 C_3}{8} + \frac{A_1^3 C_3}{96} + \frac{C_3^2}{8} + \frac{A_1^2 D_4}{16} + \frac{A_1 E_5}{4} + \frac{F_6}{2} \tag{68}$$

where t_7 is evaluated numerically using Equations 42 and 62 to obtain $t_7 = 0.1(\mu H)^6$ for (μH) in units of meV. Now using Equation 55, where we set $\nu(7k_o)$=24 GHz, we obtain $I(7k_o) \propto 0.07(\mu H)^{12}$ for (μH) in units of meV. Thus at the maximum field of H=10 kOe, $I(7k_o) \propto 10^{-10}$, which is certainly not observable.

Because we have experimental frequences in the range of $\nu(\pm k_o)$=125 GHz given in Equation 64, we might expect with our experimental configuration (discussed later) to excite $\hbar\omega(\cos k_o)$ and $\hbar\omega(\sin k_o)$ given by Equations 51 and 52 and/or $\hbar\omega(+k_o)$ given by Equation 32 because we have a polycrystalline sample. (A polycrystalline sample has crystallites at all possible orientations with respect to the applied field, so all possible spin wave modes at a given frequency should be excited.) Note that Equations 32, 51 and 52 are identical when H=0. From Equations 51 and 52, however, using the parameters given by Equation 62 we see that $\hbar\omega(\cos k_o)$ and $\hbar\omega(\sin k_o)$ have little magnetic field dependence, so that if our experimental frequency is not almost exactly right we will

see nothing. It would be easier to see these modes by sweeping frequency. The $\hbar\omega(+k_o)$ mode, however, should be pulled down in frequency to 43 GHz (given by the first expression in Equation 35) at a field of about 66 kOe along the c-axis (given by $H_{o\ell}$ in Equation 33). Since we can sweep experimentally to over 50 kOe we should see this mode at an experimental frequency of 100 GHz if there are enough crystallites in the polycrystalline sample oriented with their c-axis along the applied field. Experimentally, however, we do not observe the $\hbar\omega(+k_o)$ mode (indicating that there are not enough crystallites with a c-axis along the applied field for absorption to be visible in our experimental apparatus). We also do not observe the $\hbar\omega(\cos k_o)$ or $\hbar\omega(\sin k_o)$ modes. At low frequencies like 35.6 GHz, for example, we expect to see no resonance absorption in the spiral region of $MnAu_2$. Since Asch (41) saw a resonance in this region at 6 kOe and 35.6 GHz at T=173 K, we performed experiments (to be described later) at even lower frequencies to determine the origin of this effect.

We now construct a simple model of a planar spiral spin system suggested by Professor Samuel H. Liu that can be solved exactly without having to make an expansion in powers of the magnetic field to obtain ϕ_i given by Equation 41. In this way a good indication can be obtained telling us whether or not $\hbar\omega(0)=0$ as given by Equation 50 only to first-order in H for a field applied in the plane of the spiral. In our model the equilibrium H=0 turn angle is $\theta=120^\circ$ and the crystal structure is assumed to be the same as for $MnAu_2$. The model developed by Villain (44)

for the exchange energies can be used, so the Hamiltonian can be written

$$\mathcal{H} = -J_0 \sum_{i,\alpha} S_i \cdot S_{i+\alpha} - J_1 \sum_{i,\beta} S_i \cdot S_{i+\beta} - J_2 \sum_{i,\gamma} S_i \cdot S_{i+\gamma} - K_2 \sum_i S_{i\zeta}^2 - g\mu_B H \sum_i S_{i\eta} \tag{69}$$

where α indexes the (positive) ferromagnetic interaction between the four nearest neighbors to the $i^{\underline{th}}$ atom in the same plane perpendicular to the c-axis, β indexes the (negative) antiferromagnetic interaction between the eight nearest neighbors to the $i^{\underline{th}}$ atom in the two nearest planes perpendicular to the c-axis, and γ indexes the (negative) antiferromagnetic interaction between the two nearest neighbors to the $i^{\underline{th}}$ atom in the two next nearest planes perpendicular to the c-axis. For $\theta=120^\circ$, an analysis similar to that used in deriving Equation 59 gives us $J_2=2J_1$. A magnetic field is applied in the $\hat{\eta}$ direction perpendicular to the c-axis which is lined up with one-third of the spins by symmetry (and energy) considerations. The molecular field approximation now gives an exact expression for the angle ϕ_i in the presence of a magnetic field. The spins close continuously until they become ferromagnetic. The solution for the spin wave energies now proceeds by putting Equation 69 in the form indicated by Equation 44 and using the equations of motion method of solution indicated by Equation 45. The major complication is the necessity of dividing the lattice into three interpenetrating sublattices when a magnetic field is applied to account

for the fact that there are three sets of turn angles between spins in nearest and next nearest planes, depending on which plane is measured from. Because the separation between atoms in one of the three interpenetrating sublattices is three times as great as for the real lattice, all Fourier transforms similar to Equation 46 are carried out for $\vec{q}$ defined in only one-third of the first Brillouin zone of the real lattice (called the magnetic superzone). States are counted as before using periodic boundary conditions so that there are N/3 allowed values of $\vec{q}$ in the magnetic superzone. In the end (after some simplifications) it is necessary to solve a 3X3 determinant for the spin wave frequencies. The exact solutions setting q=0 are three frequencies given by

$$\hbar\omega = 0$$

$$(\hbar\omega)^2 = 36J_1K_2S^2 + 2K_2\mu H + \frac{1}{S^2}\left(1+\frac{K_2}{12J_1}\right)(\mu H)^2 \qquad (70)$$

$$(\hbar\omega)^2 = 36J_1K_2S^2 - 2K_2\mu H - \frac{K_2}{12J_1S^2}(\mu H)^2 \quad .$$

Since we solved for these expressions in the magnetic superzone, we identify $\hbar\omega=0$ in Equation 70 with $\hbar\omega(0)=0$ given by Equation 50, and the other two energies in Equation 70 with $\hbar\omega(\cos k_o)$ and $\hbar\omega(\sin k_o)$ given by Equations 51 and 52. The magnetic superzone is a reduced zone scheme which automatically "folds back" the $q=k_o$ energies to q=0 in Equation 70. The comparison between the first expression in Equation 70

and the expression given by Equation 50 is the basis for our assertion that $\hbar\omega(0)=0$ probably to all orders of H for a field applied in the plane of a spiral of arbitrary turn angle. A general proof that $\hbar\omega(0)=0$ to all orders of H for a field applied in the plane of a spiral of arbitrary turn angle is given by Elliott and Lange (46) under assumptions appropriate to $MnAu_2$. Another interesting comparison between Equation 70 and Equations 51 and 52 is the fact that $\hbar\omega(\cos k_o)$ and $\hbar\omega(\sin k_o)$ have no linear field dependence, whereas the comparable energies in Equation 70 have a linear field dependence. The linear field dependence in Equation 70 might be characteristic only of a $\theta=120^\circ$ spin system, or it might indicate a more general error (perhaps due to not allowing q to be coupled to multiples of k_o higher than two) in Equations 51 and 52.

We now discuss the fan region in $MnAu_2$ where an applied field in the plane of the spiral has a value between H_c (given approximately by Equation 36) and H_f (given approximately by Equation 37). Cooper and Elliott (42) derive expressions for spin waves excited in this region by an rf magnetic field, but some of their expressions contain errors. Corrections to these errors are found in Reference (43), and the correct solutions are

$$\hbar\omega(0) = g\mu_B\left[H(H+H_A) - \frac{2a_0H_A(H_f-H)}{2a_0+a_2}\right]^{\frac{1}{2}} \qquad (71)$$

and

$$\hbar\omega(\sin k_o) = [-4K_2\mu(H_f - H)]^{\frac{1}{2}} \tag{72}$$

where

$$H_A = \frac{-2K_2S}{g\mu_B} \quad . \tag{73}$$

The applied magnetic field is along $\hat{\xi}$ in the plane of the spiral. An rf field along $\hat{\eta}$ excites $\omega(0)$ given by Equation 71 with an intensity essentially the same as ferromagnetic resonance. An rf field along $\hat{\xi}$ excites $\omega(\sin k_o)$ given by Equation 72 with an intensity that goes to zero in the same way the frequency goes to zero. We might expect to excite $\hbar\omega(\sin k_o)$ in Equation 72 with fairly weak intensity using correctly polarized low frequency microwaves at a field slightly below H_f. The $\hbar\omega(0)$ mode in Equation 71 is just a continuous extension of the ferromagnetic resonance conditions discussed next.

In the ferromagnetic region, where the applied magnetic field along $\hat{\xi}$ in the plane of the spiral is greater than H_f (given approximately by Equation 37), there is only one mode excited by an rf field along $\hat{\eta}$ (8):

$$\hbar\omega(0) = g\mu_B[H(H+H_A I_{5/2}\sigma^{-1})]^{\frac{1}{2}} \tag{74}$$

where $I_{5/2}$ and σ are defined the same as for Equation 1. We have neglected demagnetizing effects in Equations 71, 72, and 74. Demagnetizing

effects can be included in Equation 74 by following Kittel (22) to get

$$\hbar\omega(0) = g\mu_B \{[H+(N_\eta-N_\xi)M][H+H_A I_{5/2}\sigma^{-1}+(N_\zeta-N_\xi)M]\}^{\frac{1}{2}} . \qquad (75)$$

We now specialize Equation 75 to the case of a polycrystalline sample, and include the wavenumber dependence of the demagnetizing effects in the same manner as discussed for Tb in the section following Equation 2. The crystallites in our sample were about a factor of ten larger than the microwave skin depth, and we assume that spin waves do not propagate across grain boundaries. The effective thickness of the sample participating in the uniform mode is therefore essentially zero because the grain size is about 10 microns. This means $N'=0$ for the uniform $q=0$ mode following the Tb discussion, which means that in Equation 75 $N_\eta-N_\xi=-N$ and $N_\zeta-N_\xi=4\pi-N$ where N is the static demagnetizing factor that can be obtained from tables (24) for an applied field in the plane of a thin disk sample of given dimensions.

If the non-uniform $q=0^+$ mode that is also excited by microwaves is now considered (by analogy to the Tb discussion in section II B), we must set $N_\zeta=N_\eta=0$ as a mathematical way to compensate for the fact that the transverse components of magnetization M_ζ and M_η are now zero macroscopically. Since M_ξ remains essentially unchanged when spin waves are excited, the factor N_ξ is again the static demagnetizing factor that can be obtained from tables (24) the same as for the uniform mode. The formalism of Kittel (22) used to derive the demagnetizing

effects in Equation 75 treats the magnetization as a microscopic quantity, whereas the magnetization used in demagnetizing effects is the macroscopic magnetization. Instead of changing the formalism of Kittel we compensate for the wavenumber dependence of the macroscopic magnetization by giving the demagnetizing factors a compensating wavenumber dependence (the expression $N_\xi+N_\eta+N_\zeta=4\pi$ is no longer satisfied for the sample as a whole). For Equation 75 in the $q=0^+$ mode we obtain

$$\hbar\omega(0^+) = g\mu_B\{[H-N_\xi M][H+H_A I_{5/2}\sigma^{-1}-N_\xi M]\}^{\frac{1}{2}} \quad . \tag{76}$$

From Equation 76 we see that the internal field is the field that acts in the $q=0^+$ mode. At our high experimental frequency of 100 GHz, Wagner and Stanford (14, 15) have found that only the non-uniform $q=0^+$ mode is excited in Tb and Dy with observable intensity (as discussed in the Tb section of this thesis). By analogy, we assume that our ferromagnetic resonance results at 100 GHz in $MnAu_2$ are explained by the $q=0^+$ expression given in Equation 76. By applying Equation 76 to resonances at more than one frequency (see Figure 12), estimates of both g and H_A can be made at low temperatures. Then by using Equation 75 a value of $-2K_2$ can be obtained by assuming S=5/2.

C. Sample Preparation

The correct amounts of Mn (99.99%) and Au (99.9999%) were melted together under an argon atmosphere. A thin disk sample 0.244 in. diam and 0.021 in. thick was spark cut from the ingot and annealed at 700° C for 36 hours. It was then polished for 18 hours on the Syntron vibrator

using 0.1 micron diam alumina powder for a preliminary polish and a soft cloth for a final polish. Two other samples from the same melt were annealed and polished in the same manner. One was submitted to the electron microprobe for analysis, and the other was etched with aqua-regia to show the grain boundaries. An "average" grain was about 10 microns in diam. Part of the original ingot was also submitted for chemical analysis.

The chemical analysis showed a slight excess (1.4% by weight) of gold as compared to ideal $MnAu_2$. By contrast, the electron microprobe showed an excess (2.8% by weight) of manganese, but this excess deviates from ideal $MnAu_2$ within the experimental error of the microprobe. The microprobe also showed that the composition of the sample was uniform except for a few small spots, some Mn rich and some Mn poor. To ensure that the major matrix of the sample was in fact ordered $MnAu_2$, the lattice parameters of the disk were determined (on the actual sample used) by placing it in a back-reflection focusing camera and observing the Bragg reflections. Copper K_α radiation was used and the Bragg reflections were analyzed using the method outlined by Cullity (47). Assuming a body-centered tetragonal unit cell, the lattice parameters were measured to be $a=3.369\pm0.001$ Å and $c/a=2.599\pm0.001$ Å. These values are in exact agreement with those quoted for ordered $MnAu_2$ by Smith and Street (36). Also, disordered $MnAu_2$ has been reported to have $c/a=2.76$ by Raub *et al.* (35). The measured lattice parameters were used to calculate the ideal density

of $MnAu_2$ giving 15.00 g/cm^3. Using our sample dimensions and the weight of the sample (0.2460 g), the density of our sample is 15.04 g/cm^3, in very good agreement with ideal $MnAu_2$.

Several attempts were made to grow a single crystal of $MnAu_2$. Two fingers of polycrystalline $MnAu_2$ from the same ingot as the sample (both $\frac{1}{4}$ in. diam, and $\frac{1}{4}$ in. and $\frac{1}{2}$ in. in length, respectively) were pressed until their length changed by a few percent. They were then annealed for several days at 700° C and grain growth by a factor of 10 was observed so that the crystallites now were barely visible to the naked eye (0.1 mm diam) after etching in aqua regia. Unfortunately, however, an attempt to repeat the process to obtain more grain growth failed when the gold appeared to separate partially from the manganese.

Mr. J. A. Herriott and Mr. M. J. Murtha of the Ames Laboratory attempted to use the "crystal pulling" technique to grow a single crystal of $MnAu_2$ using a melt with the correct amounts of Mn and Au, and a polycrystalline $MnAu_2$ sample for a seed crystal. The attempt was unsuccessful, partly because of difficulty in keeping the two metals Au and Mn from separating in the melt.

D. Apparatus

The 24 GHz apparatus is shown schematically in Figures 1 and 2. These figures have already been discussed for Tb. The $MnAu_2$ sample was mounted in the same manner as the smaller Tb sample (using a copper washer and GE 7031 varnish for glue) except that it was not necessary

to worry about crystal alignment. For very low temperature work (below 40 K) a second thermocouple was soldered to the cavity along with the copper-constantan thermocouple used for higher temperatures (see Figure 2). This second thermocouple was gold-0.03 atomic percent iron vs copper (48). When signal amplitude vs temperature runs were made with the 24 GHz apparatus, the klystron power was held constant and the changes in cavity coupling with temperature in zero applied field were compensated for by adjusting the slide screw tuner so that the crystal current remained constant.

The 100 GHz apparatus is shown schematically in Figure 10. The sample was glued (using GE 7031) to a cylindrical plunger fitted into a cylindrical cavity in such a way that it could be moved back and forth by a rack and pinion gear system to tune the cavity from outside the enclosing vacuum jacket. The polished mirror image reflected in the sample makes the cavity system shown in Figure 10 approach a confocal resonator (49). The cavity was made of brass and was isolated from the walls of the enclosing vacuum jacket by using nylon screws as spacers.

The enclosing vacuum jacket fit inside the bore of a superconducting solenoid designed by Dr. D. R. Stone which produced a magnetic field parallel to the plane of the sample disk. The superconducting solenoid was in the innermost of two chambers isolated by two vacuum spaces. Liquid helium was maintained in the innermost chamber in order to make the solenoid superconducting, and the liquid nitrogen in the outer

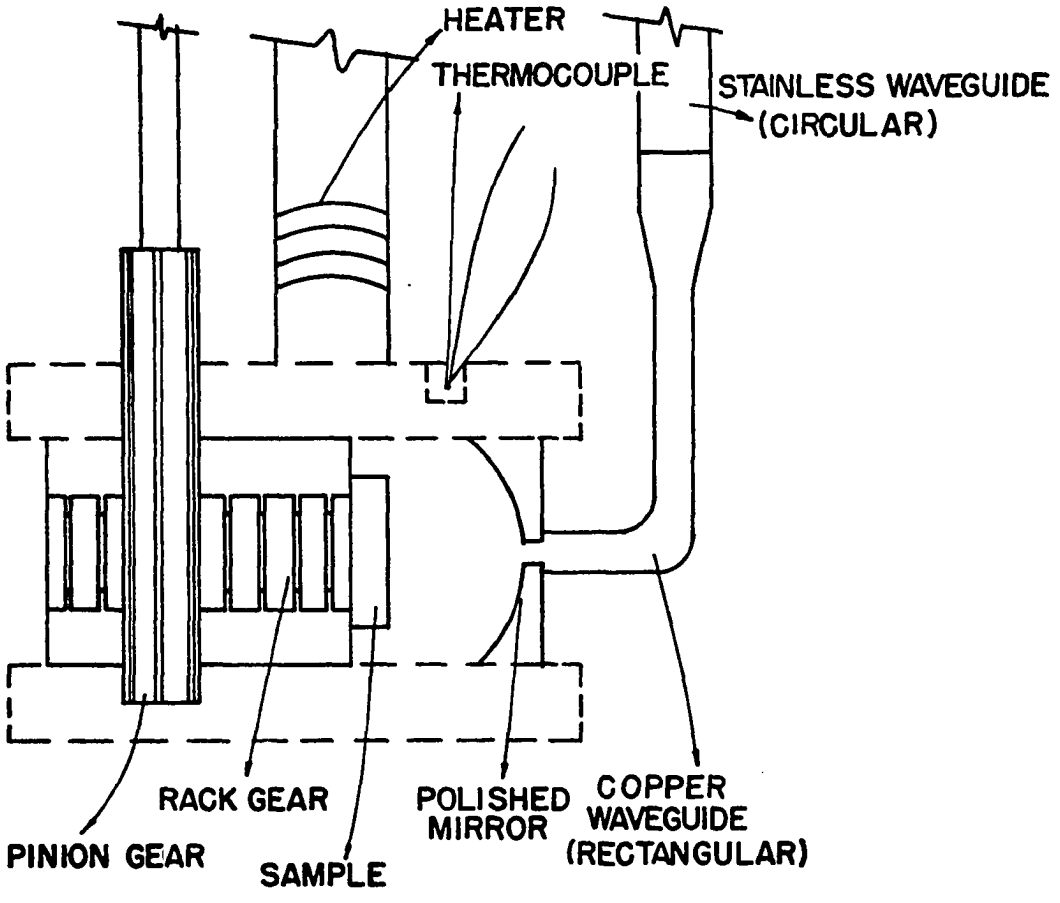

Figure 10. Diagram of 100 GHz microwave cavity.

chamber served as a radiation shield for the liquid helium. (Helium transfer gas at a pressure of 100 microns of Hg in the vacuum jacket maintained the sample at the bath temperature of 4.2 K if desired.) Mylar plastic transmits microwaves, and was therefore used to seal the waveguide entering the vacuum jacket. Conax seals for the heater and thermocouple wires, and two pressure fitted O-rings for the flexible rod attached to the pinion gear, were used to seal the vacuum jacket. The vacuum jacket itself could be disassembled to introduce the cavity and then sealed again with an O-ring.

Circular stainless steel waveguide of 3/16 in. i.d. was used throughout most of the length of the vacuum jacket to cut down the heat leak from the top of the dewar and because the attenuation of the microwaves is much less in a circular waveguide (because of the low cutoff-frequency of the dominant mode) than it is in rectangular waveguide (0.040 in. X 0.080 in.) of the same material (31). A gradual transition between the two types of waveguide was made in an Ames Laboratory shop by Mr. Harry Amenson using high temperatures to shape the copper waveguide. The rectangular waveguide operates on the TE_{10} mode between the frequencies of 74 and 148 GHz. It was positioned in the polished brass mirror (see Figure 10) so that the rf magnetic field in the waveguide entered the cavity perpendicular to the dc magnetic field. If a degenerate mode like the TE_{111} mode in a circular cavity (described in the Tb section) is excited, then $H_{rf} \perp H_{dc}$ will predominate and ferromagnetic resonance is observable. If a mode like the TM_{010} mode (31)

in a circular cavity is excited, ferromagnetic resonance should also be seen. It is not necessary to worry about polarization studies because with the system shown in Figure 10, H_{rf} cannot be rotated with respect to H_{dc}. The actual rf magnetic field configuration for the confocal resonator which our system approximates can be calculated using Reference (49), but this is not necessary when polarization studies are not performed. All that is necessary is that a component of rf magnetic field be perpendicular to the applied field, and this is assured by the cylindrical symmetry of the cavity configuration in Figure 10 with the waveguide coupled to the cavity as previously described.

The block diagram for the electronics (Figure 1) is the same for the 100 GHz gear except that the cavity and magnet configuration is different (as shown in Figure 10), and the klystron frequency is determined using a flat-plate interferometer designed by Dr. J. L. Stanford and constructed in the Ames Laboratory (50). The only other difference between the 24 and 100 GHz electronics is the power supply and field-sweep mechanism used for the superconducting magnet. A small resistance is placed in series with the large inductance of the superconducting magnet so that when 2 or 3 volts are maintained across this R-L circuit the current increases almost linearly for a time τ given by the time constant of the system, $\tau=L/R$. (Our superconducting magnet takes a maximum current of 20 A.) In order to sweep down in field, a diode is placed in parallel with the R-L circuit, so that going up in

current it is out of the circuit, but when the power supply is turned off it short circuits the power supply and the current decreases almost linearly with the same time constant $\tau=L/R$. The current passing through the solenoid was measured by measuring the voltage across a standard resistor in the R-L circuit, and the magnetic field generated in the solenoid was assumed to be a linear function of this current.

The heater for the 100 GHz gear (see Figure 10) was made of manganin wire with a resistance of 30 ohms, and the thermocouple was copper vs constantan.

E. Experimental Results

We shall describe our high frequency results in the vicinity of 100 GHz first. Reference (51) is the published version of these results. Figure 11 shows representative examples of power absorption as a function of applied field. Since all of the peaks in power absorption occur above an applied field of 20 kOe (see Figure 12), it follows that the peak in power absorption takes place in the ferromagnetic phase of $MnAu_2$ (above H_f given by Equation 37) for a field applied perpendicular to the c-axis (37, 38). Figure 12 shows that Equation 76 explains the temperature dependence of the data at 102.4 GHz very well using the polycrystalline magnetization data of Meyer and Taglang (38) to determine σ, and values of g and H_A to be discussed later, so we interpret the power absorption peaks in Figure 11 as ferromagnetic resonance. The magnetostriction (52) has a large increase in value above a magnetic field of about 10 kOe, but the trend is for this

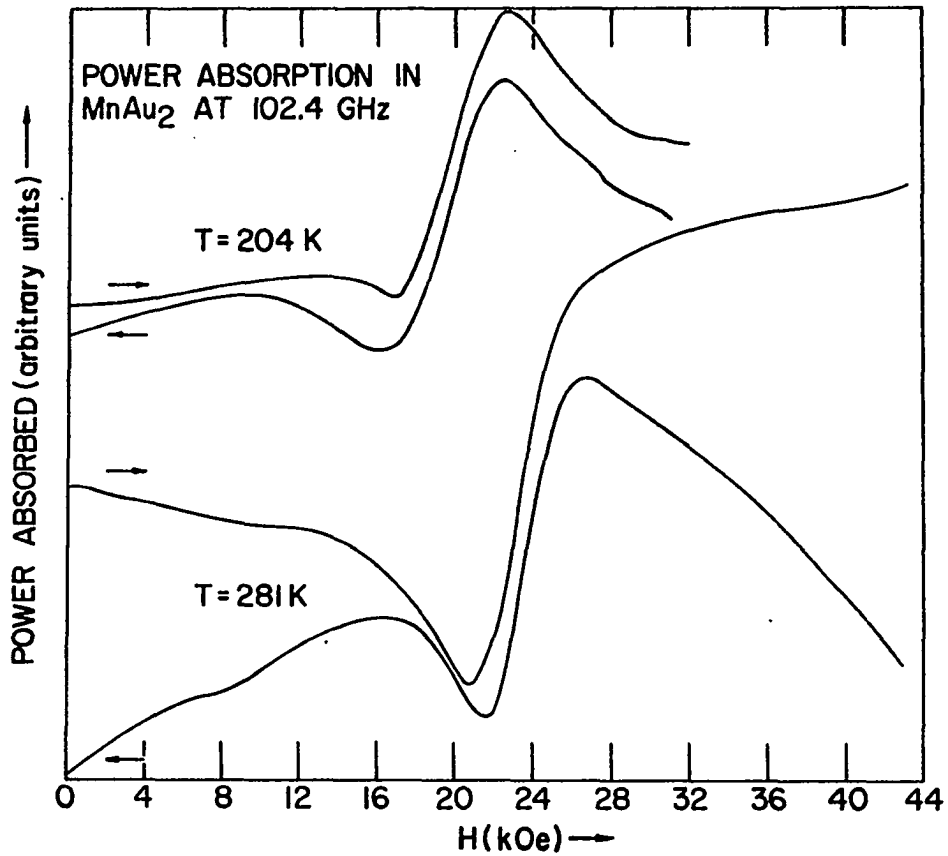

Figure 11. Tracings of typical power absorption vs applied magnetic field curves for $MnAu_2$ at 100 GHz.

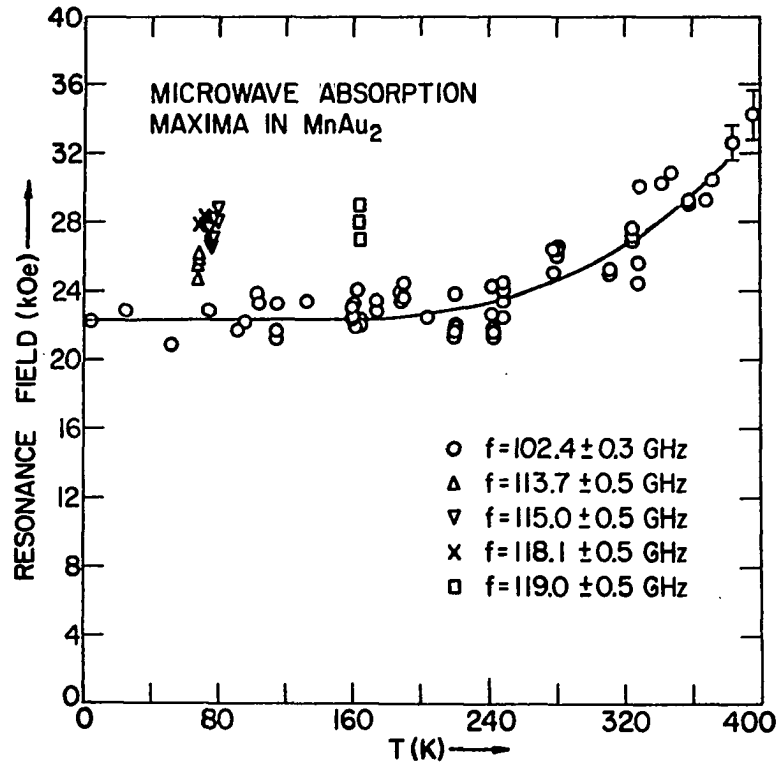

Figure 12. Plot of resonance field vs temperature for $MnAu_2$ at several different microwave frequencies. The solid line is the theoretical temperature dependence using Equation 76 and the parameters given in the text.

magnetostriction to occur at somewhat lower fields with increasing temperature, a trend that is opposite to the trend for ferromagnetic resonance shown in Figure 12. We therefore conclude that the data shown in Figures 11 and 12 are not due to magnetostriction. The data in Figures 11 and 12 are not due to domain alignment effects either, because domain alignment effects have about the same temperature dependence as the magnetostriction (38, 52).

Often the data had a poorly defined peak, as depicted in Figure 11. Cooper and Elliott (42) discuss resonance for a polycrystal like $MnAu_2$ and conclude that a trailing edge (large resonance linewidth) is the main effect of the polycrystalline nature of the sample because it is essentially the component of applied magnetic field in the spiral plane of a randomly oriented crystallite that contributes to resonance absorption. It is assumed that because of the reasonably large uni-axial anisotropy of $MnAu_2$, the spins remain essentially perpendicular to the c-axis of the randomly oriented crystallite for the resonance fields in Figure 12. When the component of applied field in the spiral plane of a crystallite reaches the resonance field solved for from Equation 76 at a given frequency, then ferromagnetic resonance for that crystallite occurs, contributing to the trailing edge of the resonance. Cooper and Elliott (42) show that the peak in power absorption should be due to those crystallites oriented with the c-axis approximately perpendicular to the applied magnetic field, so the polycrystalline peaks in power absorption shown in Figures 11 and 12 should be described in Equation 76.

At some temperatures very severe hysteresis effects with field cycling were observed. At 68 K and 113.7 GHz, for example, the resonant peak in power absorption increased monotonically with each field sweep until a saturation value was reached. On the first up-sweep, H=24.8±0.6 kOe, while for the third up-sweep, H=26.2±0.8 kOe. Subsequent sweeps yielded values near 26 kOe. We believe these effects are associated with the polycrystalline nature of our sample, together with the large magnetostrictive effects that are known to occur in $MnAu_2$ (51). At other temperatures these hysteresis effects are not as severe, but still preclude an accurate determination of the resonance field. The uncertainty in H_{res} is usually 3% - 5% or more. Analyzing Equation 76 for all the frequencies shown in Figure 12 at low temperatures, we can solve for both g and H_A. We use statistics to determine the errors by assuming that the scatter in Figure 12 is random. Any two frequencies with associated resonance fields shown in Figure 12 give a solution of Equation 76 for g and H_A with a certain error given by a standard deviation. When all combinations of two frequencies are used to solve for values of g and H_A, these values are combined to obtain a best value of g and H_A with their standard deviations using weighting factors of unity. Weighting factors of unity are used because we doubt whether the scatter in the data in Figure 12 is completely random. We suspect that the data at one frequency is as good as the data at any other frequency regardless of the scatter. The scatter may be partly random, but it may also be somewhat frequency

dependent. With weighting factors of unity, our data and Equation 76 give us g=1.9±0.4 and H_A=50±30 kOe. These results may be compared with Asch's (41) determination of g=2 and our determination of g=1.92 (to be discussed later) in the paramagnetic phase of $MnAu_2$, and with a value of H_A=50 kOe obtainable by extrapolating the low temperature magnetization work of Meyer and Taglang (38) on $MnAu_2$ in an applied field. Our value g=1.92 in the paramagnetic phase was determined from Equation 63 at a higher temperature than the g=2 value of Asch, so it should more nearly correspond to a Mn^{++} ion in $MnAu_2$, isolated (as far as magnetic interactions are concerned) from the other Mn^{++} ions. Because we know the moments on the Mn^{++} ions are localized (45), we assume that magnetic ordering at low temperatures does not change the g value. If g=1.92 is taken at low temperatures also, Equation 76 evaluated for the 102.4 GHz data at low temperatures gives H_A=45 kOe, and these values for g and H_A along with the magnetization data of Meyer and Taglang (38) were used to determine the solid line in Figure 12 which provides a good fit to the temperature dependence of the 102.4 GHz data. The solid line in Figure 12 is quite sensitive to the values of g and H_A chosen. If g=1.6 is taken, for example, Equation 76 does not follow the high temperature data at 102.4 GHz in Figure 12 if H_A is chosen to fit the low temperature data. The theory is consistent with the experimental results of other workers (38, 41, 45) and with our own experimental results by taking g=1.92 and H_A=45 kOe at all temperatures in Equation 76. Using H_A=45 kOe and S=5/2 we obtain $-2K_2$=0.20 meV.

As discussed in the theory section, we expect to observe only a weak $\hbar\omega(\sin k_o)$ mode given by Equation 72 in the fan region of $MnAu_2$ with our low frequency (24 GHz) gear. We may have observed this mode; its discussion will be postponed until later. To our surprise, we observed two apparent resonances in the spiral region in $MnAu_2$, one of which appears to correspond to the resonance observed by Asch (41) at 6 kOe and 35.6 GHz at a temperature of 173 K. (We will discuss later why we believe these peaks are not due to impurities in the sample.)

Figure 13 gives representative examples of the data showing many peaks in power absorption. Perhaps the easiest to understand is the paramagnetic peak at T=375 K (above the Néel temperature). More paramagnetic data is plotted using closed circles in Figure 14, and the highest temperature data (at T=440 K) corresponds to g=1.92 using Equation 63 as previously mentioned. Figure 15 shows how the amplitude of the paramagnetic peak falls off with increasing temperature using closed circles corresponding to the data in Figure 14. The open circles labeled A in Figure 16 show that the amplitude of the paramagnetic resonance has a $\sin^2\phi$ dependence as expected for a true paramagnetic resonance absorption where ϕ is the angle between H_{rf} and H_{dc}.

The data in Figure 13 at T=300 K shows a peak at about 3 kOe and a small peak at about 7 kOe (visible most strongly on the first curve). Both of these peaks are in the spiral phase of $MnAu_2$. The peak at T=78 K in Figure 13 is the same as the small peak at 7 kOe

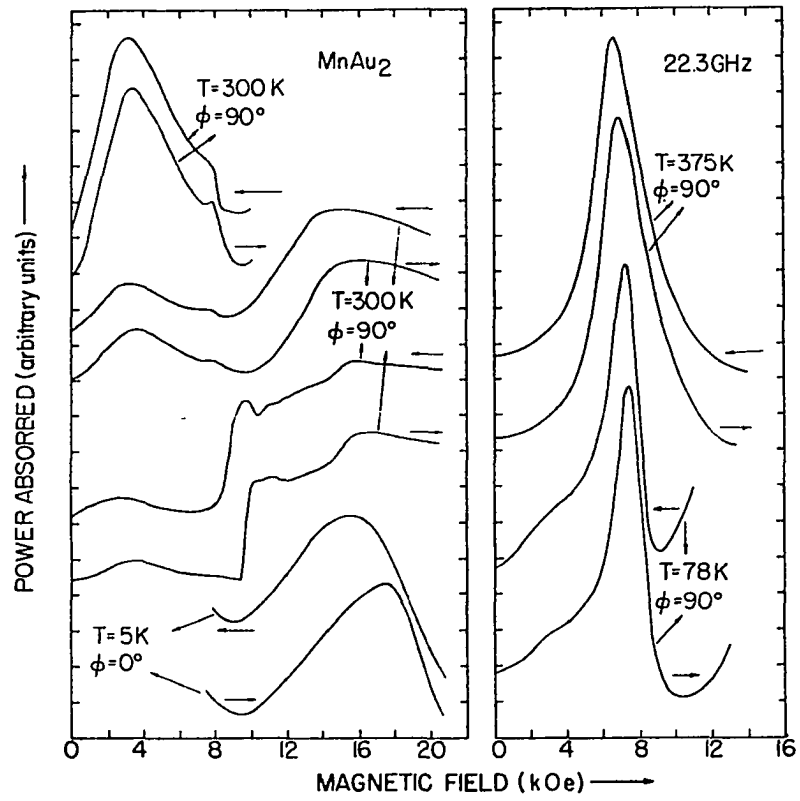

Figure 13. Tracings of typical power absorption vs applied magnetic field curves for $MnAu_2$ at 22.3 GHz. ϕ is the angle between H_{rf} and H_{dc}.

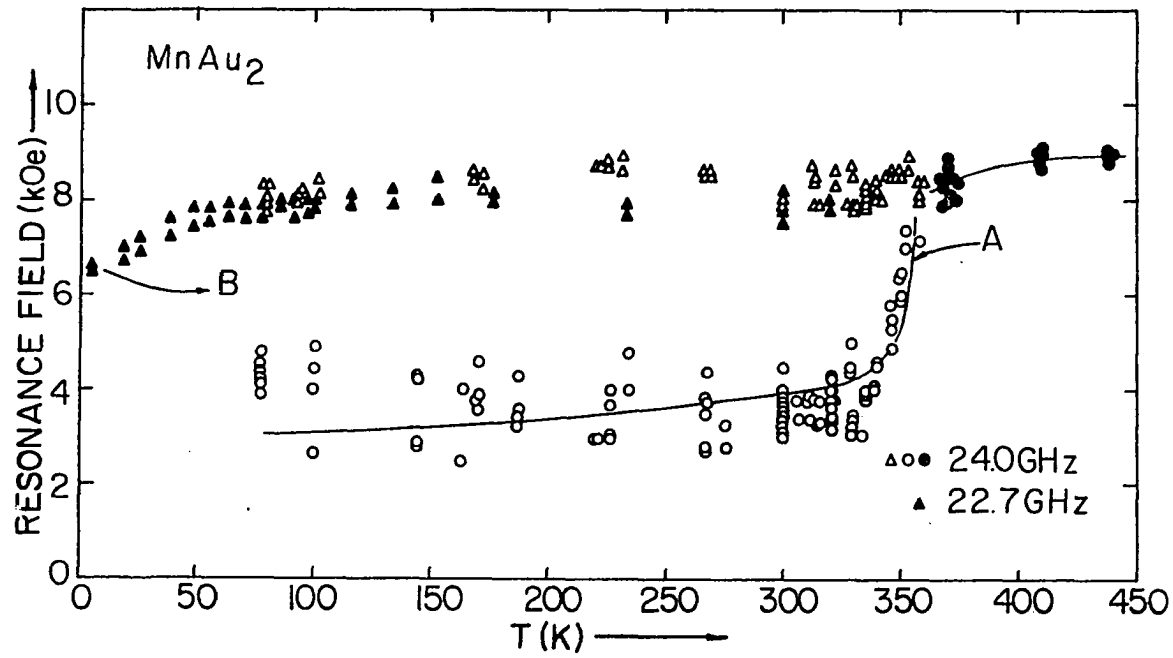

Figure 14. Plot of the field values of power absorption maxima as a function of temperature for peaks interpreted as resonance absorption in $MnAu_2$. The closed circles are paramagnetic resonance, the open circles are interpreted as "surface" ferromagnetic resonance in the spiral phase, and the open and closed triangles are interpreted as paramagnetic resonance in the spiral phase. The letters are as follows: A, theoretical ferromagnetic resonance curve using Equation 74 with parameters discussed in the text. B, field position corresponding to g=2.5 using Equation 63 at T=5 K.

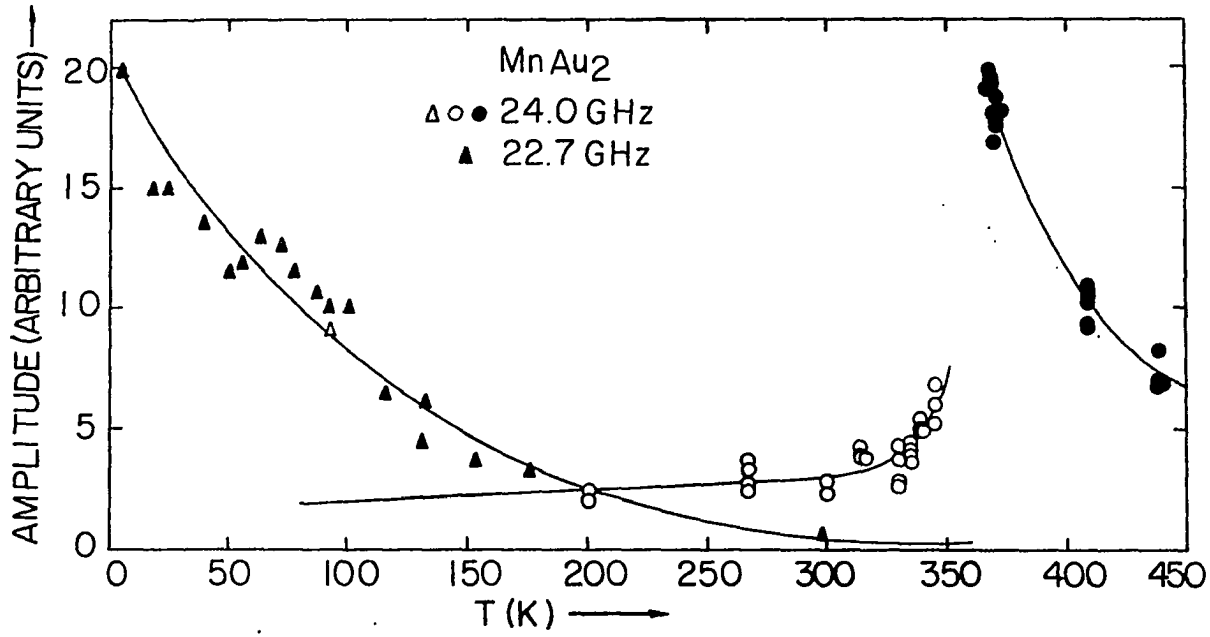

Figure 15. Plot of the amplitudes of power absorption maxima as a function of temperature for the peaks interpreted as resonance absorption in Figure 14 (using the same symbols as Figure 14 for corresponding peaks). All amplitudes, even at different frequencies, should be comparable in this figure. The zero of amplitude was taken as H=0, and only the amplitude of the peak for field increasing with time was plotted.

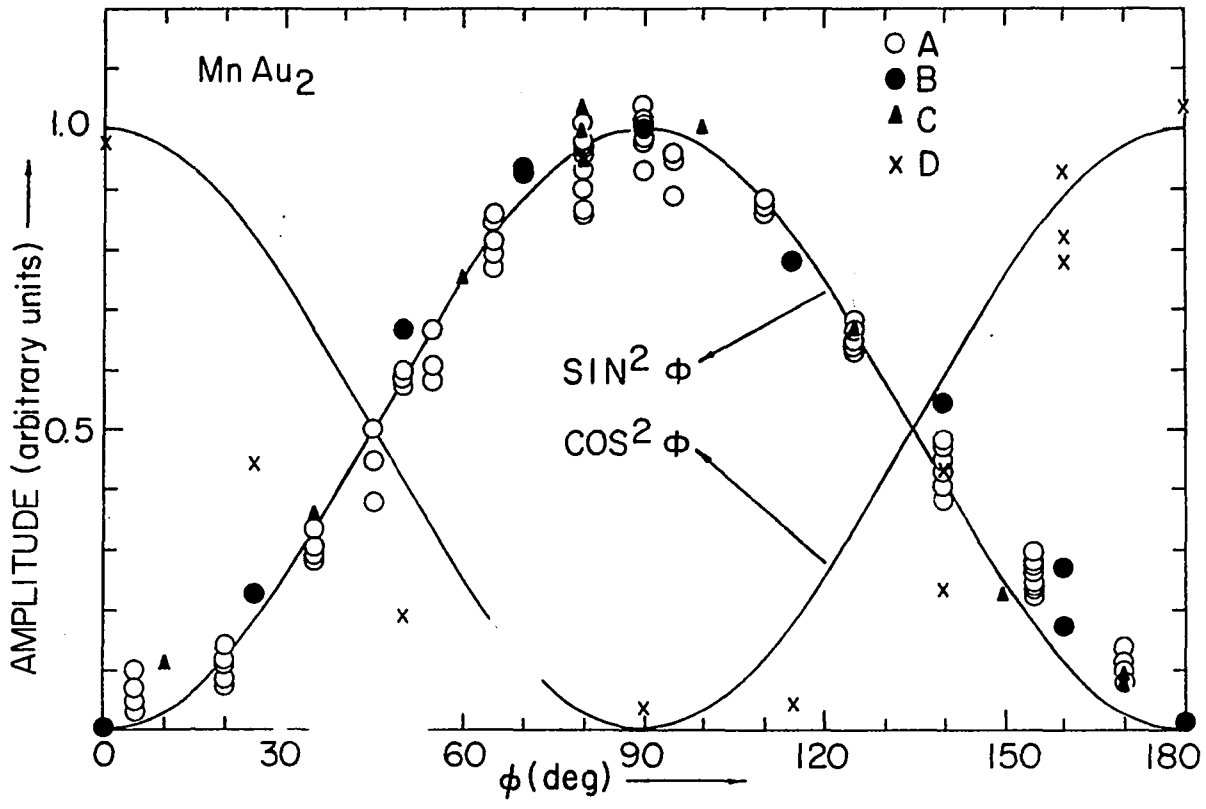

Figure 16. Plot of the amplitudes of power absorption maxima as a function of the angle (ϕ) between H_{rf} and H_{dc} in $MnAu_2$. The letters are as follows: A, paramagnetic resonance at T=371 K. B, "surface" ferromagnetic resonance in the spiral phase at T=298 K. C, paramagnetic resonance in the spiral phase at T=78 K. D, possible $\hbar\omega(\sin k_o)$ resonance in the fan phase given by Equation 72 at T=5 K.

and T=300 K, but it is much larger at low temperatures. For reasons that will become apparent hereafter, we call the peak at 3 kOe the "surface" ferromagnetic peak, and the peak at 7 kOe the "spiral phase" paramagnetic peak. The "surface" ferromagnetic peak is shown as a function of temperature by the open circles in Figure 14. The open and closed triangles in Figure 14 show the temperature dependence of the "spiral phase" paramagnetic peak. The amplitudes as a function of temperature of the "surface" ferromagnetic and "spiral phase" paramagnetic peaks are shown in Figure 15, and their amplitudes as a function of the angle between H_{rf} and H_{dc} are shown in Figure 16. Figure 16 shows that the "surface" ferromagnetic and "spiral phase" paramagnetic peaks have the $\sin^2\phi$ amplitude dependence expected of true ferromagnetic or paramagnetic resonance absorption.

The "surface" ferromagnetic resonance will now be discussed in more detail. The solid line labeled A in Figure 14 is a plot of the ferromagnetic resonance condition Equation 74 without demagnetizing factors. Meyer and Taglang (38) show that there is very little macroscopic magnetization in the spiral region where the "surface" ferromagnetic resonance occurs, so we neglect demagnetizing factors. The parameter H_A was chosen by fitting Asch's (41) low temperature peak at 35.6 GHz, 6 kOe and T=173 K to Equation 74. We took $I_{5/2}\sigma^{-1}=1$ and g=1.9 at T=173 K to obtain H_A=23 kOe. We used the magnetic moment on a given spin vs temperature data obtained by neutron diffraction at H=0 in the spiral phase of $MnAu_2$ to determine σ for the temperature

dependence of Equation 74. For the small resonance fields ($\tilde{=}$3 kOe) of the "surface" ferromagnetic peak at our experimental frequency, we would expect these H≠0 values of σ to be almost correct. As can be seen by line A in Figure 14, the temperature dependence of our low field data is well explained by assuming the data are due to ferromagnetic resonance with H_A=23 kOe, or about half the H_A=45 kOe value determined by our bulk ferromagnetic resonance studies described previously. (If we take H_A=45 kOe and g=1.4, we can fit the low temperature data given by the open circles in Figure 14 using Equation 74, but then the temperature dependence of Equation 74 does not fit the data near the Néel temperature.) Note that the large data scatter about line A is comparable to the scatter about the solid line in Figure 12, also for ferromagnetic resonance. The "surface" ferromagnetic peaks also have large linewidths as do the bulk ferromagnetic peaks at 102.4 GHz (compare Figures 11 and 13).

We call the low field peaks "surface" ferromagnetic resonance because at the field at which the resonance occurs the bulk sample is in a spiral structure as determined by neutron diffraction (37). We assume that an applied field in the spiral phase causes some magnetic moments in the surface layer of the sample to become ferromagnetic because the long range oscillatory exchange interaction producing the spiral phase in the bulk sample cannot act equally in all equivalent crystallographic directions at the surface.

Line B in Figure 17 gives the frequency as a function of resonance field for Equation 74 at T=300 K using the parameters just discussed for the surface ferromagnetic resonance. The fit to the data shown is considered reasonable but a few comments should be made. First, even though H_A=23 kOe was determined by fitting Asch's (41) T=173 K data, the fit to his data at T=300 K in Figure 17 is not perfect. This could be due to difficulty in picking the peak maximum because it is so broad, or to a slight breakdown in the assumption that the H=0 neutron diffraction data can be used to determine σ for the $H\cong 8$ kOe data of Asch at T=300 K. Our lowest frequency data (20.4 GHz) in Figure 17 with a resonance field $H\cong 2$ kOe were very weak in intensity, perhaps indicating that an applied field of a certain magnitude is necessary to induce the surface ferromagnetic state. A value H_A=26 kOe in Equation 74 would better fit the 20.4 GHz, $H\cong 2$ kOe data, but this is not much different from the H_A=23 kOe values plotted in Figure 17. In any case, the value of H_A might very well be somewhat dependent on the value of resonance field for a field-induced surface ferromagnetic resonance. Asch (41) used a frequency of 9.3 GHz at T=300 K on his $MnAu_2$ sample and saw nothing up to H=20 kOe, reinforcing the view that the resonance field must reach a certain value (probably greater than 1 kOe) before surface ferromagnetic resonance is induced according to Equation 74. We do not plot any data for the surface ferromagnetic peak below certain temperatures in Figure 14 and 15 because the "spiral phase" paramagnetic peak becomes large enough to seriously interfere with an accurate amplitude or resonance field determination.

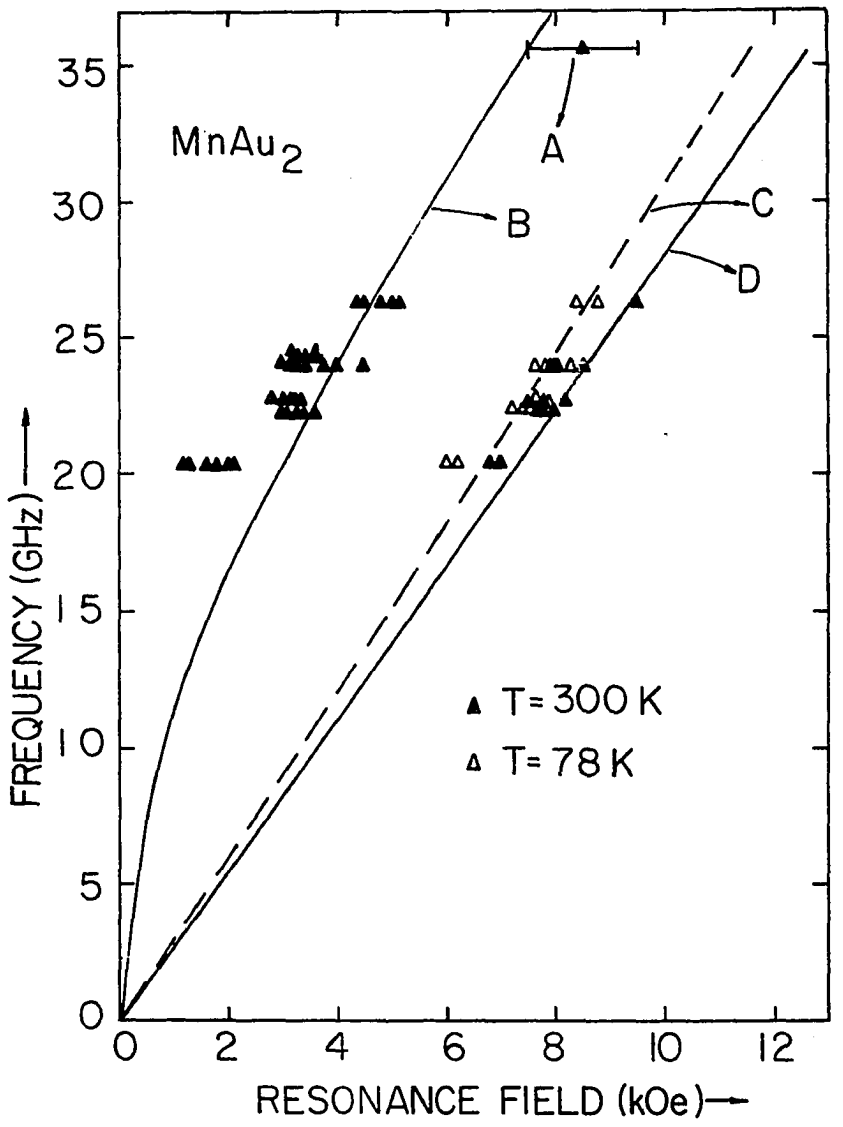

Figure 17. Plot of frequency vs resonance field for microwave absorption peaks called the "surface" ferromagnetic and "spiral phase" paramagnetic peaks in the spiral phase of $MnAu_2$. The letters are as follows: A, Asch's "surface" ferromagnetic resonance peak at T=300 K. The error bar is placed because the peak is very broad, making it difficult to pick the exact maximum. B, plot of Equation 74 for the "surface" ferromagnetic resonance peaks using g=1.9, H_A=23 kOe, σ=0.834 and $I_{5/2}$=0.58 at T=300 K. C, plot of Equation 63 for the spiral phase paramagnetic peaks at T=78 K, giving g≅2.18. D, plot of Equation 63 for the spiral phase paramagnetic peaks at T=300 K, giving g≅2.0.

The "spiral phase" paramagnetic resonance will now be discussed in more detail. Lines C and D in Figure 17 show that the spiral phase paramagnetic resonance is consistent with a linear frequency vs field plot as predicted by Equation 63, which is why we use the name spiral phase "paramagnetic" resonance. The closed circles in Figures 14 and 15 are definitely due to the bulk paramagnetic resonance of the sample above the Néel temperature of T=363 K because of their sudden appearance with large amplitude and approximately expected value of g just above the Néel temperature. It is instructive to compare the behavior of the "spiral phase" paramagnetic peaks to the behavior of the paramagnetic peaks above the Néel temperature in Figures 14 and 15 in order to show similarities in temperature dependence. In Figure 14 a rise in resonance field of the "spiral phase" paramagnetic peaks for temperatures increasing from 5 K is noted, which is similar to the rise in resonance field of the paramagnetic peaks for temperatures increasing from 363 K. In Figure 15 a steady decrease in resonance amplitude of the "spiral phase" paramagnetic peaks for temperatures increasing from 5 K is noted, which is similar to the steady decrease in resonance amplitude of the paramagnetic peaks for temperatures increasing from 363 K. The spiral phase paramagnetic peaks perhaps indicate magnetic ordering of some type below T=5 K if the analogy with the bulk paramagnetic peaks holds below T=5 K. Even the line shape of the spiral phase paramagnetic peak at T=78 K is similar to the line shape of the bulk paramagnetic peak at T=375 K in Figure 13. The large amplitude of the spiral phase paramagnetic peak at T=5 K (comparable to the bulk paramagnetic peak at T=363 K) indicates that perhaps the entire

microwave skin depth of about 10^4 Å in $MnAu_2$ participates in the spiral phase paramagnetic resonance. It may even be that the spiral phase paramagnetic state actually extends throughout the bulk of the $MnAu_2$ sample. Evidence for this comes from a statement in the last paragraph of the neutron diffraction paper on $MnAu_2$ by Herpin and Meriel (37). They predict the susceptibility of polycrystalline $MnAu_2$ in the spiral phase from parameters determined from their neutron diffraction work using the theoretical models of Villain (44) and Yoshimori (53) and compare their results to the experimental susceptibility measurements in the spiral phase of polycrystalline $MnAu_2$ made by Meyer and Taglang (38). They state, "The fact that the initial [theoretical] susceptibility [in the spiral phase] is smaller than the experimentally observed susceptibility can be explained by the existence of a constant paramagnetism that we have not taken account of." If there is a "constant paramagnetism" in the spiral phase of $MnAu_2$, then our "spiral phase" paramagnetic peak could be explained as actually due to a bulk paramagnetic phenomenon in the ordered spiral phase of $MnAu_2$! If a component of the spin is in fact disordered throughout the bulk of the sample, that might explain why neutron diffraction (37) studies show a magnetic moment in the spiral phase of only 3.6 μ_B as T→0 K, whereas the theoretical magnetic moment is about 5 μ_B for g=2 and S=5/2 in $MnAu_2$. We note that the 9.3 GHz, T=300 K data of Asch (41) do not contain the "spiral phase" paramagnetic peak, probably because of its small amplitude at T=300 K and the fact that Asch took his data point

by point without an x-y recorder. In the 35.6 GHz data of Asch (41) the peak called the "spiral phase" paramagnetic peak should be in the fan phase of $MnAu_2$ at about 12 kOe if it exists in this phase. Unfortunately, Asch does not go to low enough temperatures or show enough data at the temperatures he does use for us to be certain whether he sees the "spiral phase" paramagnetic peak in the fan phase or not. We do know that we see no "spiral phase" paramagnetic peak in the field-induced ferromagnetic phase of $MnAu_2$ in the predicted field range from 30-38 kOe ($1.92<g<2.5$) in our 102.4 GHz data using the same sample as for the low frequency studies. Apparently the "spiral phase" paramagnetic state does not exist when $MnAu_2$ is ferromagnetic even though magnetization studies (38) show a magnetic moment at H=30 kOe of only 3.5 μ_B at T=0 K, much less than the previously discussed theoretical maximum of 5 μ_B. Perhaps the ferromagnetic state in $MnAu_2$ is actually a fan structure even at large values of applied field, accounting for the low observed saturation magnetic moment. Neutron diffraction studies on $MnAu_2$ in an applied field could help clarify this point. We certainly would have expected to see any large amplitude "spiral phase" paramagnetic peak at 102.4 GHz and about 30 kOe (corresponding to g=2.5 in Equation 63) at T=5 K if it existed as it does at 22 GHz.

Absorption in the fan phase of polycrystalline $MnAu_2$ will now be discussed. Figure 13 shows two curves in the fan phase at T=300 K. The curve with the rise in power absorbed at H=10 kOe was an initial up-sweep in field. We attribute the peak at H=10 kOe to domain alignment

at the onset of the fan phase in $MnAu_2$ because successive curves (i.e., the other curve extending into the fan phase at T=300 K) do not show this peak. Apparently the domains become "trained" by successive up-sweeps of the magnetic field so that domain alignment does not affect microwave absorption. Both of the T=300 K curves in Figure 13 that extend into the fan region have peaks at about H=17 kOe for $H_{rf} \perp H_{dc}$ (ϕ=90°). These peaks do not have any consistent amplitude vs ϕ (the angle between H_{rf} and H_{dc}) dependence. (Different results are obtained for the amplitude vs ϕ measurements at different temperatures and on different days.) The amplitude vs ϕ dependence of these peaks is not even symmetric about ϕ=90° and ϕ=0° as should be the case by considering the symmetry of the experimental configuration if the experimental configuration is really the cause of the peaks as expected for magnetic resonance absorption. We conclude that these peaks are in some way associated with the static magnetic properties of the fan structure in $MnAu_2$ as it closes towards ferromagnetic alignment. The magnetostriction vs applied field data of Kazama et al. (52) shows an extremum at about 17 kOe and 284 K, which probably explains the observed peaks in our data at about 17 kOe and T=300 K. In any case, the large magnetostriction in the fan region makes it very difficult to observe true resonance absorption at any temperature. The only data which might be interpreted as the $\hbar\omega(\sin k_o)$ mode given by Equation 72 occurred at T=5 K. There is still large magnetostriction in the fan region at this temperature, but the change in magnetostriction vs

temperature is monotonic without any extrema (52). Figure 13 gives an example of the peak observed at T=5 K and $H_{rf} \| H_{dc}$ (the polarization for excitation as predicted for Equation 72) (42). The amplitude vs ϕ dependence is shown in Figure 16. The amplitudes have the correct symmetry about $\phi=90^\circ$, but they do not follow the expected $\cos^2\phi$ amplitude dependence very well. The peak occurs at about $H \cong 17$ kOe, disturbingly close in field to the peaks at T=300 K that are probably due to magnetostriction, but the amplitude of the peak at T=5 K is about two orders of magnitude less intense than the peaks at T=300 K. (Low intensity is predicted at our low experimental frequency for the $\hbar\omega(\sin k_o)$ mode (42).) The departure from the $\cos^2\phi$ dependence can be explained by the fact that this peak has small amplitude. The amplitude had to be measured from the minimum of the dip just preceding the onset of power absorption (see T=5 K data in Figure 13) because the minimum amplitude of the "spiral phase" paramagnetic peak at $\phi=0^\circ$ in Figure 16 was actually larger than the maximum of the possible $\hbar\omega(\sin k_o)$ peak, making it impossible to take the zero of amplitude of the possible $\hbar\omega(\sin k_o)$ peak at H=0. If we have observed the $\hbar\omega(\sin k_o)$ peak at T=5 K, H=17 kOe, ν=22.3 GHz and $\phi=0^\circ$, then Equation 72 predicts H_f=18 kOe, which is close to being correct. It is difficult, however, to know exactly what the experimental value of H_f is at T=5 K because the experimental measurements in an applied field which can yield this information do not extend below T=273 K, where the experimental value for H_f is between 15 and 16 kOe (37, 38). An extrapolation of the work of Meyer

and Taglang (38) indicates, however, that a value of H_f between 17 and 18 kOe at T=5 K would not be unreasonable. There is the possibility that the peak we call the $\hbar\omega(\sin k_o)$ peak is actually due to the fan-ferromagnetic transition and/or magnetostriction. We conclude that we may have observed the $\hbar\omega(\sin k_o)$ mode, but we cannot be sure. Asch (41) never reported trying to observe a resonance with $H_{rf} \| H_{dc}$ at his experimental frequencies, so he could not have observed the $\hbar\omega(\sin k_o)$ mode even if it existed.

F. Discussion

The evidence shall now be listed in favor of assuming that all the microwave absorption phenomena presented in the previous section is due to polycrystalline $MnAu_2$ and not to "impurities" caused by an excess or deficiency of Mn: 1. The stoichiometry of the sample was almost that of ideal $MnAu_2$ as determined by chemical analysis. 2. The electron microprobe showed that the sample was composed of a major matrix of uniform composition close to ideal $MnAu_2$ with some small spot areas, some Mn rich and some Mn poor. 3. The lattice parameters of the sample determined using X-rays were those of ideal $MnAu_2$, and were presumably the parameters of the major matrix. (We would not expect X-ray scattering from the spot areas to be visible on the film used considering the exposure time.) 4. The density of the sample was almost exactly the same as expected for $MnAu_2$.

We have now established quite well that the major matrix of the sample is ordered $MnAu_2$. The question is whether the spot areas that

are Mn rich or poor can contribute to the observed power absorption. The spot areas are presumed to magnetically order at temperatures different from $MnAu_2$ (54), and other properties such as magnetic transition fields would probably also be different for spot areas, allowing an internal check on the properties of the microwave absorption peaks we observe. Some of these internal properties indicating that our observed peaks occur in the major matrix ($MnAu_2$) of our sample are: 1. Often the initial up-sweep in field shows a peak in microwave absorption at $H \cong 10$ kOe, the spiral-fan transition field for $MnAu_2$ (see Figure 13). 2. The values of g and H_A as well as the temperature dependence of the resonance fields determined from our 102.4 GHz ferromagnetic resonance experiments are in good agreement with the magnetization work of Meyer and Taglang (38) for $MnAu_2$ and the theory of Cooper et al. (8, 9, 42) applied to $MnAu_2$. 3. At lower microwave frequencies the paramagnetic phase paramagnetic resonance appears suddenly with large intensity at the Néel temperature (T=363 K) for $MnAu_2$ (see Figures 14 and 15). 4. The "surface" ferromagnetic peak in the spiral phase has a temperature dependence predicted by the theory of ferromagnetic resonance applied to $MnAu_2$ by Cooper et al. (8, 9, 42) using the neutron diffraction work of Herpin and Meriel (37) on $MnAu_2$ for the temperature dependence of σ at H=0 (see line A in Figure 14). 5. Extrema in the magnetostriction for $MnAu_2$ (52) appear to produce corresponding large intensity peaks in the microwave absorption (see Figure 13). 6. The intensity of the "spiral phase" paramagnetic peak

at T=5 K is comparable to the intensity of the paramagnetic phase paramagnetic peak at T=363 K, indicating that the spiral phase paramagnetic peak is due to resonance in the major matrix ($MnAu_2$) of the sample (see Figure 15). 7. If the "spiral phase" paramagnetic peak at 22 GHz were due to paramagnetic absorption by some of the impurity spots (Mn rich or poor) observed in the sample by the electron microprobe, it would also be observable at 102.4 GHz, which it is not. (A paramagnetic resonance in spot areas would not be affected by a field-induced ferromagnetic transition in the major matrix ($MnAu_2$) except perhaps by the small demagnetizing effects of the sample as a whole.) 8. Herpin and Meriel (37) state that a "constant paramagnetism" in the spiral phase of $MnAu_2$ can explain the initial susceptibility of $MnAu_2$ determined by Meyer and Taglang (38). Our "spiral phase" paramagnetic resonance in the spiral phase of the sample may indicate the existence of this proposed "constant paramagnetism" in the spiral phase of $MnAu_2$. 9. The peaks we call "surface" ferromagnetic resonances were also observed by Asch (41). (He did not go to low enough temperatures to observe the spiral phase paramagnetic peaks, and he never reported trying to use the $H_{rf} \| H_{dc}$ configuration necessary to observe the $\hbar\omega(\sin k_o)$ mode.) We thus have two different samples on different continents in which the "surface" ferromagnetic peak is observed, making it less probable that the peak is due to an impurity peculiar to our $MnAu_2$ sample.

We conclude that the "surface" ferromagnetic and the "spiral phase" paramagnetic peaks we have observed at low microwave frequencies

($\cong$22 GHz), as well as the ferromagnetic peaks observed at high microwave frequencies ($\cong$100 GHz), are all due to resonance absorption in polycrystalline $MnAu_2$. We have no certain evidence as to whether or not the possible $\hbar\omega(\sin k_o)$ peak observed at T=5 K (see Figure 13) is a resonance absorption in $MnAu_2$ because it could conceivably be associated with magnetostriction and/or the fan-ferromagnetic transition in $MnAu_2$. It has such weak intensity that it might even be due to a resonance in a spot area of the sample. A resonance that has maximum amplitude when $H_{rf} \| H_{dc}$ is very unusual, however, so the T=5 K resonance in Figure 13 is probably due to the $\hbar\omega(\sin k_o)$ mode in $MnAu_2$ if it is really a resonance absorption.

G. Conclusions

We observe four different resonance absorptions we attribute to polycrystalline $MnAu_2$, and one possible resonance absorption we attribute to polycrystalline $MnAu_2$ if it is actually a resonance absorption. At high microwave frequencies we observe a ferromagnetic resonance in the field-induced ferromagnetic phase of $MnAu_2$. At low microwave frequencies we observe a paramagnetic resonance above the Néel temperature in the paramagnetic phase of $MnAu_2$, and two unusual resonances we call the "surface" ferromagnetic and "spiral phase" paramagnetic resonances in the spiral phase of $MnAu_2$. In the fan phase of $MnAu_2$ at low microwave frequencies and T=5 K with $H_{rf} \| H_{dc}$, we observe a possible $\hbar\omega(\sin k_o)$ resonance.

We obtain g=1.92 using Equation 63 from our paramagnetic resonance data at T=440 K in Figure 14. We get consistent results by assuming this value of g is temperature independent in all our ferromagnetic resonance calculations even though this value was determined for paramagnetic resonance. From the low temperature ferromagnetic resonance data in Figure 12 at 102.4 GHz using Equation 76, we obtain H_A=45 kOe. This value of H_A for the bulk sample is almost the same as the experimental determination of H_A by Meyer and Taglang (38) at low temperatures.

The "surface" ferromagnetic resonance is given this name because the peak behaves like a ferromagnetic resonance in $MnAu_2$ obeying Equation 74 with g=1.9 and H_A=23 kOe, but actually occurs in the spiral phase of $MnAu_2$ where no such resonance is expected (8, 9, 42). The only way to resolve this discrepancy is to consider that an applied field in the spiral phase causes some magnetic moments in the surface layer of the sample to become ferromagnetic because the long range oscillatory exchange interaction producing the spiral phase in the bulk sample cannot act equally in all equivalent crystallographic directions at the surface.

The "spiral phase" paramagnetic resonance may well turn out to be due to a bulk paramagnetic phenomenon in the spiral phase of $MnAu_2$ where a component of the magnetic moment might be disordered (37). The smaller than expected magnetic moment observed as T→0 K in $MnAu_2$ (37) would be explained if a component of the magnetic moment on each spin was paramagnetic with an ordering temperature (if the

paramagnetic component does order) below T=5 K. The "spiral phase" paramagnetic resonance does not occur in our 100 GHz data in the field-induced ferromagnetic phase of $MnAu_2$ as it should if it existed in this phase. We conclude that the "spiral phase" paramagnetic resonance is a property of the spiral phase and not the field-induced ferromagnetic phase of $MnAu_2$.

The possible $\hbar\omega(\sin k_o)$ resonance in the fan phase of $MnAu_2$ is weak in intensity as expected, has about the expected resonance field, and has maximum intensity when $H_{rf} \| H_{dc}$ as predicted. There are, however, the difficulties of large magnetostriction in the fan phase of $MnAu_2$ (52) and the fan-ferromagnetic transition which make it difficult to be certain if a true resonance absorption has been observed. The only possible candidate for the $\hbar\omega(\sin k_o)$ mode was observed at T=5 K (see Figure 13).

In the previous section (III F), reasons are listed for believing that the resonances discussed above are actually due to polycrystalline $MnAu_2$.

IV. ERBIUM

A. Introduction

Erbium crystallizes in a hexagonal close-packed (hcp) structure and is very malleable with a bright, silvery, metallic luster. The metal is fairly stable in air and does not oxidize as rapidly as some of the other rare-earth metals (1). Erbium oxide has a pink color (1). In its metallic state (below 1497° C) Er is a tri-valent ion immersed in a sea of conduction electrons. The electronic configuration for the Er ion is $4f^{11}5s^{2}5p^{6}$ with a ground state spectroscopic designation $^{4}I_{15/2}$ and a Landé factor g=6/5. The maximum theoretical magnetic moment on one Er ion at low temperatures is therefore 9 μ_B where μ_B is the Bohr magneton. This magnetic moment is entirely due to the unfilled 4f electronic shell inside the 5s and 5p shells, and is therefore very localized on the Er ion. The Er metal can be thought of as a lattice of atomic magnets interacting with each other via a sea of conduction electrons. One theory developed for the rare-earth ions interacting with the conduction electrons is called the RKKY theory after Ruderman-Kittel-Kasuya-Yosida (55, 56, 57). Crystalline anistropy arguments were also developed to explain the influence of the atomic lattice on the magnetic ordering of the rare-earths (58, 59). These theories qualitatively predict the various magnetic structures observed in the rare-earth metals (2). In particular, the RKKY theory produces an exchange interaction that is long range and oscillatory,

both necessary conditions for the spiral magnetic structures which exist in the rare-earths.

In zero applied field Er is paramagnetic above T=86 K, has several antiferromagnetic phases between 18 K and 86 K, and conical ferromagnetism below 18 K (60, 61). The major antiferromagnetic phases determined by neutron diffraction (60) are a sinusoidally modulated magnetic moment along the c-axis with a period of seven atomic layers and no ordering of the moments in the basal plane from 86 to 51 K, and a quasi-antiphase-domain structure with almost square-wave modulation of the c-axis magnetic moments and helical ordering of the moments in the basal plane from 51 to 18 K. Below 18 K the magnetic moments lie on a cone of half-angle 28.5° with a turn angle of 43.3° between the projection on the basal plane of the magnetic moment of any two adjacent spins along the c-direction. Because of the large axial anisotropy producing the conical ferromagnetic state, an applied magnetic field of up to 18 kOe along the c-axis below T=18 K produces little change in the cone half-angle (62). The magnetostriction relative to the demagnetized state for an applied field of 30 kOe along the c-axis is comparatively small, again indicating little change in the cone half-angle with applied magnetic field below T=18 K (63).

An applied field in the basal plane (perpendicular to the c-axis) below T=18 K causes a transition in which the ferromagnetic cone configuration changes to a fan configuration about the field direction with the magnetic moments still at an angle with the c-axis given by the

ferromagnetic cone half-angle (63). By increasing the field the fan can be made to close continuously to a pure ferromagnetic state still at an angle with the c-axis given approximately by the ferromagnetic cone half-angle (63). Even higher fields presumably would eventually align the ferromagnetic moments along the applied field.

Our experiment is able to detect some field-induced magnetic transitions, especially antiferromagnetic-ferromagnetic transitions, as a real or apparent change in microwave power absorbed by the sample. An actual increase or decrease in power absorption by the sample occurs if there is a change in the imaginary part of the rf susceptibility of the sample at the transition. An apparent change in microwave absorption by the sample at the transition can be caused by magnetostriction in the sample which slightly changes the cavity-sample configuration, thereby changing the cavity Q. The geometry of our samples and the relative ease of taking microwave measurements allow us to extend transition field measurements to previously neglected crystallographic directions.

We also look for magnetic resonance in the various phases of Er.

B. Theory

The theory for spin wave resonance in all the magnetic phases of Er has been worked out by Cooper et al. (9, 42). We adopt the notation of the theory section III B for the remainder of this section.

In the cone region below T=18 K, the component of the magnetic moment in the basal plane forms a spiral along the c-axis of turn-angle

$k_o c'$. For an applied field along the c-axis the equation for spin wave resonance in Er is given by Equation 32 with the substitution (9, 42)

$$K_2 \rightarrow K_2 - L = K_2 - 6K_4 S^2 \cos^2\psi - 15K_6 S^4 \cos^4\psi \qquad (77)$$

where K_4 and K_6 are the axial anisotropy terms of fourth and sixth orders (not included in Equation 11). ψ is the semivertical angle of the cone generated by the magnetic moments. As discussed in the introduction (IV A), we can take $\psi \cong 30^\circ$ for all ordinary laboratory values of applied field.

If a magnetic field is applied in the basal plane of Er below T=18 K, a transition to a fan structure described in the introduction (IV A) occurs approximately when

$$\frac{E_{cone}}{N} - \frac{E_{ferro}}{N} = -a_o \sin^2\psi + g\mu_B S H_c \sin\psi - \frac{\Delta E_{me}}{N} = 0 \ . \qquad (78)$$

ΔE_{me} symbolically represents the change in magnetoelastic energy between the cone and fan phases, and the Hamiltonian (Equation 11) has been used in the molecular field approximation for the other terms. The fan configuration is approximated in Equation 78 by a ferromagnetic configuration (E_{ferro}) with all the moments at an angle ψ to the c-axis. (Since all crystal field anisotropy terms cancel in Equation 78, the fact that we have neglected K_4 and K_6 in Equation 11 is of no consequence.) The more detailed theory of Nagamiya et al. (39, 40) adapted by Cooper and

Elliott (42) for Er indicates that H_c solved from Equation 78 above should be the correct cone-fan transition field even though Equation 78 is written here only as a first approximation to the cone-fan transition. The fan-ferromagnetic transition (where the spins are all at an angle $\psi \cong 30^\circ$ to the c-axis after the transition) should take place at a field of about $H_f = 2H_c$.

When $H > H_f$ in the basal plane of Er for temperatures below 19 K, ordinary ferromagnetic resonance occurs at frequencies given by (42)

$$\hbar\omega(0) = \{ \frac{g\mu_B H}{\sin\psi} [\frac{g\mu_B H}{\sin\psi} + 2S \sin^2\psi (L - K_2)] \}^{\frac{1}{2}}. \qquad (79)$$

Even if $H_c < H < H_f$ we expect Equation 79 to be a good approximation to the resonance frequency by analogy to ferromagnetic resonance given by Equation 71 in the field-induced fan phase of a planar spiral (42). (Equation 71 is almost the same as the pure ferromagnetic resonance given by Equation 74.) To get Equation 71 a small negative term is added to the terms under the radical in Equation 74. By analogy to the spiral case we therefore assume that Equation 79 gives an upper bound to the resonance frequency which should be quite close to the true resonance frequency when $H_c < H < H_f$ (42).

Numerical estimates of the exchange parameters in Er at temperatures below 18 K can be made using the three-layer model described by Cooper (64) for a hexagonal close-packed rare-earth metal. On the basis of this model the exchange parameters for Er can be obtained as was done

for $MnAu_2$ in section III B. First, a Hamiltonian for Er analogous to Equation 58 is written, which is then minimized with respect to the basal plane spiral turn angle $k_o c' = \theta$ to obtain (12)

$$\cos \theta = \frac{-3J_1}{4J_2} . \tag{80}$$

Next Equation 12 for $\vec{q} = q\hat{\zeta}$ is used to obtain

$$J(q) = 6J_0 + 6J_1 \cos qc' + 2J_2 \cos 2qc' \tag{81}$$

where J_0 is the magnetic interaction between a given magnetic moment and its six nearest neighbors in the same atomic plane perpendicular to the c-axis, J_1 is the magnetic interaction between a given magnetic moment and its six nearest neighbors in the two nearest atomic planes perpendicular to the c-axis, and J_2 is the magnetic interaction between a given magnetic moment and its two nearest neighbors in the two next nearest atomic planes perpendicular to the c-axis.

The definition given by Equation 43 combined with Equation 81 is used to find J_0, J_1, J_2 and a_n for all values of n by solving simultaneously Equations 78, 80, and 60. In Equation 78 the values $g=6/5$, $\psi \cong 30°$, $S=15/2$, $H_c=18$ kOe and $\Delta E_{me}=0$ are used. (Justification for taking $\Delta E_{me}=0$ will be made later.) In Equation 80 we take $\theta=43.3°$. In Equation 60, $T_N=51$ K is taken because that is the temperature magnetic ordering in the basal plane ceases, and make the replacement $S \rightarrow S\sin\psi$

(the component of spin in the basal plane). The result is

$$\begin{aligned} J_0 &= -0.015 \text{ meV} \\ J_1 &= 0.109 \text{ meV} \\ J_2 &= -0.112 \text{ meV} \\ a_o &= 1.88 \text{ meV} \\ a_2 &= 12.8 \text{ meV} . \end{aligned} \tag{82}$$

Justification for taking $\Delta E_{me}=0$ above is made by calculating its contribution to a_0 in Equation 78. For $T<18$ K, ΔE_{me} is just the change in magnetoelastic energy due to the components of the magnetic moment in the basal plane changing from a spiral to a fan configuration under the influence of an applied field in the basal plane. There is no magnetoelastic energy associated with the spiral configuration in the basal plane (3) (called clamping of the magnetoelastic energy), so ΔE_{me} is just the magnetoelastic energy of the fan configuration in the basal plane when $H>H_c$. This energy is negative and is given by Cooper (8) following the treatment of Callen and Callen (19) as

$$\Delta E_{me} = - \frac{1}{8} c^{\gamma}(\lambda^{\gamma})^2 \tag{83}$$

where λ^{γ} is a magnetostriction constant of the γ strain mode (denoting an orthorhombic distortion of the basal plane) and c^{γ} is an elastic stiffness constant related to the five independent cartesian stiffness

constants by (8, 19)

$$c^{\gamma} = 2(c_{11}-c_{12}) \ . \tag{84}$$

Values of c_{11} and c_{12} are obtained from the measurements of Fisher and Dever (65) so that $c^{\gamma}=1.212X10^{12}$ erg/cm^3 at 63 K. We assume this value of c^{γ} is almost temperature independent. The value $\lambda^{\gamma}=7.24X10^{-4}$ is obtained from the magnetostriction measurements of Rhyne and Legvold (63) at T=4.6 K for an applied field of 30 kOe in the basal plane. (This value of applied field means Er is in the fan phase.) Combining these results the value $\Delta E_{me}=-7.95X10^{4}$ erg/cm^3 is obtained. The value $N=3.26X10^{22}$ atoms/cm^3 is used for Er in Equation 78 to find that the ΔE_{me} term increases a_0 by only 0.3%, which is negligible.

Something can now be said about the parameter $(L-K_2)$ in Equation 79 by using the point-charge model of Elliott (59) as is done in Reference (42). We, however, will use our experimental result (to be described in more detail later) that for a frequency of 100 GHz no ferromagnetic resonance is observed with an applied field in the basal plane of Er of up to 50 kOe. We therefore assume that $\nu(0)>100$ GHz for a resonance field of 18 kOe in Equation 79. This gives us

$$L-K_2 > 0.115 \text{ meV} \ . \tag{85}$$

Using Equation 85 a lower limit can now be calculated to the $\hbar\omega(\pm k_o)$ frequencies in Er given by Equation 32 with the substitution of Equation 77. The result is (for $\psi \tilde{=} 30°$)

$$\begin{aligned} \nu(+k_o) &> 162 \text{ GHz} \\ \nu(-k_o) &> 772 \text{ GHz} \end{aligned} \tag{86}$$

where Equation 82 has also been used. Ordinary laboratory fields along the c-axis of Er do not change ψ very much as discussed in Section IV A, so the frequencies $\nu(\pm k_o)$ are almost field independent. It would be easier to observe $\nu(\pm k_o)$ by sweeping frequency than by sweeping field.

Spin waves were first observed in Er at H=0 by Woods et al. (66) using neutron diffraction. A better inelastic neutron diffraction investigation of Er by Nicklow et al. (67) will be discussed here. The data of Nicklow et al. show that split between the $\hbar\omega(+k_o)$ and $\hbar\omega(-k_o)$ modes. The split is surprisingly small (about 50 GHz), and the frequency of the lower frequency $\hbar\omega(+k_o)$ mode is about 484 GHz. Our estimates given by Equation 86 are not very accurate, which casts doubt on the theory used to derive Equation 82. Nicklow et al. have difficulty fitting their data with present theory, but by assuming an anisotropic exchange interaction and wavenumber dependent crystal field anisotropy constants they obtain a rough fit to their data. The exchange parameters they obtain are often as much as an order of magnitude smaller than those given in Equation 82, again casting doubt on the theory used

to derive Equation 82. They obtain a value $L\text{-}K_2 \cong 7$ meV at q=0 which shows the correctness of Equation 85 and indicates that an experimental frequency of about 622 GHz at H=18 kOe in the basal plane of Er is required to see the mode given by Equation 79. Another feature of the data of Nicklow et al. is that the spin wave energy tends to zero as $q\hat{\zeta}$ approaches zero, as predicted by Cooper et al. (9) for the ferromagnetic cone configuration of arbitrary cone angle.

By analogy to the spiral case treated in section III B, we expect to see frequencies in Er of wavenumber nk_o where n=0, 2, 3, . . . , when a field in the basal plane has a value $0<H<H_c$ and T<18 K. As for the spiral case in section III B, however, these modes would have very small microwave absorption intensities and could probably not be observed even if large enough microwave (or infrared) frequencies could be attained. (It seems probable that $\hbar\omega(0)=0$ for $H<H_c$ in the basal plane of Er by analogy to the planar spiral case treated in section III B.)

By analogy to the fan case treated in section III B, a weak $\hbar\omega(\sin k_o)$ mode might be expected in Er similar to Equation 72 for a field in the basal plane just below H_f and T<18 K. The intensity of this mode should be greatest when $H_{rf} \| H_{dc}$ and the frequency is as high as possible. Since $H_f \cong 36$ kOe, we could hope to observe this mode only with our 100 GHz cavity in the superconducting solenoid. We observed nothing, which might mean that the mode is too weak in intensity, or

that $H_{rf} \perp H_{dc}$ in the cavity mode used (our 100 GHz cavity was designed to have $H_{rf} \perp H_{dc}$ predominate over $H_{rf} \| H_{dc}$, and the cavity design was not changed to accommodate $H_{rf} \| H_{dc}$).

In the antiferromagnetic phases of Er for 18 K<T<86 K, spin waves do not in general form a correct picture of the excited magnetic states (9). A solution using the equations of motion method (see section III B for calculations using this method) leads to an infinite set of coupled equations (9). Absorption therefore occurs over the whole frequency range and no resonance is observable. Only when nk_o is a reciprocal lattice vector for some whole number n will spin waves be observed, but in general these spin wave frequencies will be in the infrared (9). It is also true that the exact spin configuration is uncertain for some of the antiferromagnetic states of Er, especially in the presence of an applied field, making it difficult to perform accurate calculations (63).

C. Sample Preparation

A 50 gram buttom of pure Er metal was prepared at the Ames Laboratory, Iowa State University, using ion-exchange separation (26). Table 2 gives an impurity analysis of the metal. Using a procedure developed by Nigh (25) this button was annealed under one atmosphere pressure of argon at 1400°C for 15 hours. The temperature was then increased to 1450°C and the sample was moved to the gradient region of the furnace for $3\frac{1}{2}$ hours. The heat was then removed slowly over a period of four hours. Several large single crystals were present in the button as determined by the

Table 2. Er sample impurities in ppm by weight

H	8	Fe	10	Pr	1.6
N	4	Co	<1	Nd	2.4
O	35	Ni	<1	Sm	<1
C	50	Cu	4	Eu	<1
F	56	Ta	20	Gd	4.5
Mg	<0.4	Y	5.4	Tb	<1
Ca	<1	La	6.5	Dy	8
Cr	<1	Ce	<1	Ho	130
Tm	50	Yb	<1	Lu	<1

Laue X-ray technique, from which were prepared two disk-shaped samples using methods described for Tb in section II. C. One of the samples had the c-axis normal with dimensions 9.032 mm diam and 0.523 mm thickness measured by a micrometer. The other sample had the b-axis normal with dimensions 5.334 mm diam and 0.257 mm thickness, also measured by a micrometer. Both these samples have a diameter to thickness ratio of about 20, or a demagnetizing factor of about N_z=0.48. Values of M for Er can be obtained from the magnetization data of Gray and Spedding (61) or Green et al. (62). For an applied field of 20 kOe at T=4.2 K along the c-axis of the b-axis normal Er crystal, N_zM=1.2 kOe. For an applied field of 20 kOe at T=4.2 K along the a-axis of the c-axis normal Er crystal, N_zM=0.45 kOe. These values of N_zM, when subtracted from the

applied field of 20 kOe give the internal magnetic field in the sample.

D. Apparatus

The apparatus used was the same as described previously for experiments in Er and $MnAu_2$.

See section II D for a description of the 24 GHz spectrometer system. In our Er experiments at 24 GHz a gold-0.03 atomic percent iron vs copper thermocouple was used to measure temperatures below about 40 K, and a copper-constantan thermocouple was used above this temperature. The larger c-axis normal Er sample was mounted in the same manner as the larger Tb sample (see Figure 2), except that masking tape placed on the back of the sample and attached to the cavity replaced the Dow Corning stopcock grease. The b-axis normal Er sample was mounted in the same way as the smaller Tb sample (using a copper washer and GE 7031 varnish for glue) except that Armstrong adhesive A-12 replaced GE 7031 varnish for some of the rotation studies where a stronger bond was needed. Armstrong adhesive A-12 is an epoxy and must be mixed in two parts. We used 1 part A to between 2 and 3 parts B for best results. The samples were mounted with H_{rf} at different angles with respect to the major crystallographic directions in different experiments described in section IV E.

See section III D for a description of the 100 GHz spectrometer system shown in Figure 10. Both Er samples were mounted in the same manner as the $MnAu_2$ sample (see Figure 10), except that Armstrong adhesive A-12 (1 part A to between 2 and 3 parts B) was used instead of GE 7031. Care had to be taken to align the desired crystallographic

direction with the direction of the applied magnetic field.

E. Experimental Results

We shall first describe our experiments at 24 GHz. Figure 18 shows representative examples of the data. The leading edge of the absorption minimum for applied field increasing with time at T=34.5 K in Figure 18 corresponds to one of the closed triangles in Figure 19. The closed triangles in Figure 19 follow the antiferromagnetic-ferromagnetic transition field for Er given in References (61) and (62) as a function of temperature. We therefore interpret the closed triangles in Figure 19 as microwave absorption minima at the antiferromagnetic-ferromagnetic transition field. We have plotted the applied field without demagnetizing field corrections in Figure 19 for all data shown because for our thin disk samples demagnetizing effects are negligible in the magnetic phase of Er preceding the transition. We assume the leading edge of an absorption minimum plotted as a closed triangle in Figure 19 represents the correct transition field by analogy with similar work by Stanford (68) at 100 GHz in Ho single crystals. For the closed circles and crosses in Figure 19 (discussed later) the transitions measured by microwave absorption are not as sharp as for the closed triangles, so we plotted the "center" of the absorption as representing a good estimate of the transition field.

At the onset of the field-induced transition to a ferromagnetic configuration the demagnetizing fields begin to decrease the internal field in the sample and thereby contribute to the width of the transition. The transition widths for a transition to a ferromagnetic configuration are about 1 kOe in our data, which can be explained very well by

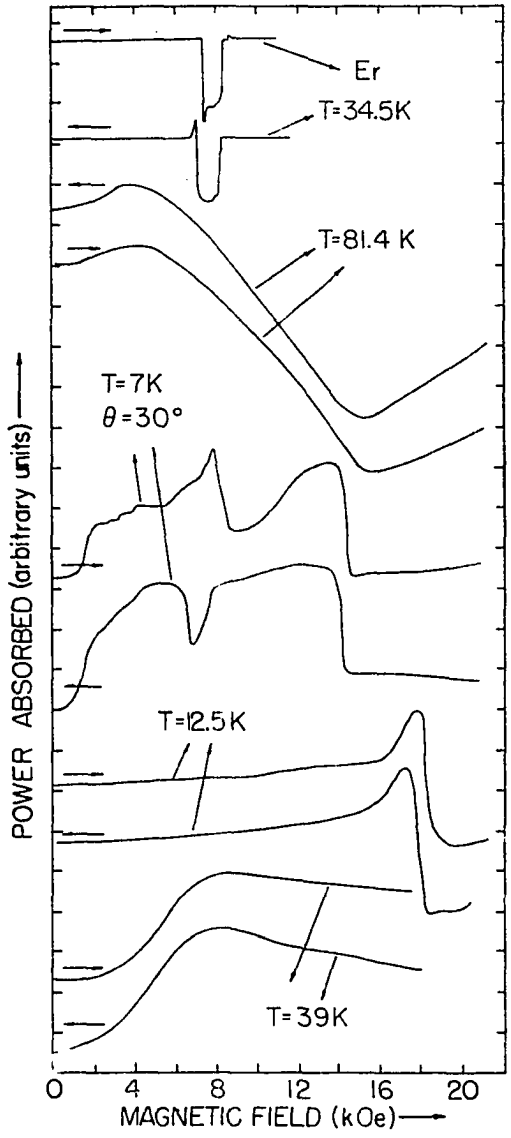

Figure 18. Tracings of typical power absorption vs applied magnetic field curves for Er. The curves at T=34.5 K and T=81.4 K were made using the b-axis normal crystal with $H_{rf} \perp H_{dc} \| c$-axis. The curves at T=7 K were made using the b-axis normal crystal with $H_{rf} \perp c$-axis and H_{dc} at an angle $\theta=30^{\circ}$ to the c-axis in the plane of the sample (see diagram in Figure 20 for the experimental configuration). The curves at T=12.5 K and T=39 K were made using the c-axis normal crystal with $H_{rf} \perp H_{dc} \| a$-axis.

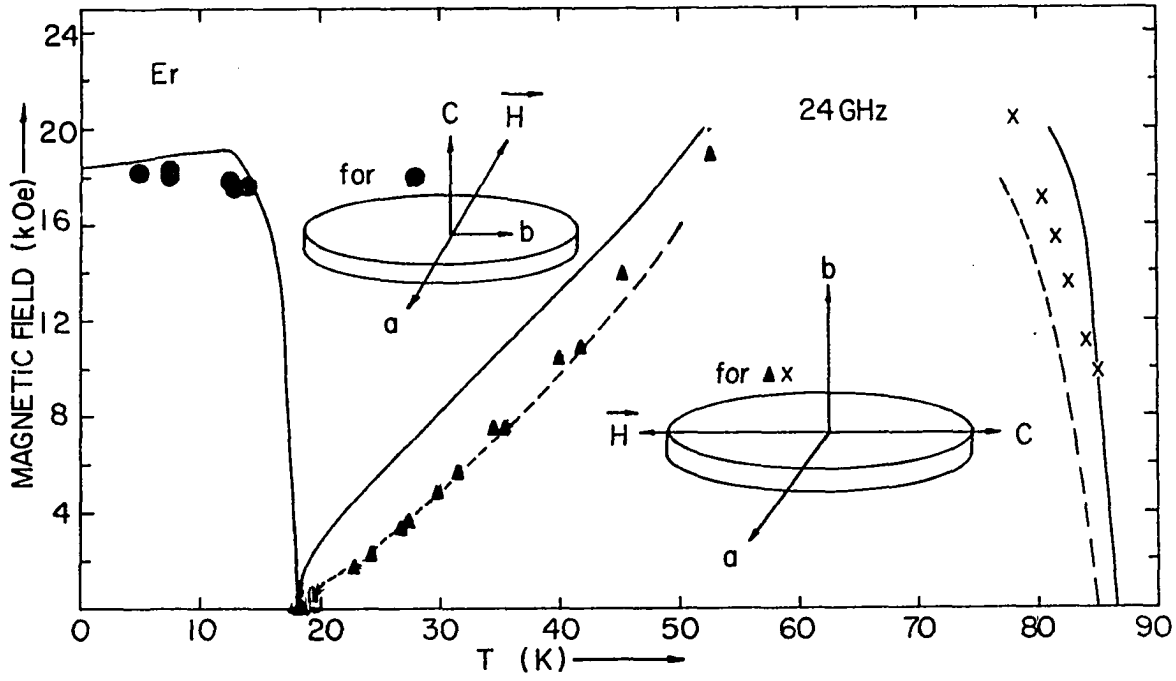

Figure 19. Plot of transition field as a function of temperature for microwave absorption peaks associated with magnetic transitions in Er at 24 GHz. The experimental configurations are shown in the figure. The solid lines are magnetic transition fields vs temperature taken from the magnetization data in Reference (61). The dashed lines are for similar data taken from Reference (62) where less pure Er samples were used. All data plotted are for the applied field increasing with time.

demagnetizing effects (see section IV C).

It is somewhat surprising that the closed triangles in Figure 19 follow the dashed line for less pure Er because our sample was supposedly of the same purity as the samples used to obtain the solid line in Figure 19. Perhaps impurities were introduced in our sample during the crystal growing process. It is also not certain that the closed triangles in Figure 19 taken from microwave absorption data are measuring exactly the same thing as the magnetic transitions taken from magnetization data.

Bagguley and Liesegang (16) also report seeing a microwave absorption (at 35.4 GHz) in Er for $H_{dc} \| c$-axis which has the field vs temperature dependence of the closed triangles in Figure 19. The curves at T=34.5 K in Figure 18 were taken for the configuration $H_{rf} \perp H_{dc} \| c$-axis. The configuration $H_{rf} \| H_{dc} \| c$-axis also produces an absorption minimum that looks almost exactly like the T=34.5 K curves in Figure 18 at the same temperature. The absorption minima corresponding to the closed triangles in Figure 19 were very intense and were taken at low microwave power (about 1-2 milliwatts incident microwave power) to avoid a thermal gradient between the sample and the microwave cavity where the thermocouples were attached. In several of our experiments powdered solder mixed with epoxy was used to glue the sample to the copper plate. Heat was used to harden the epoxy and melt the solder at the same time. A good bond and a good electrical connection between the sample and the copper plate were achieved. A good thermal connection between the sample and thermocouple is therefore probable when the copper plate and sample were mounted on the cavity. An increase in incident microwave power from 1 - 100 milliwatts

caused the thermocouple to read an increase in temperature of only 2 K, so sample heating due to microwave absorption is probably not very significant at low microwave powers.

The curves at T=81.4 K in Figure 18 show a small absorption peak at about 4 kOe followed by a broad desorption with minimum at 15.5 kOe. The peak at about 4 kOe in Figure 18 has a fairly good $\sin^2\phi$ dependence where ϕ is the angle between H_{rf} and H_{dc}. This peak has weak intensity and occurs at all temperatures from above room temperature to T=4.2 K. In an attempt to discover the origin of this peak we took paramagnetic resonance curves of our glue, GE 7031 varnish. GE 7031 varnish was found to have a broad EPR signal that corresponds almost exactly in intensity, field position, and $\sin^2\phi$ dependence to the peak at 4 kOe and T=81.4 K in Figure 18. We conclude that all the weak peaks at about 4 kOe observed in our Er experiments over the whole temperature range are actually due to GE 7031 varnish. The peak shown at 4 kOe and T=81.4 K in Figure 18 was taken at a frequency of 22.6 GHz and so has g=4.0 using Equation 63 for paramagnetic resonance. Our studies of GE 7031 varnish show that there is relatively large data scatter for the field position of the peak. If we take $3.2<g<4.0$ for GE 7031 varnish we are certainly within the allowed values. The EPR signal in GE 7031 probably also explains the broad paramagnetic peak of weak intensity and $g\tilde{=}3.7$ observed by Stanford and Young (50) over a large temperature range while performing experiments on Tb at 100 GHz using GE 7031 varnish for glue. They could not explain this peak at the time, and in later results it was not present (14). Even a small flake of GE 7031 varnish can make an observable EPR signal, so

care must be used when using GE 7031 varnish in microwave experiments. We found the GE 7031 EPR signal valuable, however, for determining whether our cavity was overcoupled or undercoupled in all our Er experiments with the b-axis normal crystal. We could therefore easily distinguish between an absorption and a desorption of microwave power by the b-axis normal sample in our experiments. We were even able to use GE 7031 to determine the coupling of our cavity when the larger c-axis normal crystal was mounted without using glue, because in some of our later experiments the cavity itself was slightly contaminated with GE 7031, giving us a weak GE 7031 EPR signal for determining cavity coupling. For this reason we believe that all the curves in Figure 18 show power absorption correctly.

The absorption minimum at 15.5 kOe and T=81.4 K going up in field in Figure 18 corresponds to one of the crosses in Figure 19. As can be seen from Figure 19, these crosses follow closely the antiferromagnetic-paramagnetic transition field for Er given in References (61) and (62) as a function of temperature. We therefore interpret the crosses in Figure 19 as microwave absorption minima at the antiferromagnetic-paramagnetic transition field. The configuration used for the crosses in Figure 19 is $H_{rf} \perp H_{dc} \| c\text{-axis}$. In contrast to the data represented by the closed triangles, however, when $H_{rf} \| H_{dc} \| c\text{-axis}$ the antiferromagnetic-paramagnetic transition causes an absorption of microwave power rather than a desorption. The GE 7031 EPR signal vanishes when $H_{rf} \| H_{dc}$, but the cavity coupling was checked by rotating H_{dc} so that it was along the a-axis with $H_{rf} \perp H_{dc}$, and then taking data showing the GE 7031 EPR signal coupled

correctly. The extreme width of the absorption minima or maxima associated with the antiferromagnetic-paramagnetic transition is not understood, but may be related to field-induced changes in the antiferromagnetic spin configuration. (Remember that a component of the spin is disordered even at H=0 for T=51-86 K.)

Bagguley and Liesegang (16) report a weak absorption at 17 kOe and 78 K using a frequency of 35.3 GHz. They suggest that their peak has the general shape associated with a microwave resonance absorption, but they were plotting the derivative of power absorption which would tend to look much like resonance absorption if their direct absorption peaks resembled our inverted T=81.4 K curves in Figure 18. We suggest, therefore, that their peak is due to the antiferromagnetic-paramagnetic transition as were our absorption minima shown by the crosses in Figure 19.

The data plotted in Figure 20 show rotation studies in the b-axis normal crystal. The data at T=23 K and T=42 K in Figure 20 at $\theta=0^{o}$ correspond to the closed triangles plotted in Figure 19 which represent the antiferromagnetic-ferromagnetic transition field. The data in Figure 20 at T=23 K and T=42 K show how the antiferromagnetic-ferromagnetic transition field changes as H_{dc} is rotated in the plane of the b-axis normal crystal, data which is not at present available from magnetostriction or magnetization studies (61, 62, 63).

The peaks in absorption in Figure 18 at about 18 kOe and T=12.5 K in the c-axis normal crystal will now be discussed. The peak for field increasing with time is plotted in Figure 19 as a closed circle. The closed circles in Figure 19 follow the cone ferromagnetism-fan ferromagnetism

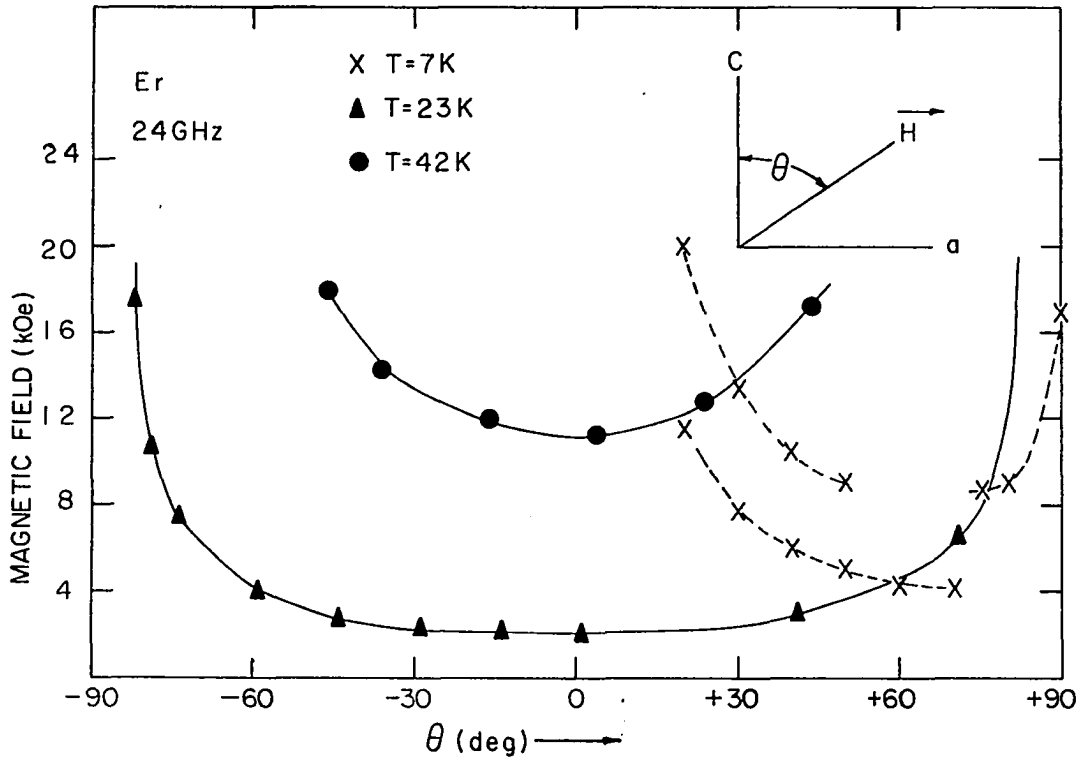

Figure 20. Plot of transition field as a function of θ (defined in the figure) for microwave absorption peaks associated with magnetic transitions in the b-axis normal Er crystal at 24 GHz. All data plotted are for the applied field increasing with time.

transition field for Er given in Reference (61) as a function of temperature. We therefore interpret the closed circles in Figure 19 as microwave absorption at the cone ferromagnetism-fan ferromagnetism transition field. These peaks remain unchanged in line shape and field position as the angle between H_{rf} and H_{dc} is changed in the plane of the c-axis normal crystal, indicating that all crystallographic directions in the basal plane of Er (including the a and b axes) are essentially equivalent. This is in agreement with magnetostriction and magnetization results (61, 63).

We now discuss the absorption peaks in Figure 18 at T=7 K in the b-axis normal crystal. The two largest peaks going up in field are plotted in Figure 20 at $\theta=30^{o}$. It is thought that these peaks represent magnetic transitions from the cone ferromagnetism of Er at T=7 K to other less symmetrical spin configurations, data which is not at present available from other measurements. (The line shapes and unusual hysteresis shown at T=7 K in Figure 18 are not typical of resonance absorption.) In Figure 20 at T=7 K the peak for $\theta=90^{o}$ is at almost 18 kOe as it should be to correspond with the equivalent peak for $H_{dc}\|$a-axis in the c-axis normal crystal shown at T=12.5 K in Figure 18. The equivalent peaks in both Er samples for H_{dc} along the a-axis and T<18 K have about the same line shape and transition field as shown at T=12.5 K in Figure 18 for the c-axis normal sample. The transitions shown in the T=7 K data in Figure 20 (and the T=7 K data in Figure 18) are very unusual for the cone ferromagnetic phase of Er because they occur at fields as low as 4 kOe at $\theta=70^{o}$. Apparently the cone ferromagnetic configuration undergoes magnetic

transitions rather easily in an applied field at certain values of θ between 0^{o} and 90^{o}, whereas no transition at all is expected at $\theta=0^{o}$, and a field of about 18 kOe is required for a transition at $\theta=90^{o}$. The small step-like absorptions seen most clearly at low field while the field is increasing with time at T=7 in Figure 18 are probably due to domain alignment effects.

The broad absorption peaks in Figure 18 at T=39 K in the c-axis-normal crystal will now be discussed. These peaks have very little amplitude change as the angle between H_{rf} and H_{dc} is changed. We note that these peaks are very broad with a maximum in power absorption at about 8 kOe, corresponding closely to broad magnetostriction with an extremum at about 8 kOe observed by Rhyne and Legvold (63) for $H_{dc}\|$a-axis and T=39 K in Er. We therefore conclude that the peaks at T=39 K in Figure 18 are due to magnetostriction effects. Further evidence that this is true comes from the fact that the magnetostriction shows a broad extremum from T=18 K to T=51 K (the quasi-antiphase-domain region of Er) (63), corresponding exactly to the temperature interval in which curves like the T=39 K curve in Figure 18 are observed. Above 51 K there is no longer an extremum in the magnetostriction (63), and there is no longer any change in power absorption with applied field for a field in the plane of the c-axis normal crystal.

We shall now describe our experiments at 100 GHz. Measurements were taken on the b-axis normal crystal in the configuration $H_{dc}\|$c-axis. No microwave absorption was observed in applied fields up to 50 kOe for $4.2\ K<T<18\ K$. For temperatures above 18 K only the antiferromagnetic-

ferromagnetic transition was observed with the same transition field vs temperature dependence as shown by the closed triangles in Figure 18 for 24 GHz.

Measurements were taken at 100 GHz on the c-axis normal crystal in the configuration $H_{dc} \| a$-axis with applied fields up to 50 kOe and $4.2\ K < T < 18\ K$. Only the cone ferromagnetism-fan ferromagnetism magnetic transition was observed with the same transition field vs temperature dependence shown by the closed circles in Figure 18 for 24 GHz. For temperatures above 18 K, only broad absorptions associated with magnetostriction were observed, just as at 24 GHz.

We conclude that no spin wave resonance absorption in Er at 24 GHz or 100 GHz was observed.

F. Discussion

In the previous section (IV E) we compared certain of our experimental results for microwave absorption at field-induced magnetic transitions in Er to similar results obtained by Bagguley and Liesegang (16). In every case where a comparison was made we reported observing a desorption of microwave power by the sample at the transition field, while Bagguley and Liesegang (16) reported observing an absorption of microwave power at the transition field. Because of differences in our experimental configuration as compared with the experimental configuration of Bagguley and Liesegang, it is impossible to know if magnetostriction, for example, would affect the Q of both cavities in the same manner. It is also difficult to know if the data of Bagguley and Liesegang should be inverted or not because they had no internal check on their cavity coupling as we did.

We conclude that it is not surprising that Bagguley and Liesegang (16) see microwave absorption where we see microwave desorption at certain of the field-induced magnetic transitions in Er.

G. Conclusions

We observed no spin wave resonance absorption in Er at 24 or 100 GHz. Using the null result of our 100 GHz experiments, an experimental lower limit was placed on some crystal field parameters for Er. Several experimental configurations were tried with an applied field along all the major crystallographic directions. Only certain field-induced magnetic transitions were observed which had already been observed using other experimental methods. We were able, however, to extend the knowledge of field-induced magnetic transitions in Er to crystallographic directions other than the major ones.

Both the antiferromagnetic-ferromagnetic transition ($T>18$ K) and the antiferromagnetic-paramagnetic transition ($T\cong 80$ K) were observed for an applied field along the c-axis. The antiferromagnetic-ferromagnetic transition was also observed for an applied field at various angles in the plane formed by the c-axis and a-axis. The cone ferromagnetism-fan ferromagnetism magnetic transition ($T<18$ K) was observed for an applied field at any direction in the basal plane of Er, confirming the fact that the basal plane of Er is almost isotropic. Some peaks associated with magnetostriction were observed for a field in the basal plane ($18\text{ K}<T<51\text{ K}$).

The most unusual peaks observed ($T<18$ K) were interpreted to be

magnetic transitions from cone ferromagnetism to other less symmetrical spin configurations for an applied field at various angles in the plane formed by the c-axis and a-axis, data which is at present not available from other measurements. An applied field as small as 4 kOe, for example, is able to cause an apparent transition from cone ferromagnetism to another spin configuration (undetermined) when the applied field is at an angle of 70^{o} to the c-axis in the plane formed by the c-axis and a-axis.

V. LITERATURE CITED

1. Handbook of Chemistry and Physics, College Edition, edited by R. C. Weast (The Chemical Rubber Co., Cleveland, Ohio, c1966), 47th edition.

2. R. M. Bozorth and C. D. Graham, Jr., General Electric Report No. 66-C-225 (1966).

3. W. E. Evenson and S. H. Liu, Phys. Rev. 178, 783 (1969).

4. W. C. Koehler, H. R. Child, E. O. Wollan, and J. W. Cable, J. Appl. Phys. 34, 1335 (1963).

5. D. E. Hegland, S. Legvold, and F. H. Spedding, Phys. Rev. 131, 158 (1963).

6. J. J. Rhyne and A. E. Clark, J. Appl. Phys. 38, 1379 (1967).

7. M. Nielsen, H. Bjerrum Møller, P. A. Lindgård, and A. R. Mackintosh, Phys. Rev. Letters 25, 1451 (1970).

8. B. R. Cooper, Phys. Rev. 169, 281 (1968).

9. B. R. Cooper, R. J. Elliott, S. J. Nettel, and H. Suhl, Phys. Rev. 127, 57 (1962).

10. D. T. Vigren and S. H. Liu, Contribution No. 2890 of the Ames Laboratory of the U.S.A.E.C. (to be published).

11. F. C. Rossol and R. V. Jones, J. Appl. Phys. 37, 1227 (1966).

12. F. C. Rossol, Ph.D. thesis, Harvard University, 1966 (unpublished).

13. E. A. Turov and V. G. Shavrov, Fiz. Tverd. Tela 7, 217 (1965) [English transl.: Soviet Phys. - Solid State 7, 166 (1965)].

14. T. K. Wagner and J. L. Stanford, Phys. Rev. 184, 505 (1969).

15. T. K. Wagner and J. L. Stanford, to be published.

16. D. M. S. Bagguley and J. Liesegang, Proc. Roy. Soc. A300, 497 (1967).

17. T. K. Wagner and J. L. Stanford, Phys. Rev. B1, 4488 (1970).

18. J. J. Rhyne and S. Legvold, Phys. Rev. 138, A507 (1965).

19. E. Callen and H. Callen, Phys. Rev. 139, A455 (1965).

20. D. T. Vigren and S. H. Liu, to be published.

21. D. T. Vigren and S. H. Liu, Contribution No. 2999 of the Ames Laboratory of the U.S.A.E.C. (to be published).

22. C. Kittel, Phys. Rev. 71, 270 (1947); 73, 155 (1948).

23. T. Holstein and H. Primakoff, Phys. Rev. 58, 1098 (1940).

24. R. M. Bozorth, Ferromagnetism (Van Nostrand Co., Inc., New York, 1951).

25. H. E. Nigh, J. Appl. Phys. 34, 3323 (1963).

26. F. H. Spedding, Scientific American 185, 26 (November 1951).

27. J. R. Cleveland, Ph.D. thesis, Iowa State University, 1970 (unpublished).

28. W. J. McG. Tegart, The Electrolytic and Chemical Polishing of Metals, (Permagon Press, New York, c1959), 2nd edition.

29. G. Feher, The Bell System Technical Journal, p. 449 (March 1957).

30. T. Moreno, Microwave Transmission Design Data (Dover Publications, Inc., New York, 1948).

31. R. F. Harrington, Time-Harmonic Electromagnetic Fields (McGraw-Hill Book Co., New York, 1961).

32. R. V. Colvin, S. Legvold, and F. H. Spedding, Phys. Rev. 120, 741 (1960).

33. H. Bjerrum Møller, J. C. Gylden Houmann, and A. R. Mackintosh, Phys. Rev. Letters 19, 312 (1967).

34. M. Nielsen, H. Bjerrum Møller, and A. R. Mackintosh, J. Appl. Phys. 41, 1174 (1970).

35. E. Raub, U. Zwicker, and H. Baur, Z. Metallkunde 44, 312 (1953).

36. J. H. Smith and R. Street, Proc. Phys. Soc. (London) 70B, 1089 (1957).

37. A. Herpin and P. Meriel, J. Phys. Radium 22, 337 (1961).

38. J. P. Meyer and P. Taglang, J. Phys. Radium 17, 457 (1956).

39. T. Nagamiya, J. Appl. Phys. 33, 1029 (1962).

40. T. Nagamiya, K. Nagata, and Y. Kitano, Progr. Theoret. Phys. (Kyoto) 27, 1253 (1962).

41. G. Asch, J. Phys. Radium 20, 349 (1959).

42. B. R. Cooper and R. J. Elliott, Phys. Rev. 131, 1043 (1963).

43. B. R. Cooper and R. J. Elliott, Phys. Rev. 153, 654 (1967).

44. J. Villain, J. Phys. Chem. Solids 11, 304 (1959).

45. R. C. Wayne and F. A. Smith, J. Phys. Chem. Solids 30, 183 (1969).

46. R. J. Elliott and R. V. Lange, Phys. Rev. 152, 235 (1966).

47. B. D. Cullity, Elements of X-Ray Diffraction (Addison-Wesley Publishing Co., Inc., Reading, Mass., 1956).

48. Calibration of the gold-0.03 atomic percent iron vs copper thermocouple was made by M. S. Anderson, H. T. King, and C. A. Swenson at the Ames Laboratory.

49. G. D. Boyd and J. P. Gordan, Bell System Tech. J. 40, 489 (1961); G. D. Boyd and H. Kogelnik, ibid. 41, 1347 (1962).

50. J. L. Stanford and R. C. Young, Phys. Rev. 157, 245 (1967).

51. L. W. Hart and J. L. Stanford, J. Appl. Phys. 41, 2523 (1970).

52. N. Kazama, T. Hirone, K. Kamigaki, and T. Kaneko, J. Phys. Soc. Japan 24, 980 (1968).

53. A. Yoshimori, J. Phys. Soc. Japan 14, 807 (1959).

54. G. Felcher, R. Moon, W. Koehler, and A. Aldred, unpublished manuscript based on work performed under the auspices of the U.S. Atomic Energy Commission, ca. 1969.

55. M. A. Ruderman and C. Kittel, Phys. Rev. 96, 99 (1954).

56. T. Kasuya, Progr. Theoret. Phys. 16, 45 (1956).

57. K. Yosida, Phys. Rev. 106, 893 (1957).

58. H. Miwa and K. Yosida, Progr. Theoret. Phys. 26, 693 (1961).

59. R. J. Elliott, Phys. Rev. 124, 346 (1961).

60. J. W. Cable, E. O. Wollan, W. C. Koehler, and M. K. Wilkinson, J. Appl. Phys. 32, 49S (1961).

61. W. J. Gray and F. H. Spedding, U.S. Atomic Energy Commission Research and Development Report IS-2044, 1968.

62. R. W. Green, S. Legvold, and F. H. Spedding, Phys. Rev. 122, 827 (1961).

63. J. J. Rhyne and S. Legvold, Phys. Rev. 140, A2143 (1965).

64. B. R. Cooper, Proc. Phys. Soc. (London) 80, 1225 (1962).

65. E. S. Fisher and D. Dever, Trans. Met. Soc. AIME 239, 48 (1967).

66. A. D. B. Woods, T. M. Holden, and B. M. Powell, Phys. Rev. Letters 19, 908 (1967).

67. R. M. Nicklow, N. Wakabayashi, M. K. Wilkinson, and R. E. Reed, to be published.

68. J. L. Stanford, Phys. Rev. 165, 642 (1968).

VI. ACKNOWLEDGMENTS

To Professor John L. Stanford, I express my sincere appreciation for guidance and many discussions throughout my graduate student days at Iowa State University. Dr. Stanford suggested the $MnAu_2$ and erbium topics in this thesis. I also thank Professor Timothy K. Wagner for helpful discussions and for teaching me many valuable experimental techniques.

Dennis T. Vigren and Professor Samuel H. Liu developed the theory which suggested the terbium topic in this thesis. To them I am grateful for many discussions covering the whole range of our experiments. Dr. Liu suggested the simple planar spiral model with a turn angle of 120^{o} calculated in section III B.

For designing and developing various parts of the equipment used in these experiments I am grateful to Drs. J. L. Stanford, T. K. Wagner, R. C. Young, J. R. Cleveland, and D. R. Stone. The technical assistance of Harlan Baker, O. M. Sevde, John Hartman, Dave Newquist, Kerry Nelson, M. J. Murtha, J. A. Herriott, Paul Millis, F. A. Schmidt, Francis Laabs, Dr. Donald Bailey, Robert Bachman, Gary Wells, Harry Amenson, R. H. Brown, E. R. Clark, and others at the Ames Laboratory made this work possible.

We are also grateful to Professor F. H. Spedding for the loan of the high-purity terbium and erbium metal, and to Professor R. G. Barnes for the loan of the 24 GHz components used in this investigation.

The financial assistance of an N.D.E.A. Title IV Traineeship during

the first three years of my stay at Iowa State University is certainly appreciated.

To Carol Kline and Laurie Anderson I extend grateful appreciation for typing the final manuscript.

And finally, to my wife Jean, I express the appreciation she deserves for encouraging me through the difficult periods of producing this thesis.